Pontifícia Universidade Católica
do Rio de Janeiro

Antonio Federico Zegarra Borrero

Effects of Interaction and Percolation on Topological Edge States

Tese de Doutorado

Thesis presented to the Programa de Pós-graduação em Física of PUC-Rio in partial fulfillment of the requirements for the degree of Doutor em Ciências - Física.

Advisor: Prof. Wei Chen

Rio de Janeiro
April 2021

Pontifícia Universidade Católica
do Rio de Janeiro

Antonio Federico Zegarra Borrero

Effects of Interaction and Percolation on Topological Edge States

Thesis presented to the Programa de Pós-graduação em Física of PUC-Rio in partial fulfillment of the requirements for the degree of Doutor em Ciências - Física. Approved by the Examination Committee:

Prof. Wei Chen
Advisor
Departamento de Física – PUC-Rio

Prof. José Carlos Egues de Menezes
USP

Prof. Thereza Cristina de Lacerda Paiva
UFRJ

Prof. Roberto Bechara Muniz
UFF

Prof. Tatiana Gabriela Rappoport
UFRJ

Rio de Janeiro, April 9th, 2021

Antonio Federico Zegarra Borrero

The author graduated in Physics from the Universidad Nacional de Ingeniería, Lima –Perú. He obtained the degree of BSc in 2012 and of MSc in 2016.

Bibliographic data

Zegarra Borrero, Antonio Federico

Effects of Interaction and Percolation on Topological Edge States / Antonio Federico Zegarra Borrero; advisor: Wei Chen. – 2021.

100 f: il. color. ; 30 cm

Tese (doutorado) - Pontifícia Universidade Católica do Rio de Janeiro, Departamento de Física, 2021.

Inclui bibliografia

1. Física – Teses. 2. Isoladores topológicos. 3. Estados de borda topológicos. 4. Transições de fase topológicas. 5. Modelo SSH. 6. Modelo BHZ. 7. Torque de spin. I. Chen, Wei. II. Pontifícia Universidade Católica do Rio de Janeiro. Departamento de Física. III. Título.

CDD: 620.11

To my parents Federico Zegarra and Maria Luz Borrero

Acknowledgments

I am totally indebted to my advisor Prof Wei Chen for his infinite patience, support, encouragement, knowledge shared, motivation and very instructive discussions during the PhD Program. I am also very thankful for his guidance and support in the development and reading of this document, for the papers we have published together and for providing me with the opportunity to carry out this research in his working group of condensed matter theory at PUC-Rio. I would also like to thank the support of Prof Carlos Egues from IFSC-USP for being part of our collaboration and for his invaluable guidance and knowledge.

Since studying abroad has presented some administrative and academic challenges, I have been very fortunate to count on the help of great people. I am grateful to the administrative staff of the Departamento de Física at PUC-Rio, specially to Professors Hiroshi Nunokawa and Carla Gobel and the secretary Giza. I thank my postgraduate colleagues for the useful discussions and their honest comments during my stay at PUC Rio and also the Professors I had in different courses. Since they come from a wide range of academic backgrounds and nationalities, they have enriched my experience of studying abroad. Furthermore, I gratefully appreciate the financial support given by CAPES, CNPq and FAPESP during this program.

This study was financed in part by the Coordenação de Aperfeiçoamento de Pessoal de Nível Superior - Brasil (CAPES) - Finance Code 001.

Abstract

Zegarra Borrero, Antonio Federico; Chen, Wei (Advisor). **Effects of Interaction and Percolation on Topological Edge States**. Rio de Janeiro, 2021. 100p. Tese de Doutorado – Departamento de Física, Pontifícia Universidade Católica do Rio de Janeiro.

In this thesis we studied two important Topological Insulators (TIs), where we focused particularly on the role of interactions and percolation on the topological edge states. First, we analyzed the role of nearest-neighbor interactions in a prototype one-dimensional TI, namely the Su-Schrieffer-Heeger (SSH) model. Based on a Green's function formalism, we applied Dyson's equation in combination with T-matrix approximation to verify the bulk-edge correspondence in the presence of interactions. The critical exponents near topological phase transitions are found to be the same as the noninteracting SSH model, indicating that the system stays in the same universality class despite the presence of interactions. The second system is a two-dimensional time-reversal symmetric TI, namely the Bernevig-Hughes-Zhang (BHZ) model in conjunction with a time-reversal breaking ferromagnetic metal (FMM), where we investigated the percolation of the quantum spin Hall state from the TI layer to the FMM by means of a tight-binding model. We demonstrated that depending on whether the edge state Dirac cone submerges into the FMM subbands and the direction of the magnetization of the FMM, the percolation of the edge state and its spin-momentum locking are affected in different ways. Surprisingly, we uncover that the equilibrium edge spin current in the BHZ model, naturally expected from the spin polarized propagating edge states, is in fact absent due to the cancellation from the valence bands. Nevertheless, laminar flows of room temperature persistent charge and spin currents are produced near the interface of the BHZ/FMM junction. Using a linear response theory, we investigate the current-induced spin polarization caused by the percolation of the edge state, which serves as a spin torque that is found to be predominantly field-like. Moreover, the spin polarization is dramatically enhanced near the impurities at the edge of the BHZ model.

Keywords

Topological insulators; Topological edge states; Topological phase transitions; SSH model; BHZ model; Spin torque.

Resumo

Zegarra Borrero, Antonio Federico; Chen, Wei. **Efeitos de Interação e Percolação nos Estados Topológicos de borda**. Rio de Janeiro, 2021. 100p. Tese de Doutorado – Departamento de Física, Pontifícia Universidade Católica do Rio de Janeiro.

Nesta tese estudamos dois importantes sistemas de Isoladores Topológicos (TIs), onde nos concentramos particularmente no papel das interações e percolação nos estados de borda topológicos. Primeiro, analisamos o papel das interações vizinhas mais próximas em um protótipo de TI unidimensional, o modelo Su-Schrieffer-Heeger (SSH). Com base em um formalismo de função de Green, aplicamos a equação de Dyson em combinação com a aproximação da matriz-T para verificar a correspondência bulk-edge na presença de interações. Os expoentes críticos próximos às transições de fase topológicas são os mesmos do modelo SSH não interagente, indicando que o sistema permanece na mesma classe de universalidade, apesar da presença de interações. O segundo sistema é um TI bidimensional simétrico na inversão de tempo, ou seja, o modelo de Bernevig-Hughes-Zhang (BHZ) em conjunto com um metal ferromagnético com quebra de reversão do tempo (FMM), onde investigamos a percolação do estado Hall de spin quântico do modelo BHZ para o FMM por meio de um modelo de ligações fortes (tight-binding). Demonstramos que dependendo de se o estado de borda do cone de Dirac submerge nas sub-bandas do FMM e da direção da magnetização do FMM, a percolação do estado de borda e seu spin-momentum-locking são afetados de maneiras diferentes. Surpreendentemente, descobrimos que a corrente de spin de borda de equilíbrio no modelo BHZ, naturalmente esperada dos estados de borda de propagação do spin polarizado, está de fato ausente devido ao cancelamento das bandas de valência. No entanto, fluxos laminares de correntes de carga e spin persistente à temperatura ambiente são produzidos perto da interface da junção BHZ / FMM. Usando teoria de resposta linear, investigamos a polarização de spin induzida pela corrente causada pela percolação do estado de borda, que serve como um torque de rotação que é encontrado ser predominantemente field-like. Além disso, a polarização do spin é dramaticamente aumentada perto das impurezas na borda do modelo BHZ.

Palavras-chave

Isoladores topológicos; Estados de borda topológicos; Transições de fase topológicas; Modelo SSH; Modelo BHZ; Torque de spin.

Table of contents

List of figures

List of tables

List of Abreviations

CMP – Condensed Matter Physics

QHE – Quantum Hall Effect

QSHE – Quantum Spin Hall Effect

TIs – Topological Insulators

TSCs – Topological Superconductors

TRS – Time Reversal Symmetry

TPT – Topological Phase Transition

1BZ – First Brilloin Zone

SSH – Su-Schrieffer-Heeger (Model of a 1D TI)

BHZ – Bernevig-Hughes-Zhang (Model of a 2D TI)

FMM – Ferromagnetic Metal

CRG – Curvature Renormalization Group

SCTMA – Self Consistent T Matrix Approximation

TB – Tight Binding (Model of a Lattice)

OZ – Ornstein-Zernike

HSP – High Symmetry Point

TRIM – Time Reversal Invariant Momentum

PBC – Periodic Boundary Condition

OBC – Open Boundary Condition

DOS – Density of States

LDOS – Local Density of States

VB – Valence Band

CB – Conduction Band

1
Introduction

Condensed matter physics has always been a practical field where a major driving force behind its development is usually the functionality of materials, starting from the first quantum revolution which is connected to the invention of the transistor, lasers, GPS, semiconductor devices and MRI imagers to the second quantum revolution connected to the Quantum Hall Effect and topological materials. The functionality of materials has often been characterized by their Landau order parameter, for instance superconductivity is used to build MRI and Maglev trains, magnetization to construct hard drives and memory devices. In all these systems it was found that upon tuning certain external handle, such as lowering the temperature or applying a magnetic field, the material undergoes a phase transition into the ordered phase in which a Landau order parameter that breaks a certain continuous symmetry (for instance, superconducting order breaks global $U(1)$ and magnetic order breaks $SO(3)$ symmetry) gradually develops. For a long time this kind of order parameter dominated what is meant by order in condensed matter physics.

In the 1980s the Landau order paradigm was challenged by the discovery of the Quantum Hall Effect (QHE) because this system, rather than breaking a continuous symmetry, breaks a discrete symmetry due to the applied magnetic field, namely the time reversal symmetry [1]. The system consisted of a 2 dimensional electron gas at low temperature in which a strong magnetic field was applied leading to the appearance of the so-called Landau levels. It was found that the Hall Resistivity ρ_{xy} was exactly quantized and moreover, the longitudinal resistivity ρ_{xx} falls down to zero, meaning we have a perfect conductor, but at the edges of the sample. Due to its magnetic translational symmetry, the Hall conductivity can be identified as a topological invariant, representing the topological property of the ground state wave function, leading to the notion of topological order. Another breakthrough comes from the proposal put forward by Haldane in 1988 [2], which shows that there can be systems showing QHE without Landau levels, referred to as the quantum anomalous Hall effect (QAHE). Along this line of development emerges the so-called quantum spin Hall effect (QSHE), in which the equilibrium current

circulating at the edge of the 2D system is a spin current rather than a charge current owing to the time-reversal symmetry. In Chapter 3 of this work, we will present several surprising properties of this edge spin current in QSHE. This quantum spin Hall state of matter is proposed to exist in special, two dimensional semiconductors that exhibit a finite spin-Hall conductance but a vanishing charge-Hall conductance, this was first put forward by Kane and Mele [3] by modifying Haldane's graphene model by incorporating time-reversal symmetry. Independently, a quantum spin Hall model (BHZ model) was proposed by Andrei Bernevig and Shou-cheng Zhang [4] in an intrincate strain architecture which engineers, due to spin-orbit coupling (a kind of momentum-dependent magnetic field coupling to the spin of the electron), a magnetic field pointing in different directions for spins up and down. Later, Kane and Mele introduced a topological $\mathbb{Z}_2$ invariant which characterizes a state (or phase of the system) as trivial or non-trivial band insulator. It was found that the non-trivial state is robust to both interactions and additional spin-orbit coupling terms that mix spin-up and spin-down electrons [5]. This topologically nontrivial phase brings in the notion of topological insulators, which are topologically ordered materials protected by time-reversal symmetry.

Such two-dimensional topological insulators were predicted in 2006 to occur in quantum wells of HgTe sandwiched between CdTe [6], and were observed in 2007 [5]. When the layer of HgTe in between the CdTe is thin, the system behaves as an ordinary insulator. However, when the HgTe is made thicker, the system eventually closes its bulk 2D gap (actually it is the so-called mass gap that closes) at a critical thickness, and then as the thickness is further increased, the gap reopens with an inversion of the well sub-bands. In this band inversion process, two branches of bands are brought out from the bulk bands, forming edge states with a roughly linear dispersion inside the band gap. As a result of these states, the edges of the system actually become metallic. This process of band inversion and corresponding occurrence of edge states in a finite system, is generally referred to as a topological phase transition, which has been verified experimentally [5].

These theoretical and experimental developments introduce the notion of TI and topological phase transition into the realm of condensed matter physics. The topological phase transition is a kind of quantum phase transition, taking place at zero temperature, at which the topological invariant jumps from one integer to another. Depending on the dimension and the kind of discrete symmetry associated with the system, the topologically ordered materials exhibit intriguing properties, and they may have important practical

applications. Fig. 1.1 gives some examples from 1D to 3D, with emphasis on what are called the topological edge states, they are important because, due to their topological protection, they are robust against local perturbations.

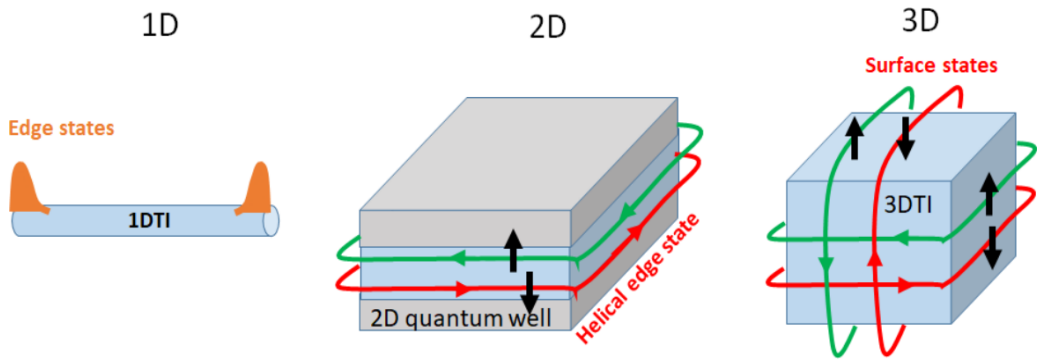

Figure 1.1: Schematics of the edge and surface states in topological insulators. (a) Edge states localized at the end of a 1D topological insulator [7]. (b) Helical edge states consist of counter propagating spins at the edge of 2D time-reversal symmetric topological insulators, which are responsible for the quantum spin Hall effect [4–6, 8, 9]. (c) Surface states at the boundary of 3D topological insulators that also consist of counter propagating spins [3, 10].

In general, the topological order of a band insulator depends on the band structure within the first Brillouin Zone and can appear in any spatial dimension. It has been clarified that at a given dimension, the topological systems can be classified into 10 different symmetry classes according to whether they possess time-reversal T, particle-hole C, and chiral S symmetries [11–14]. The result of this classification determines whether the topological invariant at a given dimension and symmetry class is zero (trivial), binary ($\mathbb{Z}_2$), integer ($\mathbb{Z}$), or even-integer ($2\mathbb{Z}$). The pattern of these topological invariants yields the so-called periodic table of topological materials that repeats every 8 spatial dimensions. Besides, in the topologically nontrivial phase, the system at any dimension exhibits edge states that are localized at the boundary of the sample. These topological edge states have promising applications in spintronic devices and dissipationless transistors due to their robustness, for example the robust edge states of 1D TIs and 1D topological superconductors (TSCs) become useful in quantum computation because they are not subjected to decoherence as is the usual case for many other systems. In the case of 2D TIs, edge states are relevant since it has been shown that magnetic components, like the ones in spin-torque computer memory, can be manipulated by topological insulators [15].

Our contribution to this already well-established field consists of two

different but complementary projects. The first project is detailed in Chapter 2 and was related to the study of a 1D TI known as the Su-Schrieffer-Heeger (SSH) model, it has been used as a model for the polyacetilene molecule. The main motivation of this project was theoretical. Here we developed a tool which allows us to calculate and study the edge states of the system in the presence of interactions. The tool developed is a combination of Dyson's equation (to calculate the interacting Green's function) together with the T-matrix approximation (to account for the presence of a strong-impurity potential which effectively creates an edge). In Section 2.1 we start by reviewing the main features of the SSH model. We also take a look at the 3 main symmetries a Dirac Hamiltonian can have, how they appear in this system and study the critical behavior of the system near a topological phase transition, which is a general feature of TIs and TSCs. In Section 2.2 it is shown how to introduce interactions in the system and to calculate its Green's function using results from many body theory. Section 2.3 shows how, from the local density of states, we can identify the bulk-edge correspondence and investigate quantum criticality for interacting 1D TIs.

The second project, detailed in Chapter 3, consisted in the investigation of a 2D TI, known as the Bernevig-Hughes-Zhang (BHZ) model, making a planar junction in contact with a Ferromagnetic-Metal(FMM). In this case, the motivation was the importance this system may have for applications in spintronics. Due to the percolation of the BHZ edge states into the FMM, we have unveiled interesting physical effects like local charge and spin currents near the interface and spin accumulation, which produces a torque on the magnetization of the FMM. After a brief motivation introduced in Section 3.1, we then review time reversal symmetry in Section 3.2, since this symmetry is what allows us to study the topology of this system and protects its topological edge states. Section 3.3 explains in detail the way the system was simulated using a lattice model, this allowed us to study its band structure, percolation of edge states, the local laminar flows of charge and spin currents and, with the aid of linear response theory, the current induced spin-torque. In this second project we needed to be careful with the choice of parameters due to the finite size of the lattice and it represented an approach complementary to the one of our first project.

It is relevant here to mention some important features related to the spin torque in general, due to its important applications and because it is a field of research by itself. The subject of spin torque has been a very active field since the seminal proposal of spin-transfer torque in ferromagnet/normal

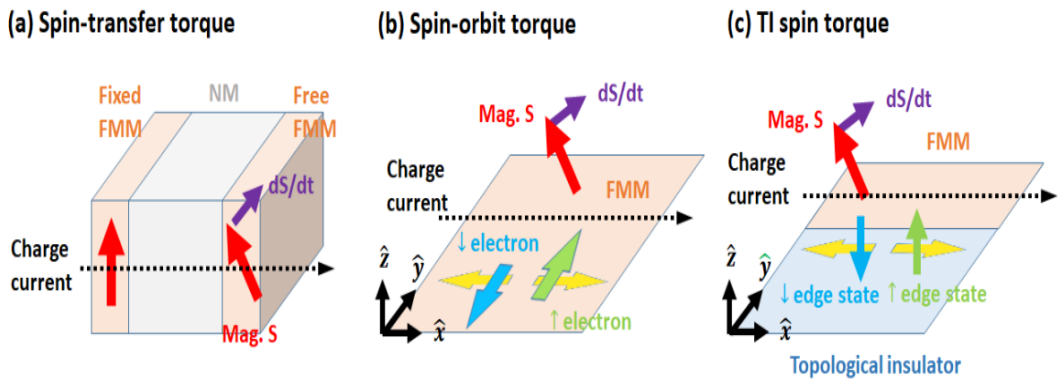

Figure 1.2: Schematics of several mechanisms for current-induced spin torque: (a) The spin-transfer torque in FMM/NM/FMM trilayer based on the spin relaxation. (b) The spin-orbit torque in a 2D FMM with Rashba spin-orbit coupling, where the spin of the electron (blue and gree arrows) depends on the momentum (yellow arrows). Note that the spin quantization remains in-plane. (c) The TI spin torque in a 2D TI/FMM junction based on the percolation of helical edge states, whose spin quantization axis is out-of-plane. In (b) and (c), the momentum-dependence of spin polarization is known as the spin-momentum locking.

metal/ferromagnet trilayers in the current-perpendicular-to-the-plane (CPP) geometry [16, 17], in which the electrons spin polarized by the fixed ferromagnetic layer yields a spin torque to the free ferromagnetic layer via spin relaxation, as shown in Fig. 1.2 (a). Another relevant mechanism is the so-called spin-orbit torque in ferromagnetic thin films in the current-in-plane (CIP) geometry, in which a charge current creates a spin polarization due to spin-momentum locking, thereby exerting a spin torque on the magnetization [18, 19], as illustrated in Fig. 1.2 (b). Besides these two mechanisms in metallic thin films that have found their applications in magnetic memory devices, it has been demonstrated recently that topological insulators can also be used to generate current-induced spin torque [15, 20], as shown schematically in Fig. 1.2 (c). In fact, topological insulators can even outperform the metallic thin films in terms of the efficiency of the torque, which has triggered a great deal of theoretical studies for the underlying mechanism [21–26]. In essence, this spin torque originates from the spin-momentum locking of the topological edge states, whose percolation into the adjacent ferromagnet causes the torque. Using a lattice model for the 2D version of this problem, we demonstrated how the percolation causes a predominantly field-like torque defined with respect to the spin quantization axis of the edge state which points out-of-plane. Moreover, we have found that impurities have a dramatic effect on the magnitude of the spin torque.

2
Corroborating the bulk-edge correspondence in weakly interacting one-dimensional topological insulators

In this Chapter we present a review of the theory, calculations and results that were developed in our first project that resulted in our first paper entitled **Corroborating the bulk-edge correspondence in weakly interacting one-dimensional topological insulators** [27] and here we will follow very closely what we have written there. We start in Section 2.1 by considering the 1D-lattice-model for the SSH system without interactions, and explain the way in which the topological invariant is calculated. We will introduce the concept of **bulk-edge correspondence**, which means the occurrence of edge states in the topologically nontrivial phase in a finite geometry. Moreover, we will introduce the framework within which critical exponents can characterize topological phase transitions. Later on, in Section 2.2, we introduce interactions between electrons in the lattice, considering a density-density nearest-neighbors specific kind of interaction. In this case the topology needs to be calculated in a different manner. For this reason, we focus on the calculation of the system Green's function which allows us to introduce interactions and treat them via a Dyson's series expansion, as long as they are weak enough. In order to effectively create an edge, to calculate the edge state and verify the bulk-edge correspondence, we introduce an impurity with a large potential into the system and treat this case by means of the T-matrix formalism (also known as the self consistent T-matrix approximation or SCTMA) in Section 2.3.

2.1
Non-interacting SSH model

We work mainly with lattice models whose fermion operator is defined on discrete lattice sites labeled by i, and we include also another quantum number α which stands for spin, orbital or sublattice (more generally a pseudospin) degree of freedom, so we have creation and annihilation operators $c_{i\alpha}, c_{i\alpha}^{\dagger}$. Since we only will be concerned with fermions, the commutation relation they obey is

$$\{c_{i\alpha}, c_{j\beta}^{\dagger}\} = c_{i\alpha}c_{j\beta}^{\dagger} + c_{j\beta}^{\dagger}c_{i\alpha} = \delta_{ij}\delta_{\alpha\beta}$$

and this make the proper wave-function of the system automatically antisymmetric under particle-exchange, the corresponding Fourier transform of these operators can be obtained as

$$c_{i\alpha} = \sum_{\mathbf{k}} e^{i\mathbf{k}\cdot\mathbf{r}_i} c_{\mathbf{k}\alpha}, \qquad c_{i\alpha}^{\dagger} = \sum_{\mathbf{k}} e^{-i\mathbf{k}\cdot\mathbf{r}_i} c_{\mathbf{k}\alpha}^{\dagger}.$$

Within this second quantization formalism the Hamiltonian of the entire lattice model can be written in real-space or momentum-space as

$$H = \sum_{ij,\alpha\beta} c_{i\alpha}^{\dagger} H_{ij,\alpha\beta} c_{j\beta} = \sum_{\alpha\beta}\sum_{\mathbf{k}} c_{\mathbf{k}\alpha}^{\dagger} H_{\alpha\beta}(\mathbf{k}) c_{\mathbf{k}\beta}, \tag{2-1}$$

where the matrix elements $H_{ij,\alpha\beta}$ contain some hopping terms connecting sites i and j, or local potentials on site i, etc, and here we consider $j = i + \delta$. In all the models that we treat, $H_{\alpha\beta}(\mathbf{k})$ takes the form of a so-called **Dirac Hamiltonian** as explained later in detail. In particular, for the SSH model we have 2 degrees of freedom for each lattice-site which stands for the specific sublattice index.

For 1D lattice models, the topology is described by the so-called **Zak phase**, which is equivalent to the Berry phase accumulated by the adiabatic evolution of a Bloch state across the first Brilloin zone (BZ). Since the ends of the BZ $k = 0$ and $k = 2\pi$ are the same point, the evolution is cyclic and this BZ is a compact manifold. The Zak phase is calculated by the integration of the Berry connection

$$\mathcal{C} = \int_{BZ} dk \sum_{n} \langle u_{nk} | i\partial_k | u_{nk} \rangle, \tag{2-2}$$

where the summation over n denotes the filled bands and $|u_{nk}\rangle$ are the Bloch states which are periodic in the lattice and whose Fourier transform $|\mathbf{R}n\rangle$ are the so called Wannier states

$$|u_{n\mathbf{k}}\rangle = \frac{1}{N}\sum_{\mathbf{R}} e^{-i\mathbf{k}\cdot(\mathbf{r}-\mathbf{R})} |\mathbf{R}n\rangle, \quad |\mathbf{R}n\rangle = \int d\mathbf{k} e^{-i\mathbf{k}\cdot(\mathbf{r}-\mathbf{R})} |u_{n\mathbf{k}}\rangle, \tag{2-3}$$

where $\langle \mathbf{r}|\mathbf{R}n\rangle = W_n(\mathbf{r}-\mathbf{R})$ is a wave function localized around lattice site $\mathbf{R}$. It may be relevant here to mention that in the language of the Wannier states, defined previously, the Zak phase measures the center of charge of the Wannier state centered at the origin of the lattice. Moreover, if instead of integrating the Berry connection to obtain the Zak phase, we consider the Fourier transform of the Berry connection, then the result is a Wannier state correlation function λ_R

that characterizes the critical behavior near the topological phase transitions. We write these definitions as

$$\mathcal{C} = \int_{BZ} dk \sum_n \langle u_{nk}|i\partial_k|u_{nk}\rangle = \sum_n \langle 0n|r|0n\rangle,$$

$$\lambda_R = \int_{BZ} dk \sum_n e^{ikR}\langle u_{nk}|i\partial_k|u_{nk}\rangle = \sum_n \langle Rn|r|0n\rangle. \tag{2-4}$$

Now we introduce which is perhaps the simplest model of topological insulators, namely the celebrated **Su-Shrieffer-Heeger (SSH) model** [7]. The model considers spinless fermions with periodic boundary condition (PBC), described by the Hamiltonian

$$H = \sum_i \{(t+\delta t)c^\dagger_{Ai}c_{Bi} + (t-\delta t)c^\dagger_{Ai+1}c_{Bi} + h.c.\}, \tag{2-5}$$

which upon a Fourier tranform to momentum space (here r_i stands for the position in real space of lattice site i)

$$c_{Ai} = \sum_k e^{ikr_i}c_{Ak}, \quad c^\dagger_{Ai} = \sum_k e^{-ikr_i}c^\dagger_{Ak}, \tag{2-6}$$

becomes

$$H = \sum_k [(t+\delta t) + (t-\delta t)e^{-ik}]c^\dagger_{Ak}c_{Bk} + [(t+\delta t) + (t-\delta t)e^{ik}]c^\dagger_{Bk}c_{Ak}$$

$$= \sum_k \begin{pmatrix} c^\dagger_{Ak} & c^\dagger_{Bk} \end{pmatrix} \begin{pmatrix} 0 & (t+\delta t) + (t-\delta t)e^{-ik} \\ (t+\delta t) + (t-\delta t)e^{ik} & 0 \end{pmatrix} \begin{pmatrix} c_{Ak} \\ c_{Bk} \end{pmatrix}$$

$$= \sum_k \begin{pmatrix} c^\dagger_{Ak} & c^\dagger_{Bk} \end{pmatrix} \mathbf{d}\cdot\boldsymbol{\sigma} \begin{pmatrix} c_{Ak} \\ c_{Bk} \end{pmatrix}, \tag{2-7}$$

where $H(k) = \mathbf{d}\cdot\sigma$ is the Dirac Hamiltonian for the SSH-model, $\boldsymbol{\sigma}$ is the vector of Pauli matrices and $\mathbf{d}$ a k-dependent vector with components

$$d_1 = (t+\delta t) + (t-\delta t)\cos(k), \quad d_2 = (t-\delta t)\sin(k), \quad d_3 = 0, \tag{2-8}$$

where the component $d_3 = 0$ because the system has chiral symmetry ($\{H, \sigma_3\} = 0$). Figure 2.1 shows a schematic representation of the SSH chain with a periodic boundary condition (PBC) forming a ring with toroidal symmetry. The difference of hopping δt distinguishes two sublattices A and B in each unit cell located at site i. The appearence of edge states depends on where we decide to cut the chain, the band structure of this model is also shown on the right of Figure 2.1, where we can see the conduction and valence bands together with the high symmetry point $k_0 = \pi$ at which the band gap closes at the topological phase transition.

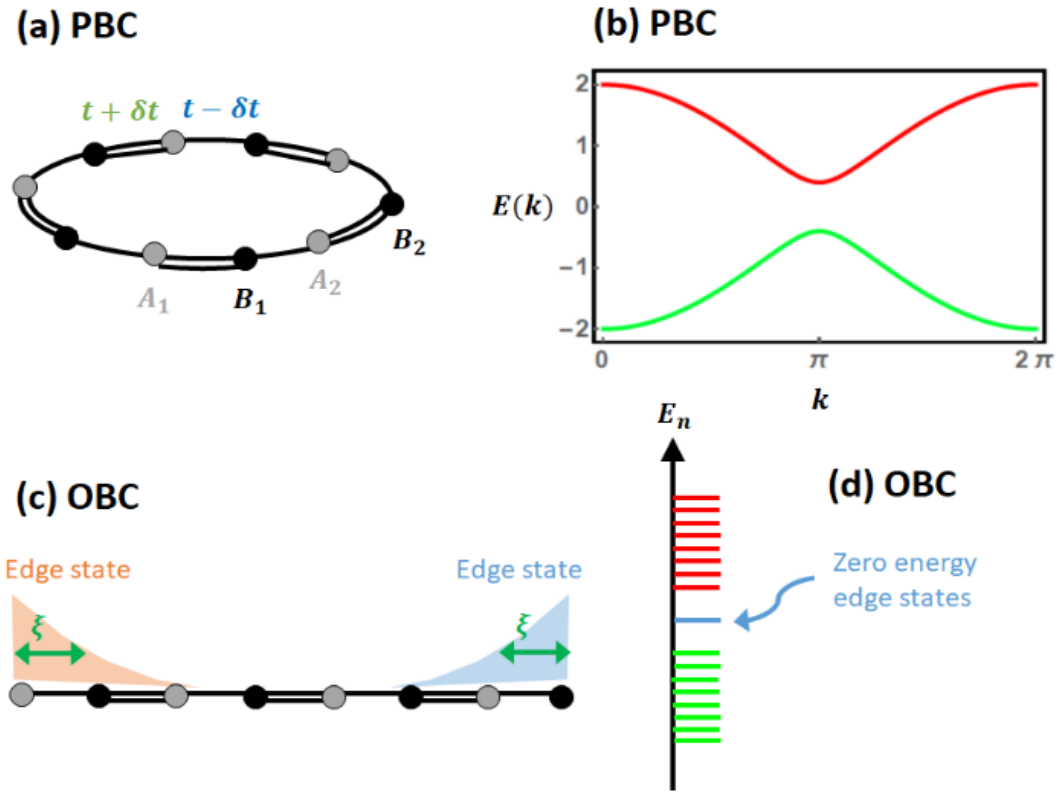

Figure 2.1: (a) Schematics of the SSH model with PBC, where the difference of hopping on the even and odd bonds distinguishes two sublattices A and B. (b) The band structure of the SSH model, which has a band gap $2\delta t$ at $k = \pi$. (c) The SSH model with OBC, where the unpaired electrons at the edge form the edge states with decay length ξ. (d) The discrete energy spectrum E_n in OBC, where the edge state shows up as zero energy eigenstate.

As explained in Eq. (2-2), the topology of this model is given by the Zak phase which is calculated from the integration of Berry connection. In this model, the Berry phase is equivalent to the winding number of the phase of the off-diagonal element of the Dirac Hamiltonian. Denoting this off-diagonal element as $h_k(\delta t) = (t+\delta t) + (t-\delta t)e^{-ik} = |h_k(\delta t)|e^{-i\varphi_k(\delta t)}$ in the complex space where one goes through the entire BZ, we define its phase from $q_k = h_k/|h_k| = e^{-i\varphi_k(\delta t)}$. It then follows that the winding of the phase can be calculated as [28]

$$\mathcal{C} = \frac{i}{2\pi}\oint dk(q_k^{-1}\partial_k q_k) = \frac{1}{2\pi}\oint dk\partial_k\varphi_k(\delta t). \tag{2-9}$$

Generally, when we express the topological invariant as a momentum integration over the BZ, the integrand is referred to as the curvature function. In the case of SSH model, the curvature function is the Berry connection, and equivalently the gradient of the phase φ_k. The curvature function for the SSH

model is, with an additional factor of -2 for the sake of normalization

$$F(k,\delta t) = -2i < \psi_-|\partial_k|\psi_- >= \frac{(t^2-\delta t^2)\cos(k)+(t-\delta t)^2}{(t+\delta t)^2+2(t^2-\delta t^2)\cos(k)+(t-\delta t)^2}, \tag{2-10}$$

where the state $|\psi_- >$ corresponds to the valence band. The topological invariant $\mathcal{C}$ can be calculated by a contour integration

$$\mathcal{C} = \int_0^{2\pi}\frac{dk}{2\pi}F(k,\delta t) = \int_0^{2\pi}\frac{dk}{2\pi}[\frac{c}{a+b\cos(k)}+\frac{d\cos(k)}{a+b\cos(k)}] \tag{2-11}$$

where $a = 2(t^2+\delta t^2), b = 2(t^2-\delta t^2), c = (t-\delta t)^2, d = t^2-\delta t^2$. The result, after doing the contour integration is

$$\mathcal{C} = \frac{1}{2}(1-\frac{t\delta t}{|t\delta t|}) = \begin{cases} 0 & t\delta t > 0, \\ 1 & t\delta < 0 \end{cases} \tag{2-12}$$

so the **critical point** is located at $\delta t_c = 0$ (δt is the tunning parameter). From the value calculated for $\mathcal{C}$, we identify $t\delta t < 0$ as the topologically nontrivial phase and $t\delta t > 0$ as the trivial one.

Before proceding further, let us mention that we can also study this SSH noninteracting system using a Green's function formalism. This formalism is particularly relevant because later we will use it to introduce interactions. The Green's function method allows us to introduce interactions by finding the full approximate Green's function of the interacting system via Dyson's equation. For the noninteracting SSH model, the Matsubara (complex frequency) Green's function $G_0(k,i\omega)$ matrix can be calculated (the very definition for the general case is given later in Eq. (2-39) and Eq. (2-40)) from the Dirac Hamiltonian $H_0(k)$ and reads

$$\begin{aligned} G_0(k,i\omega) = (i\omega - H_0)^{-1} &= \frac{1}{(i\omega)^2-d^2}\times\begin{pmatrix} i\omega+d_3 & d_1-id_2 \\ d_1+id_2 & i\omega-d_3 \end{pmatrix}, \\ G_0^{-1}(k,i\omega) &= \begin{pmatrix} i\omega-d_3 & -d_1+id_2 \\ -d_1-id_2 & i\omega+d_3 \end{pmatrix}. \end{aligned} \tag{2-13}$$

From this Green's function we can calculate relevant physical quantities after performing an analytical continuation ($i\omega \to \omega+i\eta$) to get the retarded Green's function in terms of real frequency $G_0^{ret}(k,\omega)$. The physical meaning of this so-called analytical continuation is to create an integration contour that defines a direction of time which respects causality. A particularly important quantity is

the spectral function, which allows the calculation of the energy gap in terms of the external tunning parameters, and the local density of states (LDOS), from which we can calculate the edge state and its decay or correlation length ξ, a quantity that we show below how to obtain by means of an ansatz. Moreover, with the aid of this Green's function, we can also calculate the topological invariant $\mathcal{C}$ as a momentum integral over the BZ of a function that is expressed in terms of G_0 and its derivatives [29]

$$\mathcal{C} = \int_0^{2\pi} \frac{dk}{4\pi i} Tr(\sigma_3 G_0^{-1} \partial_k G_0)|_{i\omega=0}. \tag{2-14}$$

It is possible to verify that this is actually a winding number and can be written in the same fashion as Eq. (2-9), which is obtained from the very definition of Zak phase. Later on, when introducing interactions into the system, we will just need to replace G_0 by the G_{int} (obtained from Dyson's equation) in this more general definition for the topological invariant. It will be shown that the effect of introducing interactions will be embeded in the self energy, which is responsible for changing the phase that gives the winding number. This self energy will also renormalize the $\vec{d}$ vector to a new one $\vec{d'}$, thus modifying in this way the effective Dirac Hamiltonian of the system, and inducing an effective chemical potential d'_0 that shifts the whole energy band spectrum as is explained later.

To calculate explicitly the **edge state** of the SSH model, we make use of the Dirac Hamiltonian in real space near the critical point. In a neighborhood around the critical point, the band gap closes at the so-called High Symmetry Point HSP $k_0 = \pi$. We perform an expansion around this point of the components $d_i(k)$

$$d_1 \approx (t+\delta t) + (t-\delta t)(-1+\frac{k^2}{2}) = 2\delta t + (t-\delta t)\frac{k^2}{2}, \quad d_2 \approx -(t-\delta t)k, \tag{2-15}$$

and we look for the **zero-energy-solution** $H(\hat{k} = -i\partial_x)\psi(x) = 0$

$$\mathbf{d}\cdot\boldsymbol{\sigma}\psi(x) = \{-(t-\delta t)\hat{k}\sigma_2 + [2\delta t + (t-\delta t)\frac{\hat{k}^2}{2}]\sigma_1\}\psi(x) = 0. \tag{2-16}$$

Multiplying by σ_2

$$\{-(t-\delta t)\hat{k} + [2\delta t + (t-\delta t)\frac{\hat{k}^2}{2}](-i)\sigma_3\}\psi(x) = 0, \tag{2-17}$$

and since $\psi(x) = \phi(x)\chi_\eta$ then the spinor χ_η (in this lattice-sublattice pseudo-spin space) is an eigenstate of $\sigma_3 = \sigma_z$: $\sigma_3\chi_\eta = \eta\chi_\eta$. The meaning of having $\eta = \pm 1$ for which $\chi_+ = (1,0)^T, \chi_- = (0,1)^T$ indicates the sub-lattice at

which the edge state is localized. The spatial(orbital) part then satisfies, using $\hat{k} = -i\partial_x$

$$\{(t-\delta t)\partial_x - [2\delta t - (t-\delta t)\frac{\partial_x^2}{2}]\eta\}\phi(x) = 0 \tag{2-18}$$

To solve the spatial part we consider the ansatz $\phi(x) \propto e^{-\lambda x}$ where $\lambda = 1/\xi$ is the inverse of the **decay lenght** ξ and satisfies

$$\lambda^2 - 2\eta\lambda - \frac{4\delta t}{t-\delta t} = 0 \quad \rightarrow \quad \lambda_\pm = \eta \pm + \sqrt{1 + \frac{4\delta t}{t-\delta t}}. \tag{2-19}$$

The decay or correlation length is positive by definition, so we impose that $\lambda_+ + \lambda_- = 2\eta > 0$, hence $\eta = 1$, this implies that the edge state $\chi_+ = (1,0)^T$ is localized on the A sublattice. Furthermore, we consider the model to be defined in the $x > 0$ subspace, so the wave function must vanish at $x = 0$. This is actually equivalent to introducing a strong impurity at that site which effectively creates an edge as is explained later when discussing the interacting system. From this we obtain, considering $\lambda_\pm = \xi_\pm^{-1}$, that

$$\psi(x) \propto \begin{pmatrix} 1 \\ 0 \end{pmatrix} (e^{-x/\xi_+} - e^{-x/\xi_-}). \tag{2-20}$$

It is important here to take a closer look at the two decay lengths $\xi_\pm^{-1}$. To do this, we consider the hopping to be actually small (so we are close to the critical point) $|\delta t| \ll |t|$, then

$$\xi_-^{-1} = 1 - \sqrt{1 + \frac{4\delta t}{t-\delta t}} \approx -\frac{2\delta t}{t-\delta t}, \quad \xi_+^{-1} \approx 2 + \frac{2\delta t}{t-\delta t}. \tag{2-21}$$

From Eq. (2-21) it is evident that $\xi_+^{-1} > \xi_-^{-1}$, so the longer decay length ξ_- is identified as the actual decay length. Moreover, we see that in order to make ξ_- positive, we must have $\delta t/t < 0$, meaning that **only the topologically non-trivial phase has edge state**. This is what is known as the **bulk-edge correspondence** for the non-interacting SSH model and it is important due to its potential applications such as in quantum computation [30] or spintronic devices [31].

2.1.1 Symmetries of the Non-interacting SSH model

It is relevant to mention the three non-spatial symmetries that are used to classify TIs and TSCs, these are the **time-reversal** T, **particle-hole** C and **chiral** S. They are important because they are the ones that generally bring topological protection to the system. We know that the Hamiltonian operator, as in Equation 2-1, is written generically as $H = \sum_{\mathbf{k}} \psi_{\mathbf{k}}^\dagger H(\mathbf{k}) \psi_{\mathbf{k}}$ where $\psi_{\mathbf{k}}$ is the spinor and $H(\mathbf{k})$ the Dirac Hamiltonian. If the Hamiltonian operator preserves

each of these symmetries then the Dirac Hamiltonian transforms as

$$TR: \quad TH(\mathbf{k})T^{-1} = H(-\mathbf{k}), \quad T^2 = \pm 1,$$

$$PH: \quad CH(\mathbf{k})C^{-1} = -H(-\mathbf{k}), \quad C^2 = \pm 1,$$

$$Chiral: \quad SH(\mathbf{k})S^{-1} = -H(\mathbf{k}), \quad S \propto TC. \tag{2-22}$$

These symmetries put some constraints in the Dirac Hamiltonian. Generically, one may consider a Dirac Hamiltonian in D-dimension as the low energy effective theory of a TI or TSC expanded around a HSP

$$H(\mathbf{k}) = \sum_{i=1}^{D} vk_i\gamma_i + M\gamma_0, \tag{2-23}$$

where $\mathbf{k}$ denotes the momentum deviation away from the HSP $\mathbf{k}_0$, v is a velocity scale(the slope of the Dirac cone), and the γ_i matrices satisfy the Clifford algebra $\{\gamma_i, \gamma_j\} = 2\delta_{ij}$ with $\gamma_i^2 = 1$. It is possible to show that for certain symmetries to be satisfied the γ_i matrices are restricted to satisfy certain commutation or anticommutation relations with the operators T, C and S.

Introducing the concept of surface Hamiltonian and extra mass term it is possible to analyze if a system is topologically trivial or not depending if this extra mass term gaps out the surface spectrum or not. One may further determine whether the topological invariant in a symmetry class is binary $\mathbb{Z}_2$, meaning that $\mathcal{C} = \{-1, 0, 1\}$ or integer $\mathbb{Z}$, meaning that $\mathcal{C}$ takes all possible integer values. Following this and a more general argument, the topological invariant in the ten symmetry classes in each spatial dimension has been classified in what has been called the periodic table of TIs and TSCs [13], [14] which shows certain periodicity with respect to dimension.

For the case of the non-interacting SSH model we deal with a specific case of a 2×2 **homogeneous Dirac model** (translational invariant) whose most general form is

$$\mathcal{H}_0 = \sum_k \begin{pmatrix} c_{Ak}^\dagger & c_{Bk}^\dagger \end{pmatrix} H_0(k) \begin{pmatrix} c_{Ak} \\ c_{Bk} \end{pmatrix}$$

$$H_0(k) = -d_0(k)\sigma_0 + d_1(k)\sigma_1 + d_2(k)\sigma_2 + d_3(k)\sigma_3 \tag{2-24}$$

where $c_{Ik}^\dagger(c_{Ik})$ with $\{c_{Ik}, c_{Ik}^\dagger\} = \delta_{II'}\delta_{kk'}$ denotes the creation (annihilation) operator of spinless fermion with momentum k and $I = A, B$ the sublattice degree of freedom. The presence of each $d_i(k)$ and their evenness and oddness in

k are determined by the Hamiltonian symmetry class. In our work the system under analysis belongs to **class BDI**, which in general can host topological trivial and nontrivial edge states, mainly due to the presence of the chiral symmetry. Let us verify explicitly that the SSH model satisfies all these 3 symmetries. To do this, we consider the Dirac Hamiltonian matrix $H_0(k)$ in explicit form as shown in Eq. (2-24) and the form of the 3 symmetry operators. In this case T is just the complex conjugate operator K, since we deal with spinless fermions $T = K$, $C = \sigma_z K$ and $S = \sigma_z$ so we have

$$\begin{aligned} TH_0(k)T^{-1} = \quad & K \begin{pmatrix} 0 & (t+\delta t)+(t-\delta t)e^{-ik} \\ (t+\delta t)+(t-\delta t)e^{ik} & 0 \end{pmatrix} K \\ & = \begin{pmatrix} 0 & (t+\delta t)+(t-\delta t)e^{ik} \\ (t+\delta t)+(t-\delta t)e^{-ik} & 0 \end{pmatrix} \\ & = H_0(-k), \end{aligned} \tag{2-25}$$

$$\begin{aligned} CH_0(k)C^{-1} = \quad & \sigma_z K \begin{pmatrix} 0 & (t+\delta t)+(t-\delta t)e^{-ik} \\ (t+\delta t)+(t-\delta t)e^{ik} & 0 \end{pmatrix} K\sigma_z \\ & = \sigma_z \begin{pmatrix} 0 & (t+\delta t)+(t-\delta t)e^{ik} \\ (t+\delta t)+(t-\delta t)e^{-ik} & 0 \end{pmatrix} \sigma_z \\ & = \sigma_z \begin{pmatrix} 0 & -\{(t+\delta t)+(t-\delta t)e^{ik}\} \\ (t+\delta t)+(t-\delta t)e^{-ik} & 0 \end{pmatrix} \\ & = \begin{pmatrix} 0 & -\{(t+\delta t)+(t-\delta t)e^{ik}\} \\ -\{(t+\delta t)+(t-\delta t)e^{-ik}\} & 0 \end{pmatrix} \\ & = -H_0(-k), \end{aligned} \tag{2-26}$$

$$\begin{aligned} SH_0(k)S^{-1} = \quad & \sigma_z \begin{pmatrix} 0 & (t+\delta t)+(t-\delta t)e^{-ik} \\ (t+\delta t)+(t-\delta t)e^{ik} & 0 \end{pmatrix} \sigma_z \\ & = \sigma_z \begin{pmatrix} 0 & -\{(t+\delta t)+(t-\delta t)e^{-ik}\} \\ (t+\delta t)+(t-\delta t)e^{ik} & 0 \end{pmatrix} \\ & = \begin{pmatrix} 0 & -\{(t+\delta t)+(t-\delta t)e^{-ik}\} \\ -\{(t+\delta t)+(t-\delta t)e^{ik}\} & 0 \end{pmatrix} \\ & = -H_0(k). \end{aligned} \tag{2-27}$$

This symmetry class that requires time reversal ($T^2 = +1$), particle-

hole ($C^2 = +1$) and chiral (S) symmetries, implies constraints on the $d_i(k)$ components such that

$$d_0(k) = d_3(k) = 0, \quad d_1(k) = d_1(-k), \quad d_2(k) = -d_2(-k). \tag{2-28}$$

It is relevant to mention here that since we have $T^2 = +1$ for this SSH model, they seem to be bosons. However, we should keep in mind that this model considers spinless fermions (which do not exist in reality) so they are effectively bosons, we can accept this without any contradiction since we are dealing with just a toy model for the SSH.

2.1.2 Topological Phase Transition and Critical behavior of the Non-interacting SSH model

The topological order is a property of the Bloch state of the n-th band $|u_{nk}\rangle$, and based on the dimension (here our system is one-dimensional) and symmetry class of the system (of the Dirac Hamiltonian), the topological invariant $\mathcal{C}$ is found from $|u_{nk}\rangle$ considering different schemes (by means of Berry connection, Berry curvature or Pfaffian). In all schemes of calculating topology, $\mathcal{C} = \mathcal{C}(M)$ takes only integer values and depends on tuning energy parameters M ($M = \delta t$ for the non-interacting SSH model) that appear in the Hamiltonian. The discrete change of $\mathcal{C}$ caused by tuning $M = \delta t$ across the critical point $M_c = \delta t_c = 0$ defines a specific kind of quantum phase transition called topological phase transition.

In all different ways of investigating the topology of the system, the topological invariant which characterizes the topological phase transition, can be written as an integral over a compact manifold (the first BZ) in momentum space and can be written as

$$\mathcal{C} = \int_{BZ} dk F(k, M). \tag{2-29}$$

The function $F(k, M)$, a function already demonstrated for the SSH model in Eq. (2-10), is defined as the curvature function, meaning that the integration of the curvature of a closed string counts the number of knots (or holes in a more general context where we integrate over a compact manifold where the curvature is defined at each of its points). The actual form of $F(k, M)$, similarly to the previously shown Berry-connection for the SSH model, depends on the specific scheme used for calculating the topological invariant but it is usually even around the HSP ($k_0 = \pi$ for the SSH model)

$$F(k_0 + \delta k, M) = F(k_0 - \delta k, M), \tag{2-30}$$

this eveness being a consequence of a specific symmetry like, for example, inversion or time-reversal. Within a given topological phase in the parameter space of M (δt for the SSH model), the topological invariant $\mathcal{C}$ is constant. However, the momentum space profile of the curvature function $F(k, M)$ varies with M. This is a key point to many statistical properties of topological phase transitions. In addition, we have seen that the topological invariant calculated in each scheme is closely related to the Wannier states $|Rn\rangle$ already introduced in Equation 2-3.

For systems described within the context of the Landau order parameter, the index measuring the closeness of the system to a second-order phase transition is the correlation between two local order parameters located at a certain distance apart. For example, in the celebrated Ising model, the spin-spin correlation function $< s_i s_j >$ decays with a correlation length ξ which turns out to diverge at the critical point. In TIs and TSCs, it is found that the proper quantity characterizing how close the system is to a topological phase transition, is a so-called correlation function measuring the overlap of Wannier states that are separated a given distance in the lattice. We could also ellaborate this point by taking into account the Fourier transform of the curvature function

$$\lambda_R = \int_{BZ} dk e^{ikR} F(k, M) = \langle R|\hat{r}|0\rangle. \tag{2-31}$$

In all the schemes for calculating the topological invariant, the Wannier state correlation function λ_R is related to the overlap between the Wannier states $|0\rangle$ centered at the origin and $|R\rangle$ centered at R, sandwiched by a certain (position)operator $\hat{r}$ which depends on the specific form of $F(k, M)$. According to the particular scheme considered, the two Wannier states could have the same or different band index n. We will show later that λ_R decays with a correlation length due to a very significant property of topological phase transitions, which is the divergence of the curvature function as $M \to M_c$. These correlation lengths follow from the scale invariance of the system at the critical point and fixed point in a scaling scheme within the context of the so called Renormalization Group (RG) approach.

There are two important physical phenomena that occur at a topological phase transition, these are: **(1) Gap-closing and reopening** and **(2) Divergence of the curvature function**, this last one being the most

important and related to the **critical behavior** and **scaling laws** of **critical exponents**. These two features are described below.

(1) Gap-closing and reopening: The critical behavior of a TI or TSC near topological phase transitions is dictacted by the low energy sector of the system, which is described by a Dirac model. Usually, one may consider a Dirac Hamiltonian in D-dimension as the low energy effective theory of a TI or TSC expanded around the HSP as is shown in Equation 2-23. Considering $H(\mathbf{k})^2\psi = E^2\psi$, the dispersion relation for this model is

$$E_{\pm} = \pm\sqrt{\sum_{i=1}^{D} v^2 k_i^2 + M^2}. \tag{2-32}$$

For all schemes of calculating the topological invariant $\mathcal{C}$, the topological phase transition is driven by the sign change of the tuning parameter M, that plays the role of the mass term in the generic Dirac Hamiltonian in Equation 2-23. More specifically, when M is continuously tuned from some positive to some negative value or vice versa (for example if an experimentalist continuously tunes the magnetic field or chemical potential), $\mathcal{C}$ jumps discretely at the critical point M_c ($\delta t_c = 0$ for the SSH). Equation 2-32 implies an obvious consequence of this continuous tuning of M which is the closing and reopening of the **band gap** $\Delta = E_+(\mathbf{k}_0) - E_-(\mathbf{k}_0) = 2|M|$ at the HSP (Figure 2.1 (b) shows the band structure of the SSH model and Figure 2.2 shows the closing and reopening of the band gap where the edge state only appears at the topologically nontrivial phase $\delta t < 0$). In other words, topological phase transitions necessarily involve gap-closing, which is an important feature relevant to experimental measurements. In spite of being an important signature, we must point out that the converse does not necessarily happen, i.e., gap-closing of an arbitrarily given model from variation of a tuning a parameter does not mean the system is approaching a topological phase transition, this is because the low energy sector of the arbitrary model is not necessarily described by a Dirac Hamiltonian.

(2) Divergence of the curvature function: Keeping in mind that gap-closing does not necessarily imply a topological phase transition, we should look for other more rigorous and definite properties to study the critical behavior near this kind of phase transition. We could think that the most rigorous scenario would be to focus on the investigation of the quantity defining the topology, namely the topological invariant $\mathcal{C}$, this from to the fact that there is no order parameter in topological phase transitions. However, this topological invariant remains constant inside each topological phase and jumps discretely across the critical point M_c, thereby not showing any kind of asymptotic

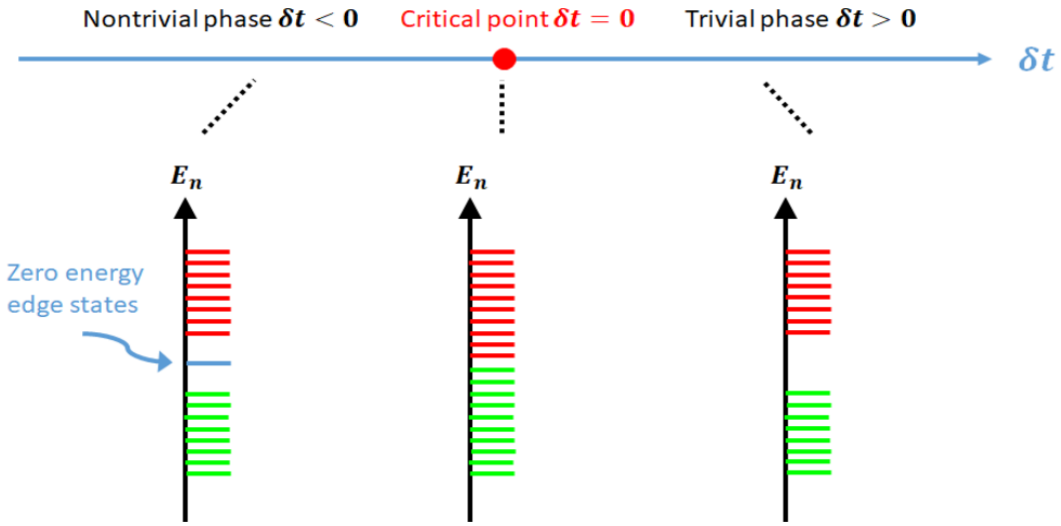

Figure 2.2: Schematics of inversion of discrete energy levels of SSH model with open boundary condition, where only in the topologically nontrivial phase at $\delta t < 0$ does the edge state appear at zero energy.

critical behavior we could analyze. Furthermore, since the topological invariant is calculated from the integration in momentum space of a curvature function, as described by Equation 2-31, the critical behavior seems to be embeded in the curvature function $F(k, M = \delta t)$. This implies, together with the gap-closing at the HSP discussed previously, that the behavior of the curvature function near the HSP is fundamental to investigate the critical phenomena of the system. If we take a look at different Dirac models in different dimensions and consider their different schemes to calculate $\mathcal{C}$, we find that the critical behavior of the curvature function in most of the topological materials falls into a category that has been called as the peak divergence scenario. Within this category the curvature function near the HSP can be fitted very well by an Ornstein-Zernike (OZ) form (a Lorentzian)

$$F(k_0 + \delta k, \delta t) = \frac{F(k_0 = \pi, \delta t)}{(1 + \xi^2 \delta k^2)}, \tag{2-33}$$

where δk stands for the distance away from the HSP $k_0 = \pi$. This fitting can be confirmed from the explicit form of $F(k, \delta t)$ in Equation 2-10 where proper expansion around the HSP gives

$$F(k_0 = \pi, \delta t) = \frac{\delta t - t}{2\delta t}, \quad \xi = |\frac{t}{4\delta t}(1 + \frac{t}{\delta t})|^{1/2}. \tag{2-34}$$

The Lorentzian peak at $k_0 = \pi$ diverges and changes sign abruptly as δt is changed accross δt_c

$$\lim_{\delta t \to 0^+} F(k_0, \delta t) = -\lim_{\delta t \to 0^-} F(k_0, \delta t) = \pm\infty, \tag{2-35}$$

where 0^+ and 0^- denote the two sides of the phase boundary close to $\delta t_c = 0$. It is also relevant to notice that the width of the Lorentzian $1/\xi$ goes to zero as δt approaches $\delta t_c = 0$ from each side of the phase boundary

$$\lim_{\delta t \to \delta t_c} \xi = \infty. \tag{2-36}$$

Equations 2-35 and 2-36 show that the Lorentzian peak becomes higher and sharper as δt_c is approached, this is shown schematically in Figure 2.3 for the SSH model. Systems described by the linear Dirac model of Equation 2-23 are part of this peak divergence scenario.

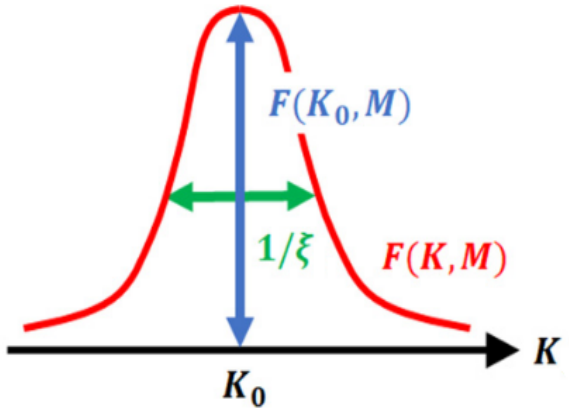

Figure 2.3: Profile of the curvature function $F(k, M = \delta t)$ showing its width $1/\xi$, as we approach the critical point this function becomes sharper, diverges to ∞ and then flips, returning from $-\infty$ [32].

The explicit expressions in Equation 2-34 tell us immediately the critical behavior and exponents

$$|F(k_0, M)| \propto |M - M_c|^{-\gamma}, \quad \xi \propto |M - M_c|^{-\nu}, \tag{2-37}$$

which are in full agreement with the divergences in Equations 2-35 and 2-36, then the conservation of the topological invariant, since we approach the critical point within a fixed phase, leads to a scaling law that constraints the critical exponents

$$\gamma = \nu = 1. \tag{2-38}$$

For this **peak-divergence scenario** which is the case for the SSH model, if we substitute the $F(k, M)$ in Equation 2-31 by the **Ornstein-Zernike (OZ)** form in Equation 2-33 we get a Wannier state correlation function λ_R that decays with R/ξ, this means that ξ plays the role of correlation length. This is because the Fourier transform of a Lorentzian in momentum space gives a

function that decays in real space, with a decay length equal to the inverse of the width of the Lorentzian as shown in Figure 2.3. It is important to highlight that this **correlation lenght** ξ from the OZ approximation is the very same **decay length** of the edge state that was calculated explicitly as shown in Equation 2-21 by means of an ansatz. It is relevant to mention that the topological phase transition that features this divergence of the curvature function and correlation length ξ at the crtical point is said to be of second order and exhibits the same critical behavior as Landau phase transitions but without the existence of an order parameter. In this context, in a similar fashion as in Landau phase transitions, exist a Renormalization Group approach (RG) which is an iterative procedure to find the trajectory (RG flow) in the parameter space along which the divergence is reduced, from there the topological phase transitions can be identified [32]. This consist of a mapping $M \to M'$ that leads to a corresponding generic RG-Equation which rescales the curvature-function from the critical point M_c at which ξ and $F(k, M)$ diverge towards a fixed point M_f at which $\xi = 0$, indicating that the overlap of two Wannier states in Equation 2-31 remains constant at these points regardless how far apart the two Wannier states are. In this work we do not elaborate this method in detail, but rather focus on the critical exponents and correlation length. Nevertheless, the phase diagram obtained in the present work is entirely consistent with that calculated from curvature renormalization group (CRG) approach.

2.2 Interacting SSH model from Green's function formalism

For the noninteracting SSH model presented above as well as for many other noninteracting systems, the edge state can be easily identified and explicitly calculated by solving the low energy Dirac Hamiltonian projected to real space [8–10, 33–35] as we have already shown in detail. Additionally, if the TI or TSC shows linear band-crossing at the topological phase transition, it turns out that the decay length of the edge state results to be proportional to the inverse of the bulk gap $\xi \propto |M|^{-1}$, giving a critical exponent of $\nu = 1$ that we wish to verify if remains the same after introducing interactions. Despite the fact that presently there exists a unified picture which summarizes in a nice manner mostly all noninteracting TIs and TSCs with linear band-crossing, the situation changes a lot when many-body interactions are introduced into the system. The single-particle Bloch state is not anymore a valid quantity to start with in the presence of interactions, so the topology ought to be defined and calculated in a different way. Restricting our investigations to

weakly interacting TIs and TSCs, we could rely on perturbation theory in the interaction-picture to treat these systems, within this context the many-body Green's function serves as a practicable magnitude to identify topology [29, 36–47]. As a function of the dimension and symmetry of the many-body Hamiltonian, the topological invariant $\mathcal{C}$ is expressed as the momentum space integration of a certain combination of the Green's function and its derivative as has been presented for the noninteracting case in Eq. (2-14). The effect of interactions arises in the self-energy that enters the full interacting Green's function [32], this is explicitly shown later when we replace G_0 by G_{int} in Eq. (2-14). We also mentioned previously that a so-called curvature renormalization group approach has already been proposed and used to overcome the complicated integration of the topological invariant, this resulted to be an efficient tool to detect topological phase transitions in parameter spaces of higher dimension [32, 48–51].

In spite of the usefullness and benefits of the Green's function formalism, there are many things related to the weakly interacting TIs and TSCs that require further clarification. First of all, we would like to know if the phenomena of gap-closing is still manifested in interaction-driven topological phase transitions, this because we require a reliable way to recognize the bulk gap under the influence of interactions. Secondly, we need to verify if the bulk-edge correspondence is still satisfied. This is relevant because it clarifies whether the edge state survives interactions, a realistic issue in practice since interactions are usually difficult to neglect completely. To finalize, it is fundamental to clarify whether the edge state decay length exhibits the same critical behavior as its noninteracting counterpart. This responds whether the system remains in the same universality class as the noninteracting case [50, 51].

In the present work, we introduce a formalism based on perturbation theory to make these issues more clear. We limit our study to one-dimensional (1D) TIs with electron-electron interaction, for this we begin with the usage of the spectral function, which is obtained from the many-body Green's function, in order to identify the property of gap-closing near the topological phase transitions. As a second step, we prove the validity of the bulk-edge correspondence in the presence of interactions with the aid of the many-body Green's function in combination with the T-matrix formalism. Within this methodology, the edge is treated as an impurity that breaks the periodicity of the lattice and therefore simulates the open boundary situation. As a consequence, the edge state can be identified from the local density of states (LDOS) in a vicinity of the edge and its decay length permits us to calculate

the respective critical exponent.

Our main objective here is to apply the Green's function method to investigate 2×2 Dirac models under the influence of many-body interactions for the open boundary condition. We already introduced the most general noninteracting 1D spinless 2×2 Dirac Hamiltonian in Equation 2-24. The presence or absence of each $d_i(k)$ together with their evenness and oddness in k are determined by the symmetry class of the corresponding Dirac Hamiltonian. In this research we restricted our analysis to the BDI class, which generally can host both topologically trivial and non-trivial edge states, this is predominantly due to the presence of the chiral symmetry [52–55]. This specific BDI symmetry class relies on time reversal ($\mathcal{T}^2 = +1$), particle-hole ($\mathcal{C} = +1$) and chiral ($\mathcal{S}$) symmetries [11, 13, 51], they impose constrains on the $d_i(k)$ as presented in Equation 2-28. In order to convey the effect of weak electron-electron interaction, together with the open boundary condition addressed by a strong impurity, we start by solving the interaction-dressed Green's function G_{int} from Dyson's equation. Afterwards, we make use of G_{int} in order to calculate the full Green's function G with the aid of the T-matrix approximation which takes into account the effect of the single impurity, therefore simulating effectively the edge of the system.

Sticking to the instructions given above, we start by calculating the effect of the weak interaction Hamiltonian $\mathcal{H}_{int}$ in a perturbatively manner with the aid of the so-called Matsubara Green's function

$$G_{int}(k,\tau) = \begin{pmatrix} G_{intAA}(k,\tau) & G_{intAB}(k,\tau) \\ G_{intBA}(k,\tau) & G_{intBB}(k,\tau) \end{pmatrix} , \tag{2-39}$$

whose matrix elements are defined as

$$G_{intIJ}(k,\tau) = -\langle T_\tau c_{Ik}(\tau) c^\dagger_{Jk}(0)\rangle , \tag{2-40}$$

where T_τ is known as the time ordering operator. The interaction-dressed Green's function with discrete frequency $i\omega_n$ is calculated by solving Dyson's equation

$$\begin{aligned} G_{int} &= G_0 + G_0\Sigma G_{int} = G_0 + G_0\Sigma G_0 + G_0\Sigma G_0\Sigma G_0 + ... \\ &= \left(G_0^{-1} - \Sigma\right)^{-1} = (i\omega_n - H_0 - \Sigma)^{-1} , \end{aligned} \tag{2-41}$$

where Σ stands for the self-energy. The interacting part of Dyson's equation

in Eq. (2-41) is calculated formally as

$$(G_0\Sigma G_{int})_{IJ} = -\sum_{n=1}^{\infty}(-1)^n \int_0^\beta d\tau_1 \int_0^\beta d\tau_2 ... \int_0^\beta d\tau_n$$
$$\times\langle T_\tau c_{Ik}(\tau)\mathcal{H}_{int}(\tau_1)\mathcal{H}_{int}(\tau_2)...\mathcal{H}_{int}(\tau_n)c^\dagger_{Jk}(0)\rangle, \quad (2\text{-}42)$$

corresponding to distinct connected diagrams. In the present study, we limit our calculation to the extend of just one-loop. Additionally, we explore the short range electron-electron interaction between spinless fermions [56–61]. For this particular TI, we contemplate the density-density interaction between two sublattices that takes the specific form

$$\mathcal{H}_{e-e} = \sum_{kk'q} V_q c^\dagger_{Ak+q} c^\dagger_{Bk'-q} c_{Bk'} c_{Ak} \ , \quad (2\text{-}43)$$

where the actual explicit form of $V_{\mathbf{q}}$ is a function which depends on the specific kind of interaction considered to take place in real space. Replacing Eq. (2-43)

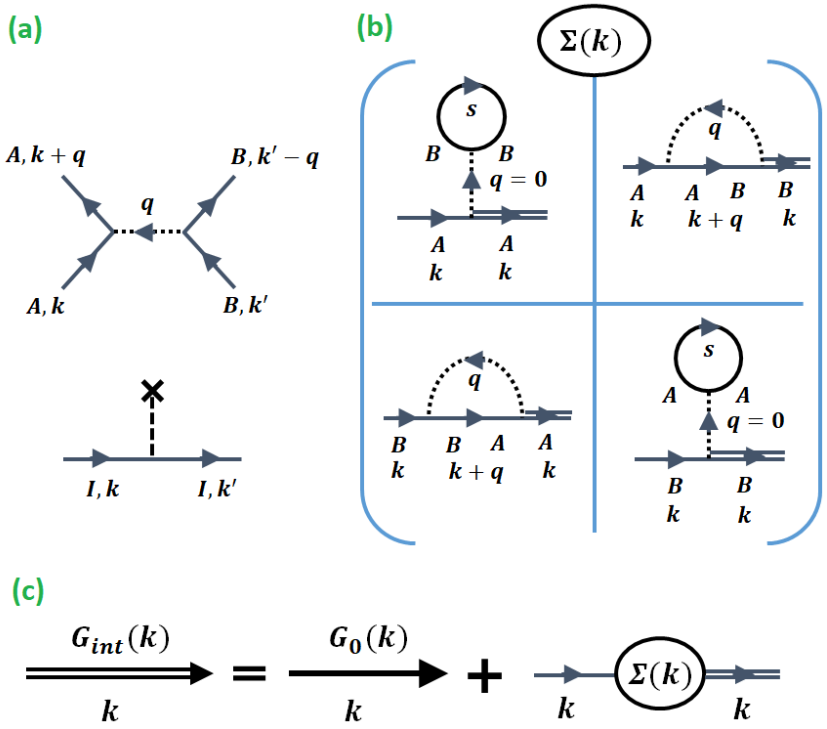

Figure 2.4: Feynman's diagrams representing (a) The vertex of the particular density-density interaction between sublattices A and B investigated here, and the vertex of impurity scattering for the specific sublattice I ($I = A, B$). (b) The self-energy matrix that arises from the specific density-density interaction obtained up to one-loop Hartree-Fock level. (c) The Dyson's equation corresponding to the homogeneous interacting Green's function G_{int}. This Figure has been taken from Ref. [27].

into (2-42), the interacting part of the Dyson's equation up to one-loop level reads as

$$(G_0\Sigma G_{int})_{IJ} = \int_0^\beta d\tau_1 \sum_{pp'q} V_q \\ \times \langle T_\tau c_{Ik}(\tau) c^\dagger_{Ap+q}(\tau_1) c^\dagger_{Bp'-q}(\tau_1) c_{Bp'}(\tau_1) c_{Ap}(\tau_1) c^\dagger_{Jk}(0)\rangle. \tag{2-44}$$

After performing the Fourier tranform of Eq. (2-44), we get the self-energies (whose Feynman diagrams are drawn in Fig. 2.4 (b))

$$\begin{aligned} \Sigma_{AA}(k) &= \sum_p V_{q=0} G_{0BB}(p, \tau = 0) \, , \\ \Sigma_{AB}(k) &= -\sum_q V_q G_{0AB}(k+q, \tau = 0) \, , \\ \Sigma_{BA}(k) &= -\sum_q V_q G_{0BA}(k+q, \tau = 0) \, , \\ \Sigma_{BB}(k) &= \sum_p V_{q=0} G_{0AA}(p, \tau = 0) \, . \end{aligned} \tag{2-45}$$

An interesting feature is that these self-energies result to be frequency-independent $\Sigma_{IJ}(k, i\omega_n) = \Sigma_{IJ}(k)$ for the specific kind of interaction considered. After having solved Dyson's equation we replace the discrete by a continuous frequency $i\omega_n \to i\omega$ to express the Green's function in terms of a continuous frequency ω from which we can find out the LDOS as well as the topological invariant as we detail later. The full Green's function in momentum-frequency space is then expressed explicitly as

$$\begin{aligned} G_{int}(k, i\omega) &= \frac{1}{(i\omega + d'_0)^2 - d'^2} \\ &\quad \times \begin{pmatrix} i\omega + d'_0 + d'_3 & d'_1 - id'_2 \\ d'_1 + id'_2 & i\omega + d'_0 - d'_3 \end{pmatrix} \, , \\ G^{-1}_{int}(k, i\omega) &= \begin{pmatrix} i\omega + d'_0 - d'_3 & -d'_1 + id'_2 \\ -d'_1 - id'_2 & i\omega + d'_0 + d'_3 \end{pmatrix} \, , \end{aligned} \tag{2-46}$$

here $d' = \sqrt{d'^2_1 + d'^2_2 + d'^2_3}$, and the components of the self-energy-renormalized $\mathbf{d}'$-vector $\mathbf{d}' = (d'_1, d'_2, d'_3)$ are written as

$$\begin{aligned} d'_1 &= d_1 + \mathrm{Re}\Sigma_{AB} \, , \quad d'_2 = d_2 - \mathrm{Im}\Sigma_{AB} \, , \\ d'_3 &= d_3 + \frac{\Sigma_{AA} - \Sigma_{BB}}{2} \, , \quad d'_0 = \frac{-\Sigma_{AA} - \Sigma_{BB}}{2} \, . \end{aligned} \tag{2-47}$$

It is relevant to keep in mind that, since the self-energies $\Sigma_{IJ} = \Sigma_{IJ}(k)$ depend

only on k, this is also the case for each $d'_i = d'_i(k)$.

To explicitly calculate the band gap as a function of the external tunning parameters $E_{gap}(\delta t, V)$ we make use of the spectral function $A(k,\omega)$ which is obtained from the retarded version of the Green's function Eq. (2-46) with real frequency $i\omega \to \omega + i\eta$. This spectral function is defined as

$$A(k,\omega) = -\frac{1}{\pi}\mathrm{Im}\left[\mathrm{Tr}G^{ret}_{int}(k,\omega)\right] \ . \tag{2-48}$$

As we argue later, from the spectral function we can identify both the bulk gap and the gap-closing (topological phase transitions) in the presence of interactions, this has been already proved for models in higher dimensions [62].

It is relevant to point out that the interaction term $\mathcal{H}_{e-e}$ in Eq. (2-43) breaks both chiral and particle-hole symmetries, thus modifying the symmetry of the effective Hamiltonian $H(k) = -\sigma_0 d_0{}' + \boldsymbol{\sigma}\cdot\mathbf{d}'$. To be more specific, for the special case of density-density interaction in which the self-energy is frequency-independent, we find $d'_3 = 0$ and a finite (induced) d'_0. Despite the fact that the usual definition of $\mathcal{S}$ and $\mathcal{C}$ [11] requires Eq.2-28 – which is not compatible with having a finite d'_0 – Ref. [13] realized that it is possible to generalize those symmetries with respect to a shift. With this particular generalization a model that respects both particle-hole and chiral symmetries fulfills

$$\begin{aligned}&\mathcal{S}\left[H(k) - \frac{1}{2}TrH(k)\right]\mathcal{S}^{-1} = -\left[H(k) - \frac{1}{2}TrH(k)\right] \\ &= \mathcal{C}\left[H(-k) - \frac{1}{2}TrH(-k)\right]\mathcal{C}^{-1}.\end{aligned} \tag{2-49}$$

As a consequence, the whole spectrum is shifted by $TrH(k)/2 = -d'_0$ and therefore the band structure can be thought to be particle-hole and chiral symmetric with respect to $-d'_0$ (a kind of induced chemical potential). The noninteracting parametrization in Eq. 2-28 represents then a less general situation taking place when $TrH(k) = 0$.

2.3 Corroborating bulk-edge correspondence by T-matrix formalism

Now we are ready to study the edge state of the system subjected to the influence of interactions. Due to the presence of interactions, it is no longer feasible to identify the edge state from the single particle wave function, which is now undefined. In this situation the proper quantity to be investigated is the impurity Green's function, this issue has already been verified for the

less general case of noninteracting systems [63]. Our aim is to prove that the LDOS obtained from the real space impurity Green's function, in conjunction with the topological invariant calculation, could be used to verify the bulk-edge correspondence and to investigate the quantum critical behavior for interacting 1D TIs.

As we pointed out previously, we can account for the presence of edge states through the T-matrix formalism which permits to take into consideration the existence of an impurity that effectively creates or simulates an edge. In this investigation we consider a sharp δ-function to model the edge of the system (strong impurity) which is assumed to be located at a given $r = 0$ position of the lattice

$$U(r) = U_0\delta(r) \ , \tag{2-50}$$

for a 1D TI defined in the semi-infinite space $r > 0$. Considering the most general potential scattering, with strength denoted by $U_{kk'}$ in momentum space, this potential breaks the translational invariance of the system. As a consequence, the full Green's function starts depending on two indices k and k' and reads, in momentum space, as

$$G(k,k',\tau) = \begin{pmatrix} G_{AA}(k,k',\tau) & G_{AB}(k,k',\tau) \\ G_{BA}(k,k',\tau) & G_{BB}(k,k',\tau) \end{pmatrix} \ , \tag{2-51}$$

whose matrix elements are defined as

$$G_{IJ}(k,k',\tau) = -\langle T_\tau c_{Ik}(\tau)c^\dagger_{Jk'}(0)\rangle \ . \tag{2-52}$$

For the interacting case, the impurity (also called "edge" or "full") Green's function, simply denoted as G, is obtained from incorporation of the G_{int} in Eq. (2-46) into the T-matrix approximation [64]

$$\begin{aligned} G(k,k') &= G_{int}(k)\delta_{kk'} + G_{int}(k)U_{kk'}G_{int}(k') + ... \\ &= G_{int}(k)\delta_{kk'} + G_{int}(k)T_{kk'}G_{int}(k') \ , \\ &= G_{int}(k)\delta_{kk'} + G_{int-T}(k,k') \ , \end{aligned} \tag{2-53}$$

where $G_{int}(k)$ and $G_{int-T}(k,k')$ stand for, respectively, the homogeneous (no impurity) and inhomogeneous (with impurity) components. The T-matrix

fulfills

$$T_{kk'} = U_{kk'} + \sum_{k''} U_{kk''} G_{int}(k'') T_{k''k'} \ , \tag{2-54}$$

as is presented diagramatically in Fig. 2.5. For the δ-function potential we used in Eq. (2-50) to effectively create the edge, we have $U_{kk'} = U_0$, and therefore

$$T = T(i\omega_n) = U_0 \left[I - U_0 \sum_k G_{int}(k, i\omega_n) \right]^{-1} \ . \tag{2-55}$$

This result tell us that the T-matrix depends only on the (Matsubara or complex) frequency. If we focus on the particular case of a infinitely strong impurity, situation known as the hard edge limit $U_0 \to \infty$, then the T-matrix reduces to

$$\lim_{U_0 \to \infty} T(i\omega_n) = - \left[\sum_k G_{int}(k, i\omega_n) \right]^{-1} \ , \tag{2-56}$$

which displays a quite manageable form. In this research project, we will concentrate on this hard edge limit $U_0 \to \infty$ which seems appropiate to generate the edge state. Within this approximation the T-matrix and local density of states become explicitly independent on the parameter U_0. The T-matrix with real frequencies, that is needed to obtain the full retarded Green's function, is judged similarly. This methodology considers only the essential diagrams that permit to capture the edge state, i.e., the diagrams that generate the impurity bound state. Notwithstanding that, our method fails to take into account diverse impurity-interaction interference diagrams as those drawn in Fig. 2.5 (c), which ought to be treated elsewhere.

Once we have solved for the full retarded Green's function, which corresponds to perform an analytical continuation $i\omega_n \to \omega + i\eta$ for all quantities which are dependend on the Matsubara frequency, we are ready to get the actual LDOS. We begin by going from momentum space towards real space, for this we take the Fourier transform of the already calculated momentum space full Green's function

$$G^{ret}_{IJ}(r, r', \omega) = \int \frac{dk}{2\pi} \int \frac{dk'}{2\pi} e^{i(kr - k'r')} G^{ret}_{IJ}(k, k', \omega) \ . \tag{2-57}$$

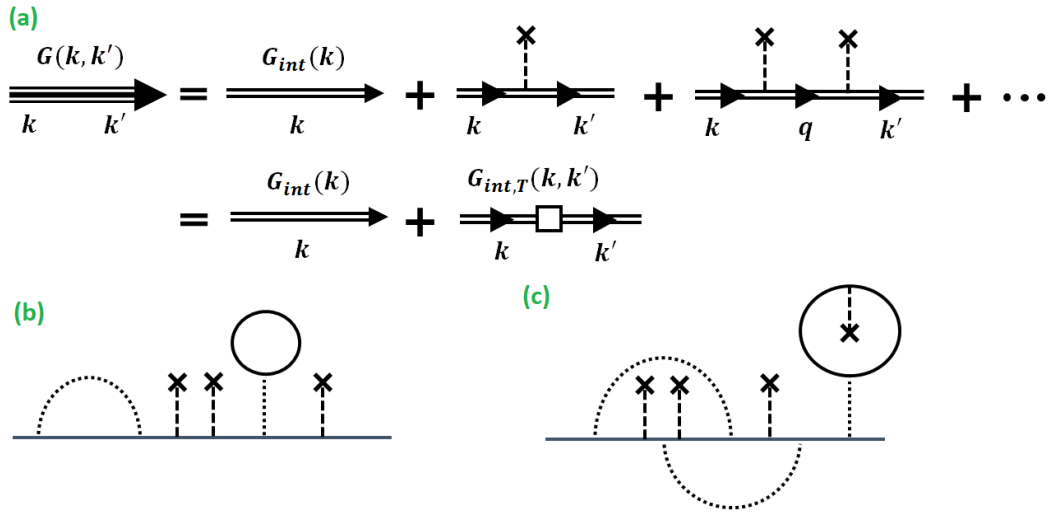

Figure 2.5: (a) Feynman's diagram representing the full impurity Green's function obtained from the incorporation of the homogeneous interacting Green's function into the T-matrix approximation. (b) Some specific diagrams that are (b) considered and (c) not considered within our approximation. This Figure has been taken from Ref. [27].

The LDOS in real space reads

$$\begin{aligned}\rho(r,\omega) &= -\mathrm{Im}\left\{\mathrm{Tr}\left[G^{ret}(r,r,\omega)\right]\right\}/\pi \\ &= -\mathrm{Im}\left\{G^{ret}_{AA}(r,r,\omega)+G^{ret}_{BB}(r,r,\omega)\right\}/\pi\ ,\end{aligned} \tag{2-58}$$

which is made up from the summation of the imaginary parts of the retarded Greens function of the A and B sublattices. Here it is relevant to mention that the so-called spectral sum rule of this T-matrix-Dyson's equation formalism is fulfilled as follows. If we split the homogeneous and the impurity parts of the Green's function as shown in Eq. (2-53), and label their corresponding LDOS as

$$\begin{aligned}&\rho_{int}(r,\omega) = -\mathrm{Im}\left\{\mathrm{Tr}\left[G^{ret}_{int}(r,r,\omega)\right]\right\}/\pi\ , \\ &\rho_{int-T}(r,\omega) = -\mathrm{Im}\left\{\mathrm{Tr}\left[G^{ret}_{int-T}(r,r,\omega)\right]\right\}/\pi\ , \\ &\rho(r,\omega) = \rho_{int}(r,\omega)+\rho_{int-T}(r,\omega)\ ,\end{aligned} \tag{2-59}$$

therefore

$$\begin{aligned}&\int_{-\infty}^{\infty} d\omega\,\rho(r,\omega) = \int_{-\infty}^{\infty} d\omega\,\rho_{int}(r,\omega) = 2\ , \\ &\int_{-\infty}^{\infty} d\omega\,\rho_{int-T}(r,\omega) = 0\ .\end{aligned} \tag{2-60}$$

So we verify that the particle number is conserved and comes only from the homogeneous part, the integration gives 2 since we counted the contribution from the 2 bands of the system (the VB and the CB). The edge state arises from the impurity-scattering part $\rho_{int-T}(r,\omega)$, this part only changes the profile of the total LDOS $\rho(r,\omega)$ without modifying the total number of particles, a feature we already expect from the relation $[H, H_{e-e}] = 0$.

To calculate effectively the decay length of the edge state and to avoid the tedious fit of the decaying LDOS in real space, we rely on the following approach. In a vicinity of the critical point $M \to M_c$, the impurity Green's function in momentum space $G^{ret}(k,k',\omega)$ is even in k and k' and is well fitted by an Ornstein-Zernike form near the high symmetry points $\{k_0, k_0'\} = \{\pi, \pi\}$, i.e.,

$$G^{ret}(k_0+\delta k, k_0'+\delta k', \omega) \approx \frac{G^{ret}(k_0, k_0', \omega)}{(1+\xi^2\delta k^2)(1+\xi^2\delta k'^2)}. \tag{2-61}$$

As a result, after taking the Fourier transform in Eq. (2-57), we get a LDOS decaying with a decay length ξ. So it is only necessary to extract ξ from the Ornstein-Zernike fit in Eq. (2-61), a much easier task than explicitly taking the Fourier transform in Eq. (2-57) and then making a fit to get ξ in real space.

2.3.1 Topological invariant and edge states of interacting Su-Schrieffer-Heeger model

We are now ready to make use of the general formalism introduced previously and apply it to the specific case of the SSH system introduced in Sec. 2.1, but taking into account the presence of nearest-neighbor electron-electron interaction. Many different versions of the SSH model have been already investigated with the aid of different techniques [65–69]. In the noninteracting limit, the topological properties of the system have been investigated experimentally with the aid of optical lattices [70, 71]. In this work, we concentrated on the quantum criticality investigated by means of the Green's function approach. The noninteracting part of the Hamiltonian, described by Eq. (2-5), which stands for the SSH model alone, can be cast into the following form:

$$\begin{aligned} \mathcal{H}_0 &= \sum_i (t+\delta t) c_{Ai}^\dagger c_{Bi} + (t-\delta t) c_{Ai+1}^\dagger c_{Bi} + h.c. \\ &= \sum_k Q_k c_{Ak}^\dagger c_{Bk} + Q_k^* c_{Bk}^\dagger c_{Ak} \ , \end{aligned} \tag{2-62}$$

here $t+\delta t$ and $t-\delta t$ represent the hopping amplitudes on the even and the odd bonds, and $Q_k = (t+\delta t) + (t-\delta t)e^{-ik}$ stands for the out of diagonal matrix element of the Dirac Hamiltonian. The bare chemical potential of this system is set to be zero by definition. We choose the interaction to be a density-density specific kind of interaction between nearest-neighbors only as is the situation chosen in Ref. [32]

$$\mathcal{H}_{e-e} = V \sum_i \left(n_{Ai} n_{Bi} + n_{Bi} n_{Ai+1} \right) \ , \tag{2-63}$$

where $n_{Ii} \equiv c_{Ii}^\dagger c_{Ii}$. Taking the Fourier transform of this interaction Hamiltonian gives us Eq. (2-43) with $V_q = V(1+\cos q)$ [32]. We see immediately that this specific form of interaction breaks both particle-hole and chiral symmetries with respect to zero frequency (the $\mathcal{C}$ and $\mathcal{S}$ symmetries are still respected if we replace $n_{Ii} \to (n_{Ii} - 1/2)$ everywhere in Eq. (2-63)). Restricting our study to just one-loop approximation, we find the following self-energies [32]

$$\Sigma_{AA}(k) = \Sigma_{BB}(k) = V \ , \tag{2-64}$$

$$\Sigma_{AB}(k) = \frac{1}{2} \sum_q V_q e^{-i\alpha_{k+q}} = \left[\Sigma_{BA}(k) \right]^* \ , \tag{2-65}$$

where the phase factor α_k arises from $Q_k \equiv |Q_k| e^{-i\alpha_k}$. The Σ_{AA} and Σ_{BB} stand for the Hartree terms that bring in a finite induced chemical potential $d_0' = -V$ that shifts the entire spectrum by V without broadening it (because it is a purely real quantity). Considering Eq. (2-49), for this specific situation it is then clear that

$$\mathcal{S} \left[H(k) + V \right] \mathcal{S}^{-1} = - \left[H(k) + V \right] , \tag{2-66}$$

$$\mathcal{C} \left[H(-k) + V \right] \mathcal{C}^{-1} = - \left[H(k) + V \right] , \tag{2-67}$$

which represents a generalization of the symmetries with respect to the finite induced chemical potential and provides a spectrum that is symmetric with respect to V. To finalize, with the aid of Eqs. (2-64) and (2-65), the Green's function Eq. (2-46) can be explicitly written as

$$G(k, i\omega) = \frac{1}{(i\omega - V)^2 - |Q_k + \Sigma_{AB}(k)|^2} \times \begin{pmatrix} i\omega - V & Q_k + \Sigma_{AB}(k) \\ \left[Q_k + \Sigma_{AB}(k) \right]^* & i\omega - V \end{pmatrix} . \tag{2-68}$$

We already highlighted in the previous Section that at $i\omega = V$ the full Green's function turns out to be off-diagonal. Due to the presence of interactions, the topological invariant is modified and corresponds to a winding number of the new phase [29, 32, 68, 72]

$$\begin{aligned}\varphi_k &= -\arg\left(Q_k + \Sigma_{AB}\right), \\ &= -\arg\left(Q_k + \frac{1}{2}\sum_q V_q e^{-i\alpha_{k+q}}\right) . \end{aligned} \tag{2-69}$$

To make clear why this is the case for the interacting model, let us remind the way the topological invariant is calculated in terms of the full Green's function [29]

$$\mathcal{C} = \int_0^{2\pi} \frac{dk}{4\pi i} Tr(\sigma_3 G^{-1}\partial_k G)|_{i\omega=-d_0'} \tag{2-70}$$

where the integrand is evaluated at $i\omega = -d_0'$, where d_0' can be viewed as the interaction-induced chemical potential. In the case under study in which the self-energy is frequency-independent, the requirement of $i\omega = -d_0'$ physically means that the entire spectrum is shifted by $-d_0'$ and hence the spectrum is particle-hole symmetric with respect to $-d_0'$ as we already stressed out. As a consequence, within this Green's function formalism, the reference energy should be shifted to $i\omega = -d_0'$ such that the diagonal element of the Green's function is set to zero and we can apply Eq. (2-70). Observe that in the noninteracting model delineated by Eq. (2-28) the $d_0 = 0$ and hence $i\omega = 0$ in Eq. (2-70) [29], [43]. Looking at Eq. (2-41), one realizes that the full Green's function at $i\omega = -d_0'$ has the same feature as the unperturbed Green's function, namely it possess only off-diagonal elements

$$G(k, i\omega = -d_0') = \begin{pmatrix} 0 & \frac{-Q_k - \Sigma_{AB}}{|Q_k + \Sigma_{AB}|^2} \\ \frac{-Q_k^* - \Sigma_{AB}^*}{|Q_k + \Sigma_{AB}|^2} & 0 \end{pmatrix} , \tag{2-71}$$

where $\Sigma_{AB} \equiv \Sigma_{AB}(k, i\omega = -d_0') = \Sigma_{BA}(k, i\omega = -d_0')^*$ stands for the upper-right off-diagonal element of the 2×2 self-energy matrix at $i\omega = -d_0'$. Introducing Eq. (2-71) into Eq. (2-70), the topological invariant is

$$\begin{aligned}\mathcal{C} &= \frac{1}{4\pi i}\int_0^{2\pi} dk[\frac{-1}{Q_k + \Sigma_{AB}}\partial_k(Q_k + \Sigma_{AB}) - H.c.] \\ &= \frac{1}{2\pi}\int_0^{2\pi} dk \partial_k \varphi_k , \end{aligned} \tag{2-72}$$

where φ_k is the argument of $Q_k + \Sigma_{AB} = |Q_k + \Sigma_{AB}|e^{-i\varphi_k}$. So we have demonstrated that the topology of the system simply counts the number of times that the phase of $Q_k + \Sigma_{AB}$ winds as k goes from 0 to 2π. This winding number is dictated by the off-diagonal elements of both the noninteracting Hamiltonian $Q_k = d_1 - id_2$ and the self-energy Σ_{AB}. From this particular form of the phase we can notice how the interaction alters the phase by means of the self-energy, and so the topological invariant is affected by the interaction. This fact permits us to state that interactions are capable of driving topological phase transitions.

This topological phase transition can be identified, in the $\delta t - V$ parameter space, from the gap-closing which is derived from the spectral function (read our argument below). The phase transition line obtained in this way turns out to coincide exactly with the one solved by means of the CRG approach as in Ref. [32], this result is presented in Fig. 2.6 (a). For either $V > 0$ or $V < 0$ regimes, the calculated phase diagram displays both topologically trivial $\mathcal{C} = 0$ and nontrivial $\mathcal{C} = 1$ phases. It is noteworthy the fact that for $V < 0$ the topological phase transition has been displaced from $\delta t = 0$ to a negative δt, whereas for $V > 0$ it is shifted to a positive δt. So it is clear that the critical point in the parameter space is shifted due to the presence of the interactions.

This spectral function $A(k, \omega)$, which has been defined in Eq. (2-48), experiences a shift in frequency due to particle-hole-breaking nature of the interaction. This result is clearly noticeable by looking at Fig. 2.6 (b)$\sim$(d). This displacement of the whole energy spectrum originates from the Hartree term $\Sigma_{AA}(k) = \Sigma_{BB}(k) = V$ in Eq. (2-64). Additionally, due to the real nature of the Hartree term, the quasiparticle lifetime is not affected, i.e., there is no broadening of the spectral function for this specific electron-electron interaction (for more general kinds of interactions this is not the case). In spite of this shift in frequency for finite V, the band gap, which is identified from the separation between the two peaks $A(\pi, \omega)$ at the high symmetry point $k = \pi$, is clearly noticeable in Fig. 2.6 (b)$\sim$(d). As V is varied across the critical point V_c, the spectral function clearly shows a gap-closing at the high symmetry point. If the topological phase transitions is driven by the kinetic parameter δt, the same phenomena takes place. We can therefore state that this behavior of the spectral function proves unambiguously that gap-closing is a definite property occurring at topological phase transitions even for systems subjected to interactions.

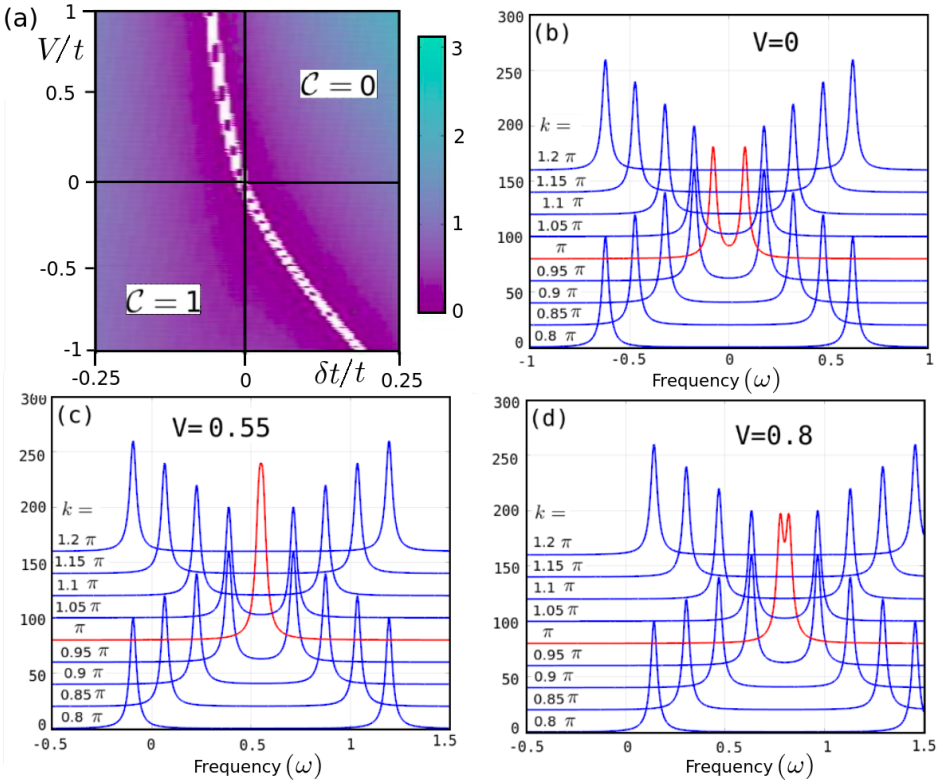

Figure 2.6: (a) Phase diagram for the SSH system with nearest-neighbor density-density interaction. The color scale tells us the magnitude of the gap which is calculated from the spectral function $A(k,\omega)$, and the white line represents the phase transition line at which this gap closes. (b) to (d) highlight the dependence of $A(k,\omega)$ on ω as k varies from $k=0.8\pi$ to 1.2π at a fixed $\delta t=-0.04$ for some values of V. The closing of the gap at the critical point $V_c=0.55$ is clear. The whole spectrum is displaced with V since the interaction in Eq. (2-63) destroys particle-hole symmetry. This Figure has been taken from Ref. [27].

For this interacting SSH model, its LDOS is presented in Fig. 2.7, this was computed considering 128×128 grid points for the integration in momentum space of Eq. (2-57) and an artificial broadening of $\eta=0.05$ in the analytical continuation $i\omega_n\rightarrow\omega+i\eta$ to get the retarded Green's function. The edge state can be recognized as the peak located in the middle of the spectrum and it only appears in the topologically nontrivial phase, showing that the bulk-edge correspondence is properly satisfied in this model. Since the whole energy spectrum is displaced by the interaction V and the edge state is always located in the in the middle of the gap, this edge state is moved away from absolute zero frequency by the interaction. Considered as a function of the separation distance from the edge located at $r=0$, we unveil that this edge state remains localized in one sublattice only, this is a property inherited from the noninteracting limit which was previously obtained by analytical solution of

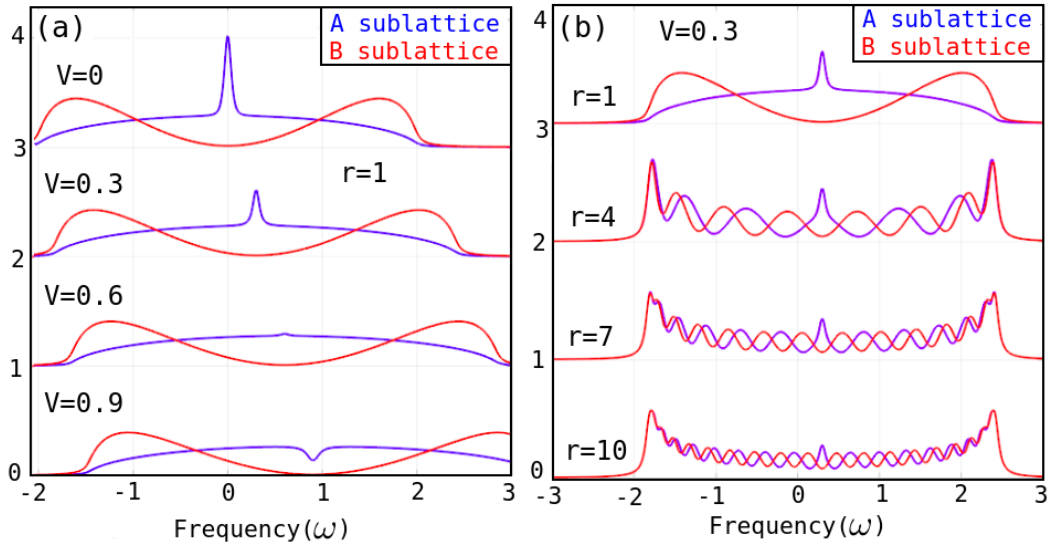

Figure 2.7: (a) LDOS for the two sublattices of the SSH model with fixed $\delta t = -0.04$ at the first lattice site located at $r = 1$ away from the edge, and for some values of the interaction strength V. We clearly notice that the edge state situated in the middle of the spectrum appears only within the topologically nontrivial region $V < 0.6$, and is located at the A sublattice only. (b) LDOS for $V = 0.3$ at some specific spots r localized away from the edge, this shows an edge state which decays as r increases. The wavy features noticeable in the spectrum arise from finite size effects. This Figure has been taken from Ref. [27].

the Dirac equation projected into real space. The decaying behavior of the peak signaling the edge state, as we move away from the edge (so as we increase r), is clearly noticeable. For this system the decay length $\xi \sim \mathrm{M}^{-1}$ shows a critical exponent $\nu = 1$ regardless of the tunning parameter that is varied continuously to drive the phase transition, it holds for both $M = \delta t$ and $M = V$ as is nicely presented in Fig. 2.8(this critical exponent is calculated with the aid of the fit in Eq. (2-61), up to the accuracy of grid size $\xi^{-1} \approx \Delta k \approx 0.05$ set in momentum space). This tells us that the SSH model, even under the presence of the nearest-neighbor interaction defined by Eq. (2-63), stays within the same universality class.

To finalize this Chapter, we reflect on the plausibility of our statement, since our procedure is limited to just one-loop calculation of the self-energy. We could expect that as we increase V, higher-loop corrections to the self-energy would become more and more relevant, and the one-loop result will start losing accuracy. Consequently, our expectation is that the phase transition line depicted in Fig. 2.6(a), as well as the size of the bulk gap calculated from the spectral function $A(k, \omega)$, could change at larger V. Despite this, we believe

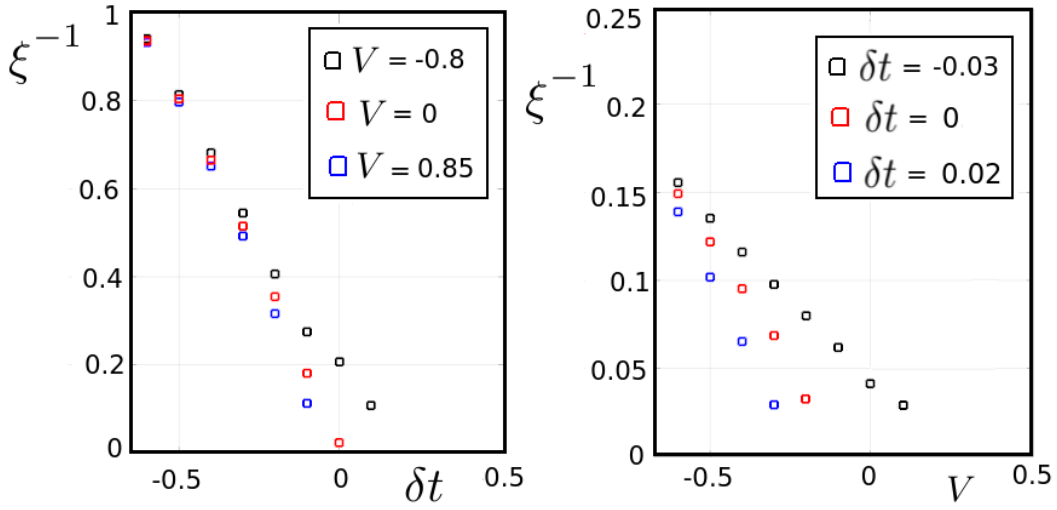

Figure 2.8: We can perform a fit to extract the critical exponent of the decay or correlation length of the edge state $\xi \sim |M|^{-\nu}$ for (a) $M = \delta t$ at different values of V, and (b) $M = V$ at different values of δt. We clearly notice a linear behavior which provides a critical exponent of $\nu = 1$. This Figure has been taken from Ref. [27].

our statements related to critical exponents $\nu = 1$ and universality class ought to survive further corrections. This conclusion is reinforced from the results obtained in Ref. [73], where a Chern insulator in strong coupling far beyond the reach of perturbation theory is shown to remain within the same universality class as the noninteracting model, this was further confirmed by means of an exact diagonalization approach. Even though the strong coupling limit $V > t$ of our model is beyond the scope of our methodology, considering our result together with the one of Ref. [73] suggests that whether considering only the lowest order self-energy in the small V regime or using an exact diagonalization (or Machine Learning method or any other efficient computational method) to study the larger V limit, the system will still remain within the same universality class.

3
Persistent currents and spin torque caused by percolated quantum spin Hall state

In this Chapter we perform a similar review for our second project, which in turn materialized into our second paper entitled **Persistent currents and spin torque caused by percolated quantum spin Hall state** [74], and here in a similar way we will follow very closely what we have written in our article. We start, in Section 3.1, with the introduction of some relevant concepts and motivation about the importance of the QSHE and its practical applications to the field of spintronics. Then, in Section 3.2, we perform a review of the time reversal symmetry and operator for spinful particles because it is key to properly define and calculate the topological invariant for the system under study. Here we also derive Kramers theorem, which has important consequences in the topological properties of the system of interest. Section 3.3 is devoted entirely to the investigation of the physical properties of a system which results from putting in contact a 2D TI known as the Bernevig-Hughes-Zhang (BHZ) model and a Ferromagnetic-Metal (FMM), we refer to this system as the 2D TI/FMM junction. We start Section 3.3.1 by elucidating the continuous BHZ model and indicate the way its edge-states are calculated, later we focus on the lattice model for the 2D TI/FMM junction. From this model we outline two different kinds of band structure and address the corresponding percolation or infiltration of topological edge states from the BHZ into the FMM in Section 3.3.2. In Section 3.3.3 we move forward to prove that the asymmetric type of band structure is the source of a laminar flow of local persistent charge current, we also elaborate the proximity induced local persistent spin current flowing near the junction that connects the two subsystems. Later in Section 3.3.4 we investigate the current-induced spin torque with the aid of linear response theory, there we point out the field-like nature of the spin torque which is a direct consequence of the real nature of the wave functions representing the percolated edge state as well as the quantum well state of the FMM.

3.1 Introduction and Motivation

One of the predominant properties of two-dimensional (2D) time-reversal (TR) invariant topological insulators (TIs) is represented by a celebrated phenomenom known as the quantum spin Hall effect (QSHE) [3–6, 8]. Several spintronic devices based upon topological edge states have been motivated from the defining feature of QSHE, namely the existence of a spin current which flows at the edge of the system, this is supposed to be a direct consequence of the existence of spin polarized topological edge states. However, we show in this work that even though the TI by itself do possess spin polarized topological edge states, this TI alone does not exhibit any local spin current unless we put it in contact with a FMM. So, in order to take advantage of the edge states and generate a local spin (and charge) current, the TI is put in contact with the FMM, this has been performed for specific three-dimensional (3D) TI/FMM heterostructures [15, 20, 75–77] with the purpose of using the magnetization of the FMM to manipulate the edge spin transport and viceversa. From a theoretical perspective, a lot of research has been carried out to explore the complex spintronic phenomena occuring in such a hybrid structure [21–26]. To properly address an accurate theoretical description for this system, it is important to understand the way in which the QSH state is altered when the TI is put in contact with a metal. This because the boundary condition for the edge state wave function changes in this situation.

The practicability of spin to charge interconversion has been verified in recent experiments performed on spintronic devices based on 2D TIs. The high efficiency of spin-transfer torque and spin pumping that has been measured on monolayer and multilayer transition metal dichalcogenide/ferromagnet (TMD/FMM) heterostructures is very promising [78–83]. This is a particular advantage provided by these materials that manisfests the QSHE [84–86]. Making use of a lattice model and, stimulated by these experimental results, we investigate the 2D TI/FMM planar junction in order to make clear the role that the edge states have in these spintronic effects. We find out that the way in which the QSH state is modified depends mainly on two issues, the first is related to the location of the Dirac cone with respect to the FMM subbands, i.e., whether the type of band structure is of the pristine or submerged kind (we later provide details on this dicotomy), and the second is the direction set for the magnetization of the FMM. Both the percolation of the edge state into the FMM, as well as the spin-momentum locking in the TI region close to the TI/FMM interface, are firmly influenced by these two factors. We unveil some

interesting dissipationless responses which include the generation of laminar flows of room temperature persistent charge and spin currents that change in direction and magnitude as we move away from the interface. Furthermore, we detail how crucial the real wave function of the percolated edge state is for determining both the magnitude and direction of the current-induced spin torque.

3.2 Time reversal symmetry for spinful particles and $\mathbb{Z}_2$ invariant from sign of the Pfaffian

Before moving forward, it is relevant to review the time-reversal (TR) symmetry and the operator representing it because this is the essential ingredient to QSHE and is responsible for bringing topological protection to the edge states of the TI. We start with a brief discussion of the TR symmetry and outline the way to obtain the topological invariant for this system which belongs to a particular symmetry class (AII in 2D). This specific symmetry class imposes important consequences on the topological properties of the systems belonging to it, this holds for both spinless and spinful particles. The corresponding time-reversal operator T is constructed out of an unitary operator U ($U^\dagger U = UU^\dagger = I$) and the complex conjugate operator K. Due to the fact that spin is an angular momentum, it is rotated by the action of this operator, conventionally we define this rotation to be along the $y-$axis

$$T = UK = e^{-i\pi S_y}K, \quad T\mathbf{S}T^{-1} = -\mathbf{S}. \tag{3-1}$$

Squaring T yields

$$T^2 = e^{-i\pi S_y}Ke^{-i\pi S_y}K = e^{-i\pi S_y}e^{i\pi S_y^*} = e^{-2\pi S_y} = \pm 1, \tag{3-2}$$

this brings us the important result that for integer spin (bosons) $T^2 = 1$ and for half-integer spin (fermions) $T^2 = -1$. We are interested particularly in the study of topological insulators composed by spin 1/2 electrons, so the spin rotation part of the T operator is written as

$$T = e^{-i\pi\sigma_y/2}K = -i\sigma_y K \rightarrow T^2 = -i\sigma_y K(-i\sigma_y)K = \sigma_y\sigma_y^* = -1. \tag{3-3}$$

Since $T^2 = -1$, this implies that $T^{-1} = -T$ and the operation on the spin is therefore

$$T\mathbf{S}T^{-1} = -i\sigma_y K\mathbf{S}i\sigma_y K = -i\sigma_y\mathbf{S}^*Ki\sigma_y K = \sigma_y\mathbf{S}^*\sigma_y. \tag{3-4}$$

Using the explicit expression $\mathbf{S} = \boldsymbol{\sigma}/2$ (so $S^{x*} = S^x, S^{z*} = S^z$, but $S^{y*} = -S^y$), together with the fact that $\{\sigma_a, \sigma_b\} = 2\delta_{ab}$, we then obtain that $\sigma_y\mathbf{S}^*\sigma_y = -\mathbf{S}$.

We proceed now to prove the so-called Kramers theorem for half-integer spin systems. Since for this case $T^2 = -1$ and $T = UK$ we then have $U = -U^T$. If the system has time-reversal symmetry $[H, T] = 0$, this implies that eigenstates $|\psi\rangle$ and $T|\psi\rangle$ have the same eigenenergy E and their overlap is

$$\langle\psi|T|\psi\rangle = \sum_{mn}\langle\psi|m\rangle\langle m|T|n\rangle\langle n|\psi\rangle = \sum_{mn}\psi_m^* U_{mn} K\psi_n = \sum_{mn}\psi_m^* U_{mn}\psi_n^*$$

$$= \sum_{mn}\psi_m^*(-U_{nm})\psi_n^* = -\langle\psi|T|\psi\rangle = 0, \tag{3-5}$$

meaning that $|\psi\rangle$ and $T|\psi\rangle$ are orthogonal and hence degenerate. We arrive at the **Kramers theorem**, which states that for half-integer spin systems that are subjected to time-reversal symmetry, the energy spectrum is at least doubly degenerate.

In a similar fashion we can verify, using $T^{-1} = -T, U = -U^T$ and $U^\dagger U = I$ that the matrix element coupling $|\psi\rangle$ and $T|\psi\rangle$ in a Hamiltonian that obeys TR symmetry $THT^{-1} = H$ vanishes

$$\langle\psi|HT|\psi\rangle = 0, \tag{3-6}$$

meaning that if a half-integer spin system follows time-reversal symmetry, then there is no matrix element coupling $|\psi\rangle$ and $T|\psi\rangle$. At the operator level, we are not allowed to directly apply $T^2 = -1$ since this depends on the even or odd number of spin 1/2 fermions occupying the state. From the fact that this operation flips the spin, the following relations are valid

$$Tc_{i\uparrow}T^{-1} = Ac_{i\downarrow}, \quad Tc_{i\downarrow}T^{-1} = Bc_{i\uparrow} \rightarrow Tc_{i\uparrow}c_{i\uparrow}^\dagger|0\rangle = -AB|0\rangle^* \tag{3-7}$$

and hence $AB = -1$, observe that the T^2 acts on the single spin 1/2 state so we can use $T^2 = -1$, and $|\psi\rangle^* = \sum_m |m\rangle\langle m|\psi\rangle^* = \sum_m |m\rangle\psi_m^*$, the convention is to select $A = 1$ and $B = -1$ so we may write in a compact manner for both the real and momentum spaces (after a Fourier transform)

$$Tc_{i\sigma}T^{-1} = i\sigma^y_{\sigma\sigma'}c_{i\sigma'}, \quad Tc_{i\sigma}^\dagger T^{-1} = c_{i\sigma'}^\dagger(-i)\sigma^y_{\sigma'\sigma} = c_{i\sigma'}^\dagger i(\sigma^y)^T_{\sigma'\sigma} \tag{3-8}$$

$$Tc_{\mathbf{k}\sigma}T^{-1} = i\sigma^y_{\sigma\sigma'}c_{-\mathbf{k}\sigma'}, \quad Tc_{\mathbf{k}\sigma}^\dagger T^{-1} = c_{-\mathbf{k}\sigma'}^\dagger i(\sigma^y)^T_{\sigma'\sigma}. \tag{3-9}$$

If a Hamiltonian fulfills TR symmetry, then

$$H = THT^{-1} = \sum_{\mathbf{k}} Tc^{\dagger}_{\mathbf{k}\sigma} h_{\sigma\sigma'}(\mathbf{k}) c_{\mathbf{k}\sigma'} T^{-1} = \sum_{\mathbf{k}} c^{\dagger}_{-\mathbf{k}\sigma''} i(\sigma^y)^T_{\sigma''\sigma} T h_{\sigma\sigma'}(\mathbf{k}) T^{-1} i\sigma^y_{\sigma'\sigma'''} c_{-\mathbf{k}\sigma'''}$$

$$= \sum_{\mathbf{k}} c^{\dagger}_{\mathbf{k}\sigma''} i(\sigma^y)^T_{\sigma''\sigma} T h_{\sigma\sigma'}(-\mathbf{k}) T^{-1} i\sigma^y_{\sigma'\sigma'''} c_{\mathbf{k}\sigma'''} = \sum_{\mathbf{k}} c^{\dagger}_{\mathbf{k}\sigma''} h_{\sigma''\sigma'''}(\mathbf{k}) c_{\mathbf{k}\sigma'''} \quad (3\text{-}10)$$

Then we use the fact that $h_{\sigma\sigma'}(-\mathbf{k})$ is just a number (matrix element) defined at a specific $\{\mathbf{k}, \sigma, \sigma'\}$, so the effect of time-reversal operator is to take its complex conjugate $Th_{\sigma\sigma'}(-\mathbf{k})T^{-1} = h_{\sigma\sigma'}(-\mathbf{k})^*$, and hence the above equation implies that $h_{\sigma''\sigma'''} = i(\sigma^y)^T_{\sigma''\sigma'} h^*_{\sigma\sigma'}(-\mathbf{k}) i(\sigma^y)_{\sigma'\sigma'''}$. Applying TR operation one more time and using $T = i\sigma^y K$ and $T^{-1} = K(-i\sigma^y) = -i\sigma^y K$ and dropping all the spin indices for simplicity, we get

$$Th(\mathbf{k})T^{-1} = i\sigma^y K(-i\sigma^y) h^*(-\mathbf{k}) i\sigma^y (-i\sigma^y) K$$

$$= -(i\sigma^y)^2 K h^*(-\mathbf{k})(-1)(i\sigma^y)^2 K = h(-\mathbf{k}) KK = h(-\mathbf{k}) \quad (3\text{-}11)$$

which means that the single particle hamiltonian changes its argument $\mathbf{k} \to -\mathbf{k}$ under TR operation. At the so-called Time Reversal Invariant Momentum (TRIM), $\mathbf{k}_0 = -\mathbf{k}_0$, one has $Th(\mathbf{k}_0)T^{-1} = h(\mathbf{k}_0)$, meaning that $\psi(\mathbf{k}_0)$ and $T\psi(\mathbf{k}_0)$ have the same energy and hence are degenerate. Thus we know that if the half-integer spin system has only two bands, then the two bands must be degenerate at TRIM, and consequently the system must be either a metal or semimetal. From this we see that a spin 1/2 topological insulator must be at least a four band model, this is the case for the BHZ model.

In a TR-invariant system the Hall conductance vanishes (as for example in 2D Chern insulators), so we need to find other ways to characterize the topology of the system. We expect that the index must be somehow related to the TR operator T in order to reflect this symmetry. The following construction has been proposed, based on the fact that the overlap between eigenstates $|u_{\alpha\mathbf{k}}\rangle$ and $T|u_{\beta\mathbf{k}}\rangle$ is antisymmetric, and performing a similar calculation as previously done to prove Kramers theorem

$$m_{\alpha\beta}(\mathbf{k}) = \langle u_{\alpha\mathbf{k}}|T|u_{\beta\mathbf{k}}\rangle = \sum_{mn} \langle u_{\alpha\mathbf{k}}|m\rangle\langle m|T|n\rangle\langle n|u_{\beta\mathbf{k}}\rangle = \sum_{mn} u^*_{\alpha\mathbf{k}m} U_{mn} K u_{\beta\mathbf{k}n}$$

$$= -\sum_{mn} u^*_{\beta\mathbf{k}n} U_{nm} u^*_{\alpha\mathbf{k}m} = -\langle u_{\beta\mathbf{k}}|T|u_{\alpha\mathbf{k}}\rangle = -m_{\beta\alpha}(\mathbf{k}) \quad (3\text{-}12)$$

where we have applied $-U = U^T$, this means that the so-called m-matrix is antisymmetric. Since the m-matrix is antisymmetric and has an even rank (due to the two spin species), its Pfaffian can be defined, whose square gives the determinant

$$det[m(\mathbf{k})] = (Pf[m(\mathbf{k})])^2. \tag{3-13}$$

There are two schemes to obtain the $\mathbb{Z}_2$ invariant: $(i)$from the phase of $Pf[m]$ or (ii) from the sign of $Pf[m]$. The BHZ model falls into the sign of Pfaffian scheme, in this case the $\mathbb{Z}_2$ invariant is defined using the sign of the Pfaffian at the HSP, provided it is a real number

$$(-1)^{\nu} = \prod_{i=1}^{4} Sgn(Pf[m(\mathbf{k}_{0,i})]) \tag{3-14}$$

where $\mathbf{k}_{0,i}$ is the i-th HSP. The product in $2D$ systems is among the four HSPs $(0,0),(\pi,0),(0,\pi)$ and (π,π). The Pfaffian $Pf[m]$ in these models is not necessarily complex, hence it may have no phase gradient. It has been found that $Pf[m(\mathbf{k}_{0,i})]$ remains at a fixed value of ± 1 within a particular topological phase.

3.3 Bernevig-Hughes-Zhang(BHZ)/Ferromagnetic-Metal(FMM)-Planar Junction

3.3.1 Continuous BHZ model and Lattice model for the BHZ/FMM system

In order to study properly the percolation of the edge state, we make use of a tight-binding model approach in a similar fashion as has been already applied to investigate 3D TIs [26]. To be more specific, we focus on the analysis of a strip of 2D Bernevig-Hughes-Zhang (BHZ) model [6] of width $N_{y,TI}$ in contact with a strip of 2D FMM of width $N_{y,FM}$, as can be seen in Fig. 3.3 (a). We impose periodic boundary condition (PBC) along the longitudinal $\hat{\mathbf{x}}$ direction and open boundary condition (OBC) in the transverse direction $\hat{\mathbf{y}}$, i.e., we consider a closed BHZ/FMM ribbon that looks like a cylinder. The BHZ sub-system is made up by the the spinful s and p orbitals $\psi = (s\uparrow, p\uparrow, s\downarrow, p\downarrow)^T$, with the specific representation set for the Dirac matrices as $\gamma_i = \{\sigma^z \otimes s^x, I \otimes s^y, I \otimes s^z, \sigma^x \otimes s^x, \sigma^y \otimes s^x\}$ and the TR operator defined as $T = -i\sigma^y \otimes IK$, where σ^b and s^b represent the Pauli matrices in the spin and orbital spaces, respectively. The Dirac Hamiltonian

in momentum space for the BHZ alone is written as [87]

$$\begin{aligned} H(\mathbf{k}) &= \sum_{i=1}^{3} d_i(\mathbf{k})\gamma_i = A\sin k_x\gamma_1 + A\sin k_y\gamma_2 \\ &+ \left(M - 4B + 2B\cos k_x + 2B\cos k_y\right)\gamma_3 \\ &= \begin{pmatrix} h(\mathbf{k}) & 0 \\ 0 & h^*(-\mathbf{k}) \end{pmatrix}, \end{aligned} \tag{3-15}$$

where $h(\mathbf{k}) = \sum_{i=1}^{3} d_i(\mathbf{k})\sigma^i$, parameters A and B stand for the so-called kinetic parameters, and the region $M < 0$ (for the mass term) represents the topologically nontrivial phase hosting the edge state.

Prior to the study of the lattice model for the whole system, let us focus on the continuous model for the BHZ alone and delineate the way to calculate its edge-states and respective decay-length. Following the notation introduced previously for the basis for spinful s and p orbitals, the TR operator reads as

$$T = -i\sigma_y \otimes IK = \begin{pmatrix} 0 & 0 & -1 & 0 \\ 0 & 0 & 0 & -1 \\ 1 & 0 & 0 & 0 \\ 0 & 1 & 0 & 0 \end{pmatrix} K. \tag{3-16}$$

Under the action of TR-operation, the 5 γ_i matrices are transformed as

$$\begin{aligned} T\gamma_i T^{-1} &= -\gamma_i, \quad i \in \{1,2,4,5\}, \\ T\gamma_3 T^{-1} &= \gamma_3, \end{aligned} \tag{3-17}$$

so in order to construct a 4×4 Dirac Hamiltonian $H(\mathbf{k}) = \sum_{i=1}^{5} d_i(\mathbf{k})\gamma_i$ which satisfies the TR symmetry $TH(\mathbf{k})T^{-1} = H(-\mathbf{k})$ the following relations must hold for the $\mathbf{d}$ vectors

$$\begin{aligned} d_i(\mathbf{k}) &= -d_i(-\mathbf{k}), \quad i \in \{1,2,4,5\}, \\ d_3(\mathbf{k}) &= d_3(-\mathbf{k}). \end{aligned} \tag{3-18}$$

For the BHZ model we just require the three Dirac matrices $\{\gamma_1, \gamma_2, \gamma_3\}$ in order to build up its Dirac Hamiltonian Eq. (3-15), and if we denote $d = \sqrt{d_1^2 + d_2^2 + d_3^2}$, then the four eigenstates of the system are found to be

$$|u_1\rangle = \frac{1}{\sqrt{2d(d-d_3)}}\begin{pmatrix} 0 \\ 0 \\ -d_3+d \\ d_1-id_2 \end{pmatrix}, |u_2\rangle = \frac{1}{\sqrt{2d(d-d_3)}}\begin{pmatrix} d-d_3 \\ d_1+id_2 \\ 0 \\ 0 \end{pmatrix}$$
$$|u_3\rangle = \frac{1}{\sqrt{2d(d+d_3)}}\begin{pmatrix} 0 \\ 0 \\ -d_3-d \\ d_1-id_2 \end{pmatrix}, |u_4\rangle = \frac{1}{\sqrt{2d(d+d_3)}}\begin{pmatrix} d+d_3 \\ d_1+id_2 \\ 0 \\ 0 \end{pmatrix} \quad (3\text{-}19)$$

with occupied state eigenenergies $E_1 = E_2 = -d$ (Valence Bands) and unoccupied states $E_3 = E_4 = d$ (Conduction Bands). The corresponding Pfaffian of the m-matrix for the two occupied states (VBs) as was defined more generally in Eq. (3-12) is then

$$m_{12} = \langle u_1|T|u_2\rangle = \frac{d_3}{d} = Pf(m), \quad (3\text{-}20)$$

in this way se see that the topology for this system is determined by the factor d_3/d, since from there we can calculate the topological invariant index ν with the aid of Eq. (3-14). To verify that the edge state is a TR-invariant state with spins up and down counter propagating at the edge, we first note that the block diagonal Hamiltonian in Eq. (3-15) can be written in the form

$$H(\mathbf{k}) = \begin{pmatrix} H_\uparrow(\mathbf{k}) & 0 \\ 0 & H_\downarrow(\mathbf{k}) \end{pmatrix}$$
$$= \begin{pmatrix} d_3 & d_1-id_2 & & \\ d_1+id_2 & -d_3 & & \\ & & d_3 & -d_1-id_2 \\ & & -d_1+id_2 & -d_3 \end{pmatrix}, \quad (3\text{-}21)$$

so it is possible to solve separately for the edge state for spin up and spin down channels. If we consider a model defined in the $y > 0$ half-plane and impose periodic boundary condition along the x direction, then k_x is a well defined quantity (a good quantum number) from translational invariance along x. If we perform an expansion of the $\mathbf{d}$ vector around the HSP $\mathbf{k}_0 = 0$, project its components to real space, and set the kinetic parameters in Eq. (3-15) as $A = v$ and $B = 1$, then an approximation for the d_i components reads

$$d_1 \approx vk_x = -iv\partial_x, \quad d_2 \approx vk_y = -iv\partial_y,$$
$$d_3 \approx M - \frac{1}{2}(k_x^2 + k_y^2) = M + \frac{1}{2}(\partial_x^2 + \partial_y^2). \tag{3-22}$$

The derivation is similar to the one used when calculating edge-states for the non-interacting SSH model in Section 2.1, except now we deal with a 2 dimensional system where we expect a periodic behavior along x and a decay one along y and we require to consider the spin up and spin down channels separately. We start by looking for the solution for the spin up channel, this is a 2×2 Hamiltonian which satisfies $H_\uparrow \psi_\uparrow = E_\uparrow \psi_\uparrow$. Or goal is to solve for a real space edge state $\psi_\uparrow$ that propagates along the edge with a definite momentum $|k_x|$ corresponding to an energy of $E_\uparrow = v|k_x|$, so the eigenvalue equation to solve reads

$$\{-iv\partial_x\sigma_x - iv\partial_y\sigma_y + [M + \frac{1}{2}(\partial_x^2 + \partial_y^2)]\sigma_z\}\psi_\uparrow = v|k_x|\psi_\uparrow \tag{3-23}$$

Making use of the ansatz

$$\psi \propto e^{i|k_x|x}e^{-\lambda y}\chi_\eta, \tag{3-24}$$

we find out that this wave function is an eigenstate of σ_x and the relation $\sigma_x\chi_\eta = \eta\chi_\eta = \chi_\eta$ is satisfied in such a way that the term $v|k_x|\psi_\uparrow$ is canceled in both the left and right hand sides of the equation. Then the remaining of the equation vanishes

$$\{i\lambda v\sigma_y + [M - \frac{1}{2}(|k_x|^2 - \lambda^2)]\sigma_z\}\psi_\uparrow = 0. \tag{3-25}$$

If we multiply this equation by σ_y, we obtain that the wave function has to be an eigenstate of σ_x and so we arrive to the following quadratic equation for the factor λ

$$\lambda v + [M - |k_x|^2/2] + \lambda^2/2 = 0. \tag{3-26}$$

The two roots of this equation are

$$\lambda_\pm = \frac{1}{2}\{-2v \pm \sqrt{(2v)^2 - 8[M - |k_x|^2/2]}\}. \tag{3-27}$$

Considering the case $v > 0$, in a vicinity of the topological phase transition $M \to 0$, it is the inverse of the smaller $\lambda = \lambda_+$ who provides the decay length

$$\xi_+ = \frac{1}{\lambda_+} = Sgn(-M)|\frac{v}{M - |k_x|^2/2}|. \tag{3-28}$$

The very definition of the decay length and its positivenes demands that $\xi_+ > 0$, this indicates that only the region $M < 0$ (topological nontrivial

phase) possess edge state. In a similar fashion we now look at the spin down channel which satisfies $H_{\downarrow}\psi_{\downarrow} = E_{\downarrow}\psi_{\downarrow}$. By looking at the form of the block-diagonal Dirac Hamiltonian, we notice that the only difference from the spin up channel is that now there is a minus sign for the d_1 component. We are seeking for an edge state propagating with the same magnitude of momentum $|k_x|$ but with negative energy $E_{\downarrow} = -v|k_x|$, i.e, having a negative group velocity which means it propagates in the opposite direction. Projecting the Hamiltonian to real space we get

$$\{iv\partial_x\sigma_x - iv\partial_y\sigma_y + [M + \frac{1}{2}(\partial_x^2 + \partial_y^2)]\sigma_z\}\psi_{\downarrow} = -v|k_x|\psi_{\downarrow}, \tag{3-29}$$

and from here we find that, if we employ the same ansatz as before and demand the spinor to obey the relation $\sigma_x\chi_\eta = \eta\chi_\eta = \chi_\eta$, then we could cancel out the term $-v|k_x|\psi_{\downarrow}$ who appears on both sides of the equation. Demanding the rest of the equation to vanish, in the same way as performed for the spin up case, we arrive at the very same solution for the decay length ξ_+. If we compare the methodology applied for calculating the spin up and spin down edge states, we see that both spin directions have the same decay length, and they appear only at $M < 0$. They differ only in the sign of their corresponding group velocities, this means that they propagate in opposite directions.

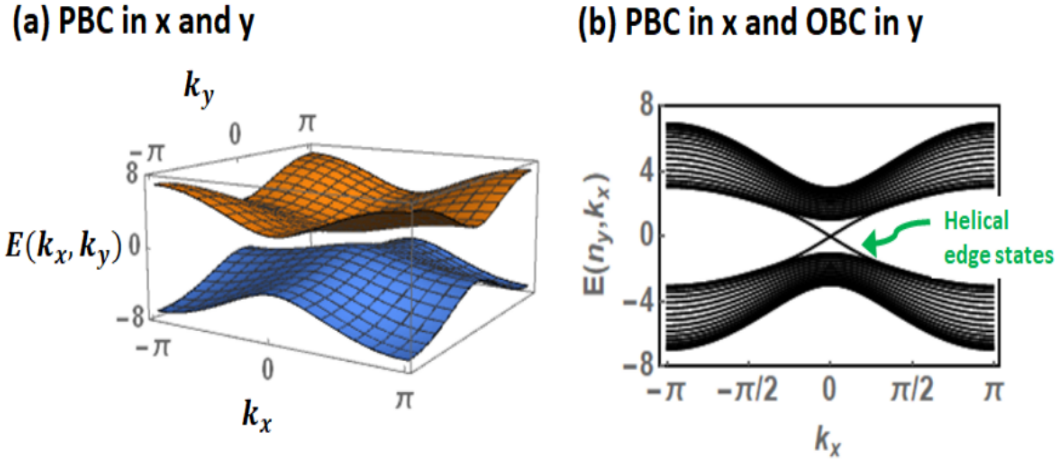

Figure 3.1: (a) The energy dispersion of BHZ model with PBC in both x and y direction. (b) The band structure of a strip of BHZ model with PBC in x and OBC in y, where the helical edge state occurs in topologically nontrivial phase.

This characteristic of finding edge states in TR-invariant TIs has been called as the QSHE, this phenomenon has been verified in many experiments

performed on HgTe quantum wells. Fig. 3.1 shows the energy dispersion for different kinds of boundary conditions imposed on the BHZ system, for the PBC in x and OBC in y we can clearly see the Dirac cone containing the above mentioned edge states who also satisfy the so called spin-momentum locking. Fig. 3.2 explains what occurs during a topological phase transition in this system, we notice that in the topologically nontrivial phase appears the so-called Dirac cone containing the helical edge states, this is a very different situation from that occurring for the SSH system that was presented in Fig. 2.2.

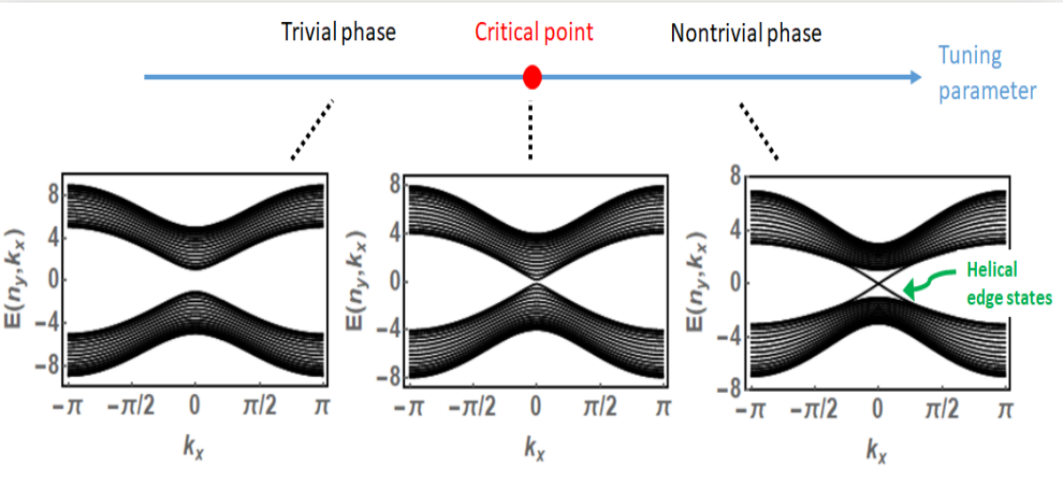

Figure 3.2: Schematics of band inversion at the critical point of a tuning parameter in a strip of 2D time-reversal invariant topological insulator. After the system enters the topologically nontrivial phase, helical edge states that consist of counterpropagating spins occur, known as the QSHE.

We proceed now to delineate the lattice model for the BHZ/FMM ribbon. Due to the contact and influence from the TI, we assume the conduction band of the FMM to be split into s-like and p-like orbitals, both of which are affected by the magnetization $\mathbf{S}$ of the FMM by means of the so-called exchange coupling. The Hamiltonian operator for the whole system in lattice space is written as

$$
\begin{aligned}
H &= \sum_{i\in TI}\left\{-itc^{\dagger}_{is\uparrow}c_{i+ap\uparrow}-itc^{\dagger}_{ip\uparrow}c_{i+as\uparrow}+itc^{\dagger}_{is\downarrow}c_{i+ap\downarrow}+itc^{\dagger}_{ip\downarrow}c_{i+as\downarrow}+h.c.\right\}\\
&+ \sum_{i\in TI}\left\{-tc^{\dagger}_{is\uparrow}c_{i+bp\uparrow}+tc^{\dagger}_{ip\uparrow}c_{i+bs\uparrow}-tc^{\dagger}_{is\downarrow}c_{i+bp\downarrow}+tc^{\dagger}_{ip\downarrow}c_{i+bs\downarrow}+h.c.\right\}\\
&+ \sum_{i\in TI}\left(M+4t'-\mu\right)\left\{c^{\dagger}_{is\uparrow}c_{is\uparrow}+c^{\dagger}_{is\downarrow}c_{is\downarrow}\right\}+\sum_{i\in TI}\left(-M-4t'-\mu\right)\left\{c^{\dagger}_{ip\uparrow}c_{ip\uparrow}+c^{\dagger}_{ip\downarrow}c_{ip\downarrow}\right\}\\
&+ \sum_{i\in TI,\delta}\left(-t'\right)\left\{c^{\dagger}_{is\uparrow}c_{i+\delta s\uparrow}-c^{\dagger}_{ip\uparrow}c_{i+\delta p\uparrow}+c^{\dagger}_{is\downarrow}c_{i+\delta s\downarrow}-c^{\dagger}_{ip\downarrow}c_{i+\delta p\downarrow}+h.c.\right\}-\mu_F\sum_{i\in FM,I\sigma}c^{\dagger}_{iI\sigma}c_{iI\sigma}\\
&- t_F\sum_{i\in FM,\delta I\sigma}\left\{c^{\dagger}_{iI\sigma}c_{i+\delta I\sigma}+c^{\dagger}_{i+\delta I\sigma}c_{iI\sigma}\right\}+\sum_{i\in FM,I\sigma}J_{ex}\mathbf{S}\cdot c^{\dagger}_{iI\alpha}\boldsymbol{\sigma}_{\alpha\beta}c_{iI\beta}\\
&- t_B\sum_{i\in BD,I\sigma}\left\{c^{\dagger}_{iI\sigma}c_{i+bI\sigma}+c^{\dagger}_{i+bI\sigma}c_{iI\sigma}\right\}. \qquad (3\text{-}30)
\end{aligned}
$$

It is important to point out that in Eq. (3-30) the part of the Hamiltonian representing the BHZ sub-system is the Fourier transform of the BHZ model whose Dirac Hamiltonian in momentum space has already been introduced in Eq. (3-15). In this equation $c_{iI\sigma}$ and $c^{\dagger}_{iI\sigma}$ stand for the electron annihilation and creation operators, $I=\{s,p\}$ for the orbital index, $\delta=\{a,b\}$ for the lattice constant along the two planar directions, $\sigma=\{\uparrow,\downarrow\}$ labels the spin index, $i=\{x,y\}$ labels the planar position, and TI, FM, BD denote the TI region, the FMM region, and the interface sites, respectively. Additionaly, from the so-called Schottky-Mott rule [88, 89], it is well known that the difference in work functions of the two materials in contact causes an adjustment of their chemical potentials, for this reason the FMM on-site energy μ_F becomes a quantity which is dependent on the specific material and whose variation shifts the FMM subbands. We denote the magnetization vector of the FMM in spherical coordinates as $\mathbf{S}=S\left(\sin\theta\cos\varphi,\sin\theta\sin\varphi,\cos\theta\right)$.

From the explicit form of the full Hamiltonian operator in second quantization Eq. (3-30), we can obtain its Eigenenergies and Eigenvectors by diagonalizing its Hamiltonian matrix, but to have a more clear idea on how to construct this matrix for a lattice model, we can draw a grid of the lattice where we enumerate each of the sites as shown in Fig. 3.4. At each of these sites there are 4 spin-orbital states composed of the spinful s and p orbitals $(s\uparrow, p\uparrow, s\downarrow, p\downarrow)$ so the number of Eigenenegies and Eigenvectors is 4 times the number of sites in the whole BHZ/FMM lattice and the Hamiltonian matrix takes the form shown in Fig. 3.5.

In order to establish a connection with realistic HgTe quantum well

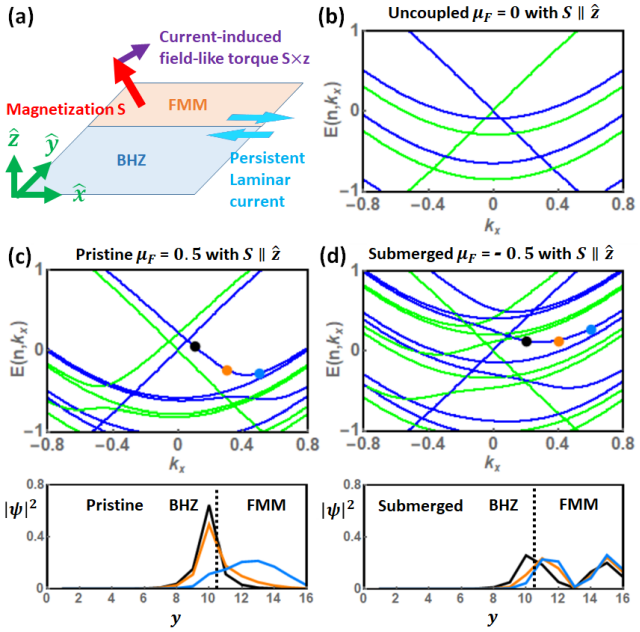

Figure 3.3: (a) Graphical representation of the lattice model for the BHZ/FMM system, where we imposed PBC along $\hat{\mathbf{x}}$ and OBC along $\hat{\mathbf{y}}$. (b) Low energy band structures corresponding to spin up (blue) and down (green) polarizations for the case when the BHZ and the FMM are uncoupled $t_B = 0$. The magnetization is set to point along $\mathbf{S} \parallel \hat{\mathbf{z}}$, the width of the BHZ is fixed at $N_{y,TI} = 10$ sites and that of the FMM at $N_{y,FM} = 6$ sites along the y direction. (c) The pristine and (d) the submerged kinds of band structures for the coupled BHZ/FMM system at interface hopping set to $t_B = 0.8$. The undeformed Dirac cone contains the edge states located at the vacuum/BHZ interface $y = 1$, whereas the deformed one contains states at the BHZ/FMM interface (dashed line). The panels at the bottom exhibit the wave function profiles $|\psi|^2$ (which have the same value as $\langle\sigma^z\rangle$) corresponding to the three selected states labelled as dots of the same colors on the band structure. This Figure has been taken from Ref. [74].

parameters, we choose the hopping or kinetic parameters to have the values

$$A = 2t \approx -3.4\text{eV} \ , \quad B = -t' \approx -17eV = 10t \ . \tag{3-31}$$

In this work we set the energy unit of the system to have the value of the hopping term $t = A/2 = -1.7\text{eV} \equiv -1$ (so we consider 1.7eV as the energy unit). Due to the finite size of this lattice model, if we consider the value $t' = -10t = 10$, then it does not appear clearly any band gap in the energy spectrum, this is a consequence of the higher order term comming from the d_3 component. When simulating this lattice model with $4t' - 2t' \cos k_x a - 2t' \cos k_y a$ and a large hopping amplitude t', then this term washes out the bulk gap. As already mentioned above, this is an obvious artifact of considering a finite size

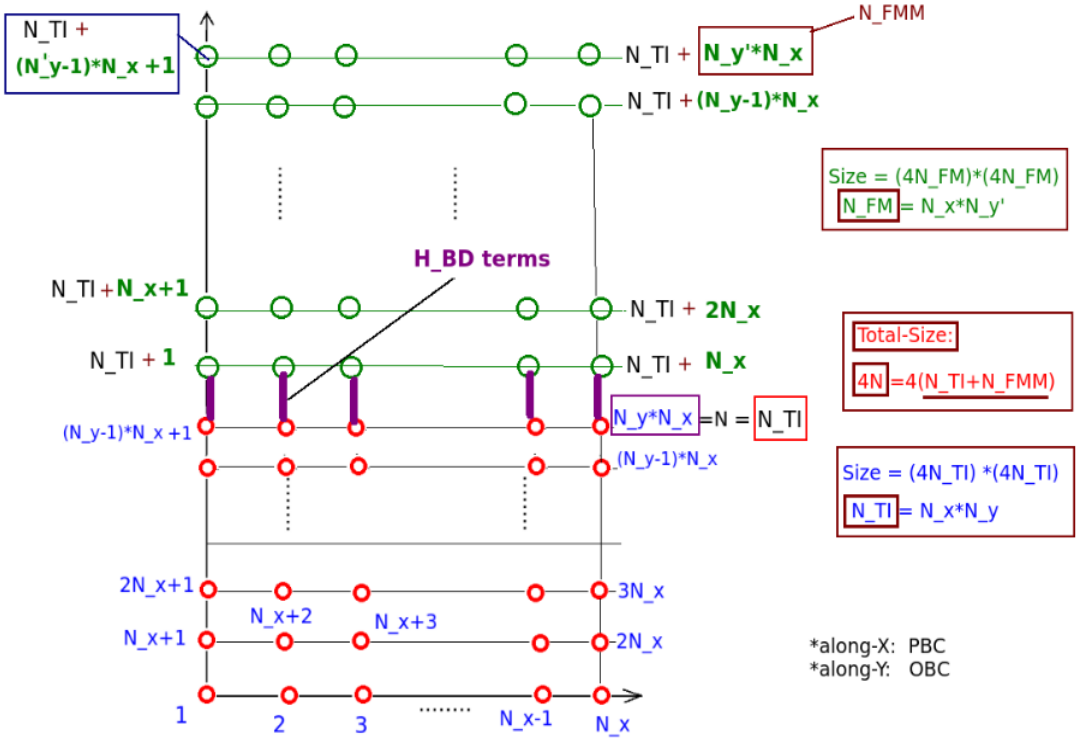

Figure 3.4: This grid permits us to visualize the lattice where we can enumerate and label each of the lattice sites. In red are the sites in the BHZ ($N_{TI} = N_{xy}$), in green the sites in the FMM ($N_{FMM} = N_x \times N'_y \equiv N_{yp}$) and the purple lines show the tight-binding interaction between the BHZ and FMM which results in the term H_{BD}. As a result the full Hamiltonian is $H_{full} = H_{TI} + H_{FMM} + H_{BD}$, this grid helps us to construct the matrix whose size is 4 times the number of lattice sites.

lattice model to simulate the continuous HgTe quantum well. To avoid these numerical issues we reduce the $t' = -10t = 10$ to $t' \approx -t = 1$ in our lattice model so as to preserve the bulk gap and show the edge state.

The other parameter we need to approximate properly is the so-called mass term M, this is relevant because the factor $A/M = 2t/M$ provides the decay length of the edge state as can be seen from the analytical expression in Eq. (3-28). Since we simulate the system on a lattice size of the order of 10×10 sites, then this decay length should not exceed some few lattice sites, otherwise we will have an undesired overlapping between the edge states which belong to the two opposite edges. From this argument we decide the value of $M = -1$ for the mass term, which certainly differs from realistic HgTe quantum wells. To perform the calculations for the local persistent currents and the magnetoelectric susceptibility (see details below) we consider room temperature conditions so we set $k_B T = 0.03$. To finalize, we set the concrete

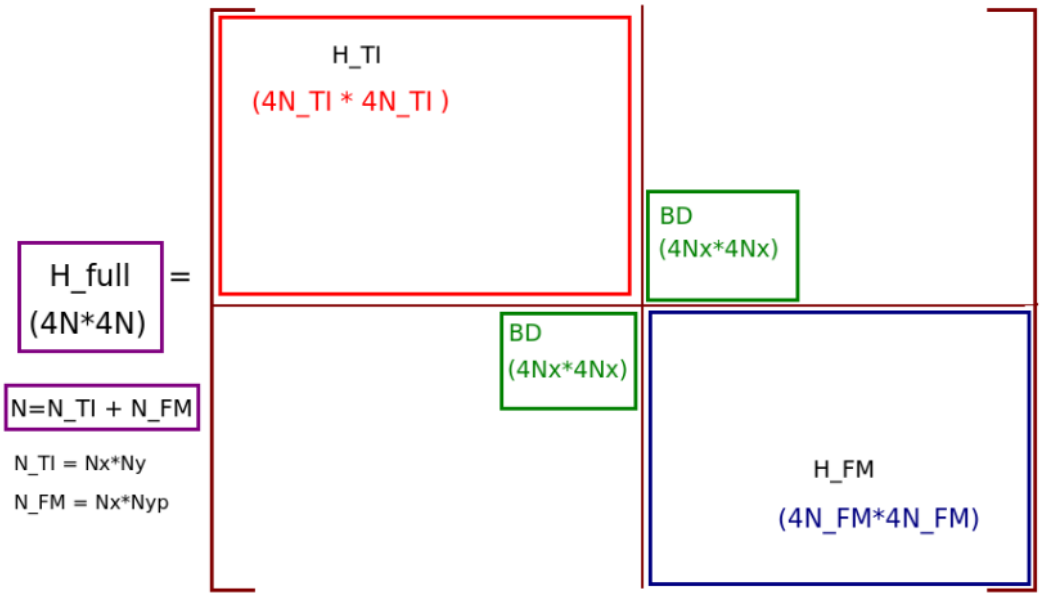

Figure 3.5: The full Hamiltonian matrix will have this form, it is block-diagonal containing H_{TI} and H_{FM} and the off-diagonal term H_{BD} having size $4N_x \times 4N_x$.

value of $t_B = 0.8$ for the interface hopping, which is assumed to be only between the same orbital and spin species. To summarize, we have set (in units of $|t| = 1.7\text{eV}$) the following parameters

$$\begin{aligned} &-t = t' = -M = t_F = 1\,, \quad \mu = 0\,, \quad \mu_F = 0.5\,(\text{pristine}) \\ &\mu_F = -0.5\,(\text{submerged})\,, \quad t_B = 0.8\,, \quad J_{ex} = 0.1\,, \\ &k_B T = 0.03\,, \end{aligned} \tag{3-32}$$

we should also emphasize that all statements made in the present investigation are fairly robust against modifications of these parameters.

3.3.2 Band structure and percolation of the edge state

We can obtain the band structure $E(n, k_x)$ of the system from Eq. (3-30) by performing a partial Fourier transform

$$c_{iI\sigma} = c_{xyI\sigma} = \sum_{k_x} e^{ik_x x} c_{k_x yI\sigma}, \tag{3-33}$$

where $c_{iI\eta}$ stands for the electron annihilation operator of orbital $I = \{s, p\}$ and spin $\sigma = \{\uparrow, \downarrow\}$ at site $i = \{x, y\}$. To make a proper comparison, in Fig. 3.3 (b) we present this band structure when the BHZ and the FMM are uncoupled $t_B = 0$, there both the edge state Dirac cone and the quadratic FMM bands are clearly noticeable. We remark that, since the FMM is sandwiched between the

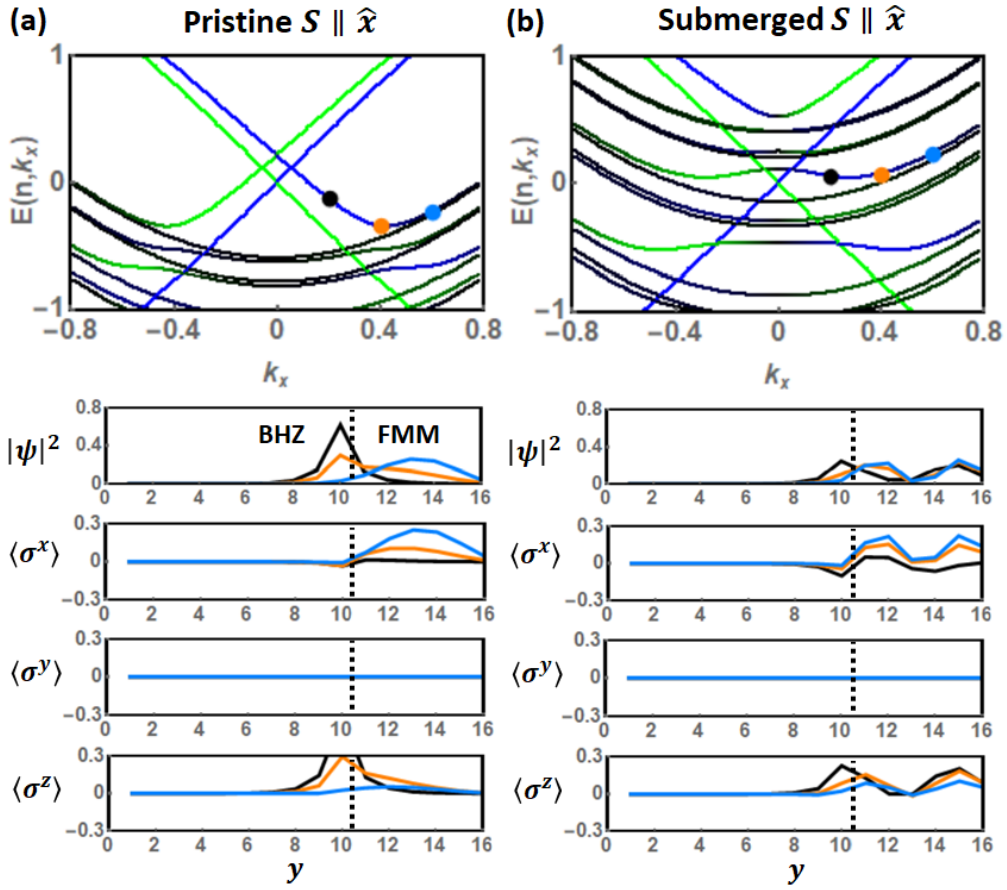

Figure 3.6: Band structures for the BHZ/FMM system with magnetization oriented along $\mathbf{S} \parallel \hat{\mathbf{x}}$, for (a) the pristine $\mu_F = 0.5$ and (b) the submerged $\mu_F = -0.5$ situations. The green and blue colors stand for the spin up and down polarizations, and the black color represents unpolarized states. In the same colors as the dots located in the dispersion are shown below the corresponding edge state wave functions and spin polarizations (spin texture). This Figure has been taken from Ref. [74].

TI and the vacuum, the FMM wave functions turn out to be confined quantum well states. In Figure 3.3 (c) we can see the so-called pristine type of band structure for the coupled BHZ/FMM strip simulated by selecting $\mu_F = 0.5$ and an interface hopping of $t_B = 0.8$, together with the corresponding percolations of the edge state, the magnetization has been set to point along the spin polarization of the edge state $\mathbf{S} \parallel \hat{\mathbf{z}}$. The Dirac cone remains gapless and at larger momenta starts merging with the FMM subbands which have the same spin polarization. If we start increasing the value of momentum, the edge state wave function $|\psi|^2 = \sum_{I\sigma} |\psi_{I\sigma}|^2$ evolves gradually from a shape highly localized at the edge to a profile that merges with the FMM quantum well state corresponding to the first harmonic. Since we can still identify the edge state Dirac cone, and the phenomena of wave function merging between the

edge state and the FMM quantum well state, we identify this state as the percolated QSH state.

The other kind of band structure is obtained by considering $\mu_F = -0.5$ and we have labelled it as the submerged type, here the Dirac point overlaps with the FMM subbands, as we can visualize in Fig. 3.3 (d). For this situation the Dirac cone at the BHZ/FMM interface is a lot more distorted and becomes exceedingly intertwined with the FMM subbands. If we track the states which originate from the Dirac cone, we find out that this Dirac cone separates into different branches and each of them therefore hybridizes with the FMM quantum well state corresponding to a different harmonic, such as the second harmonic exhibited by the $|\psi|^2$ in Fig. 3.3 (d). For both kinds of band structures the percolation is increased as we increase the value of the interface hopping t_B (not shown), as we could expect. Despite the fact that the highly intertwined Dirac cone and FMM subbands make it rather difficult to accurately locate the edge states at the BHZ/FMM interface, we should remind that the edge states at the free edge $y = 1$ remain unaltered (undistorted Dirac cone), then we still consider the states for this submerged situation as QSH states. A last observation is that whether the Dirac point is submerged or not inside the FMM subbands is something that depends also on the number of FMM subbands, this number is given by the width $N_{y,FM}$ of the FMM. For both the pristine and submerged situations, the Dirac cone situated at the vacuum/BHZ interface at $y = 1$ is undistorted by the contact to the FMM at the $y = N_{y,TI}$ junction, this means that those edge states are of the same kind as those arising from the BHZ alone.

For the other two magnetization directions $\mathbf{S} \parallel \hat{\mathbf{x}}$ and $\mathbf{S} \parallel \hat{\mathbf{y}}$, which are orthogonal to the spin polarization of the edge state, the respective results from numerical simulations are presented in Fig. 3.6. These results show that the amalgamation between edge states and quantum well states has the effect of inducing a small spin polarization pointing in the same direction of $\mathbf{S}$ for the edge states in the BHZ region close to the interface (there arises a small $\langle\sigma^x\rangle$ near $y \lessapprox 10$ as can be seen in Fig. 3.6). From this we find out that the spin polarization in the BHZ region is not anymore perfectly along $\hat{\mathbf{z}}$, therefore the presence of the magnetization alters the spin-momentum locking. In the same fashion, the percolated edge state in the FMM region is polarized in the plane spanned by $\mathbf{S}$ and $\hat{\mathbf{z}}$, instead of entirely along $\mathbf{S}$, this indicates that the spin polarization gets distorted in this region. For example, for either of these 2 kinds of band structure, the spin polarization for the $\mathbf{S} \parallel \hat{\mathbf{x}}$ case is entirely contained within the xz-plane. As we will verify in Sec. 3.3.4, such a

particular spin texture is the cause of obtaining an entirely field-like type of current-induced spin torque.

3.3.3 Laminar charge and spin currents

When the magnetization has a component S_z pointing along the spin polarization of the edge state, then the dispersion for both the pristine and submerged cases becomes asymmetric between $-k_x$ and $+k_x$ as can be seen in Fig. 3.3 (b). The explanation for this asymmetry is that such a component makes one branch of the Dirac cone to become more energetically favorable with respect to the other, this is a situation quite similar to that taking place in 2D magnetized Rashba systems [90]. Despite that this asymmetry immediately motivates us to speculate that there may exist a persistent charge current [91], we ought to keep in mind the of fact that an asymmetric dispersion does not provide a nonzero net current. This can be verified quite easily if we notice that the expectation value of the velocity operator v_x for the eigenstate $|u_{n,k_x}\rangle$ is just the group velocity [92]

$$\langle u_{n,k_x}|v_x|u_{n,k_x}\rangle = \langle u_{n,k_x}|\frac{1}{\hbar}\frac{\partial H}{\partial k_x}|u_{n,k_x}\rangle = \frac{\partial E(n,k_x)}{\hbar\partial k_x}. \tag{3-34}$$

The mean value of the current operator integrated over momentum around the BZ vanishes identically

$$\langle v_x\rangle = \sum_n \int_{-\pi}^{\pi} \frac{dk_x}{2\pi}\frac{\partial E(n,k_x)}{\hbar\partial k_x} f(E(n,k_x)) = 0\ , \tag{3-35}$$

where $f(E(n,k_x)) = 1/\left(e^{E(n,k_x)/k_BT}+1\right)$ is the Fermi function, and so we find out that there is no net current (this is known as the so-called Feynman's theorem).

In spite of the absence of a net current, the local current turns out to be nonzero. We can prove this if we evaluate the charge and spin currents directly from the lattice model by means of the next methodology. First of all, the BHZ Hamiltonian does not commute neither with σ^x nor with σ^y, from this fact we focus only on the longitudinal charge current and the spin current polarized along σ^z, and make use of the charge/spin polarization operator

$$P^a = \sum_{iI\eta\lambda} x_i c^\dagger_{iI\eta}\sigma^a_{\eta\lambda}c_{iI\lambda} \equiv \sum_{I\eta\lambda} P^a_{I\eta\lambda}\ , \tag{3-36}$$

where x_i is the longitudinal coordinate of site i, and $\sigma^a = \{\sigma^0, \sigma^z\} = \{I, \sigma^z\}$.

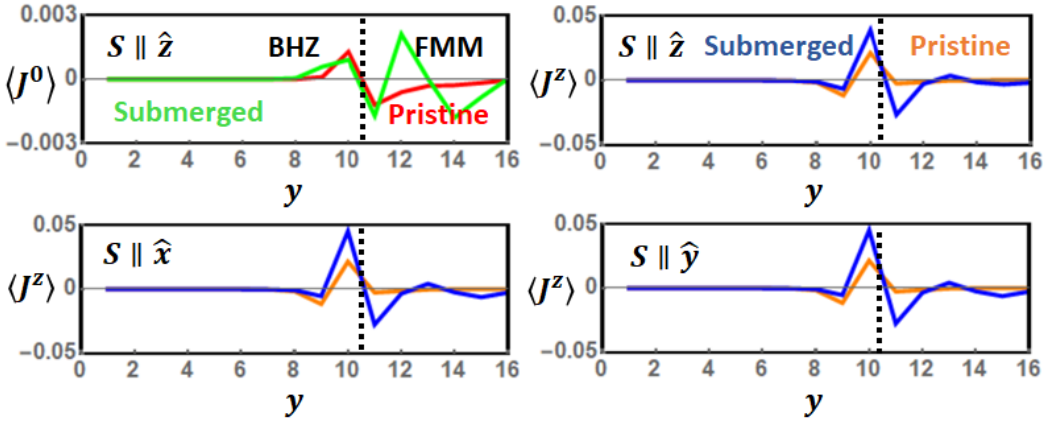

Figure 3.7: Laminar local charge current $\langle J^0(y) \rangle$ and local spin current $\langle J^z(y) \rangle$ showing variation along the y direction (but no variation along x from translational invariance), for different orientations of the magnetization $\mathbf{S} \parallel \{\hat{\mathbf{x}}, \hat{\mathbf{y}}, \hat{\mathbf{z}}\}$ and for both the pristine and the submerged situations. The charge current appears only when the magnetization has a component pointing along $\hat{\mathbf{z}}$, and if the BHZ and FMM are decoupled $t_B = 0$ then both the spin and charge currents dissapear. This Figure has been taken from Ref. [74].

From here the current operators can be obtained by using the Heisenberg equation of motion $J^a = \dot{P}^a = \frac{i}{\hbar}[H, P^a]$, as performed explicitly in Appendix A. The expectation value of the current operator in the ground state gives then the local current

$$\langle J^a \rangle = \sum_n \langle n|J^a|n\rangle f(E_n), \tag{3-37}$$

where $|n\rangle$ is the eigenstate corresponding to the eigenenergy E_n of the BHZ/FMM lattice model, and we can separate $\langle J^a \rangle$ into contributions from each bond connecting sites i and $i + a$ in order to calculate the local current.

The longitudinal charge current $\langle J^0(y) \rangle$, which is a function that depends only on the transverse coordinate y, is presented in Fig. 3.7 and from there we notice that this result features a laminar current whose direction of flow varies with y. As verified previously in Eq. (3-35), there is no net current since this quantity vanishes up to numerical precision. The local charge current is nonzero only when the magnetization has an out-of-plane component S_z, this is a consequence of the asymmetric band structure for this situation. Furthermore, both the charge and spin currents only appear when the BHZ and FMM are coupled $t_B \neq 0$, this means that this effect is entirely proximity induced. A more detailed analysis reveals that both the charge and spin currents arise from contributions comming from all the subbands and are not exclusevily due to

the edge states. This is the reason why these currents persist easily up to room temperature, representing an advantage over those induced at the topological superconductor/FMM interfaces [93, 94]. For the specific set of parameters we have chosen, the magnitude of the local charge current is of the order of $\langle J^0(y)\rangle \sim 10^{-3}et/\hbar \sim 10^{-7}$A, and its direction (the flow direction) changes sign alternating between $-\hat{\mathbf{x}}$ and $+\hat{\mathbf{x}}$ at the length scale of the lattice constant ∼nm. Making use of the Ampere's circuital law

$$B = \mu_0\langle J^0(y)\rangle/2\pi r \tag{3-38}$$

reveals that at a distance of r ∼nm above the surface, the laminar current generates a magnetic field ∼ 1Oe pointing along $\hat{\mathbf{y}}$ who alternates at the length scale of nm. Thus despite the fact that the local laminar current is not expected to manifest in the transport properties, the alternating magnetic field it generates may be in principle measurable.

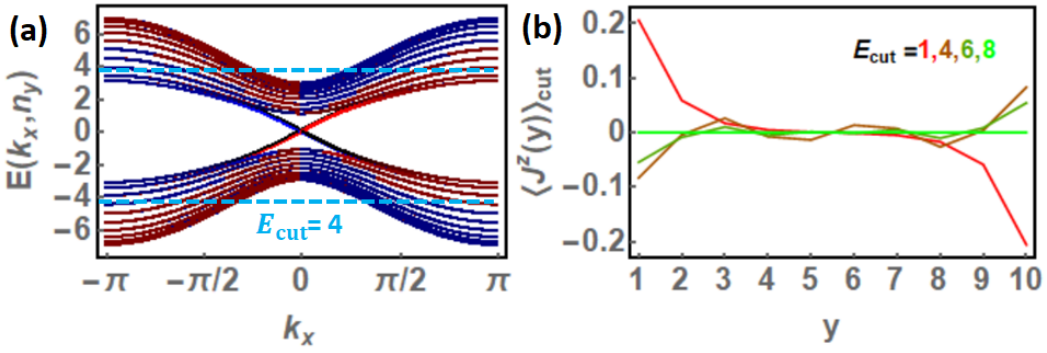

Figure 3.8: (a) The band structure for the BHZ ribbon alone having width $N_y = 10$, with its Dirac point localized at chemical potential (Fermi level of zero energy). The red and blue colors stand for the spin up and down components of the wave function near the $y = 1$ edge $\tilde{m}_{k_x,n_y}$ as defined in Eq. (3-39). (b) The local persistent spin current as a function of the transverse coordinate $\langle J^z(y)\rangle_{cut}$ which is obtained from summation of only those states within an energy window $|E(n,k_x)| < E_{cut}$. Only the contribution from the Dirac cone is obtained by considering the $E_{cut} = 1$ case, whereas the $E_{cut} = 8$ situation considers a summation over the whole band structure. The situation for $E_{cut} = 4$ is illustrated by the two dashed lines in (a), for this case only states within that energy window are summed and weighted by the Fermi function. This Figure has been taken from Ref. [74].

We have presented in Sec. 3.3.1 that the edge state of the BHZ model is made up of counterpropagating spins, from here it is natural to expect an equilibrium edge spin current to arise in the system. Notwithstanding this, we will show that this is not true, i.e., spin-polarized edge state does not necessarily imply the generation of an equilibrium edge spin current. The

reason for this is that the spin current caused by the edge state is canceled out due to the negative contribution comming from the BHZ valence bands which are also spin polarized. To make clear this phenomena, in Fig. 3.8 (a) we present the band structure of the BHZ ribbon alone, there the red and blue colors indicate the spin polarization of the eigenstates $|k_x, n_y\rangle$ close to the $y = 1$ edge

$$\tilde{m}^z_{k_x,n_y} = \sum_{1\leq y\leq N_y/2} \sigma^z_{k_x,n_y}. \tag{3-39}$$

The Dirac cone contains spin up states who propagate with positive group velocity and spin down states with negative group velocity at the $y = 1$ edge, as we would expect. Additionally, we need to consider the fact that the valence bands are also spin polarized, as well as the conduction bands although these conduction bands do not contribute due to the Fermi distribution. Furthermore, at least some regions of the valence bands have spin up but negative group velocity (red color with negative slope in Fig. 3.8 (a)), this means that those states make up a spin current *against* that generated by the edge states. The very same situation also takes place at the other edge $y = 10$.

To analyze quantitatively the contribution to the edge spin current arising from the Dirac cone and from the valence bands, we calculate the spin current in the lattice model considering only the contribution comming from the states within an energy window E_{cut} around the chemical potential

$$\langle J^z\rangle_{cut} = \sum_n \langle n|J^z|n\rangle f(E_n)\theta(E_{cut} - |E_n|) \ , \tag{3-40}$$

here $\theta(E_{cut} - |E_n|)$ stands for the step function. As is presented in Fig. 3.8 (b), the $E_{cut} = 1$ situation that considers only the Dirac cone contribution provides a finite spin current, but the case $E_{cut} = 8$ which sums over the whole band structure generates a local spin current equal to zero. So we have found out that the contribution from the bulk bands cancels out exactly that comming from the edge state Dirac cone yielding a zero local spin current. However, we could generate a finite spin current by shifting away the Dirac point from the chemical potential, or if in a given experiment we are able to measure the equilibrium spin current arising only from states within an energy window around the chemical potential [95].

On the flip side, when we put in contact the BHZ together with the FMM, a persistent local spin current is generated for both the pristine and

the submerged situations, and is a laminar flows which infiltrates or percolates into the FMM, as can be seen in Fig. 3.7. That laminar spin current appears regardless of the direction of the magnetization and the position of the Dirac point with respect to the chemical potential. The magnitude and spatial variation of this spin current differs only by approximately 20% for other magnetization directions, this can be notice if we compare the $\langle J^z \rangle$ as a function of y at $\mathbf{S} \parallel \hat{\mathbf{x}}$, $\mathbf{S} \parallel \hat{\mathbf{y}}$, and $\mathbf{S} \parallel \hat{\mathbf{z}}$ as can be visualized in Fig. 3.7.

3.3.4 Current-induced spin torque

The spin polarization induced by a longitudinal electric field $E(i,t)\hat{\mathbf{x}}$ has the following components for the three spatial directions $b = \{x, y, z\}$

$$\sigma^b(i,t) = \chi^b(i,\omega)E(i,t) \ , \tag{3-41}$$

and within our lattice model approach we can solve for this response with the aid of linear response theory, from this formalism the real part of the DC magnetoelectric susceptibility can be calculated as [96, 97]

$$\begin{aligned} &\lim_{\omega\to 0} \mathrm{Re}\chi^b(i,\omega) \\ &= -\sum_j \sum_{m,n} \langle n|\sigma^b(i)|m\rangle\langle m|J^0(j)|n\rangle \tilde{F}(E_n, E_m) \ , \end{aligned} \tag{3-42}$$

as is explained in detail in Appendix B. The distribution function $\tilde{F}(E_n, E_m)$ has a very high peak in a vicinity of the Fermi level $E_n \approx E_m \approx 0$ and decays quite rapidly as we move away as can be seen in Fig. 3.9, this means that the states close to the Fermi surface contribute the most to the response as we would expect, these states include both the Dirac cone-like bands and the FMM-like subbands in accordance to Fig. 3.3 (c) and (d).

We concentrate on the DC limit of the magnetoelectric susceptibility

$$\lim_{\omega\to 0} \mathrm{Re}\chi^b(i,\omega) \equiv \chi^b(y), \tag{3-43}$$

as a function which depends only on the transverse coordinate y due to the translational invariance along x. We also bring into our discussion some news about recent investigations on magnetized BHZ system who suggest that a damping-like spin torque could be induced by the presence of impurities [98]. This phenomena is similar to the spin mixing enhanced by disorder-induced spin-dependent scattering which was firstly uncovered in metallic spin valves and domain walls [99, 100]. Stimulated by these recent works, and also for the

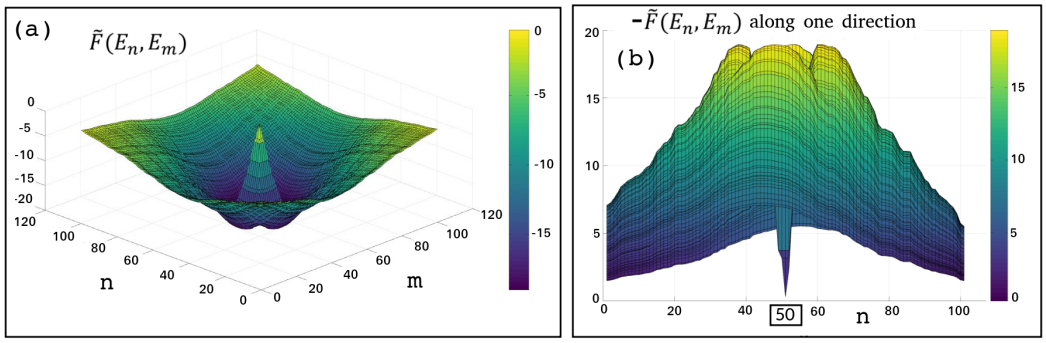

Figure 3.9: (a)Surface of ditribution $\tilde{F}(E_n, E_m)$ where the indices n and m are the indices of the array of Eigenenergies, we clearly see that at $n = 50$, which corresponds to the Fermi Level $E(n = 50) = E_F = \mu = 0$ we have $\tilde{F} = 0$. However, at a vicinity of the Fermi Level the distribution $\tilde{F}$ shows a peak (at $n \approx 70$), this is more noticeable if we invert $\tilde{F}$ as in (b) where the distribution $-\tilde{F}$ is plot along one direction, the fact that this distribution decays very rapidly from the peak justifies our approach of just considering approximately 100 states in the vicinity of the Fermi Level, those who contribute more to the response. This is a general feature of the distribution $\tilde{F}$ which is independent of the input parameters.

necessity of wiping out some numerical ambiguities as is detailed in Appendix B, we introduce some random impurities into the BHZ/FMM junction

$$H_{imp} = U_{imp} \sum_{i \in imp, I\sigma} c^{\dagger}_{iI\sigma} c_{iI\sigma}, \tag{3-44}$$

where $i \in imp$ indicate the (random) spots at which impurities are located. We set a quite large impurity potential $U_{imp} = 4$ and density $n_{imp} = 10\%$ with the purpose of drawing some relevance into TMD-based 2D TIs, where a quite important amount of defects, such as missing sulfur atoms, are known to be a realistic matter [101–104]. The magnetoelectric susceptibility χ^b is therefore solved from Eq. (3-42) with the usage of the eigenstates $|n\rangle$ of the whole system including impurities.

The solutions for the magnetization directions $\mathbf{S} \parallel \hat{\mathbf{z}}$ and $\mathbf{S} \parallel \hat{\mathbf{x}}$ are shown in Fig. 3.10, there some values for the magnetoelectric susceptibility averaged along the longitudinal direction

$$\chi^z(y) \equiv \sum_{x=1}^{N_x} \chi^z(x, y)/N_x \tag{3-45}$$

are presented for a specific impurity configuration. Near the free edge $y = 1$ the nonzero value of $\chi^z(y)$ is due to the Edelstein effect of the BHZ model alone,

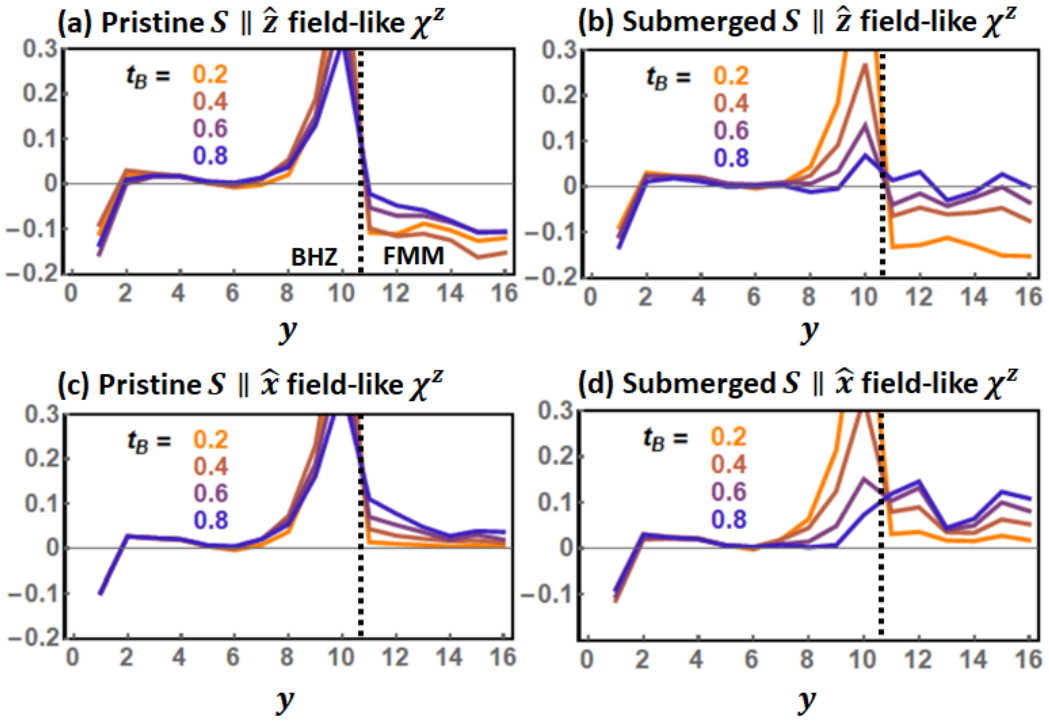

Figure 3.10: Field-like component of the magnetoelectric susceptibility $\chi^z(y)$ in the BHZ/FMM junction which, after the average over x, depends on the transverse coordinate y only. This response function is plotted for different values of interface hopping t_B, for the two different types of band structures and magnetization directions: (a) Pristine $\mathbf{S} \parallel \hat{\mathbf{z}}$, (b) submerged $\mathbf{S} \parallel \hat{\mathbf{z}}$, (c) pristine $\mathbf{S} \parallel \hat{\mathbf{x}}$, and (d) submerged $\mathbf{S} \parallel \hat{\mathbf{x}}$. The damping-like components are zero $\chi^x = \chi^y = 0$. The BHZ region is located at $y \leq 10$ whereas the FMM region at $y > 10$. The response (negative) at the free edge $y = 1$ is due to the Edelstein effect for the single BHZ sub-system. This Figure has been taken from Ref. [74].

i.e., is a current induced spin polarization produced by the edge state, in an exact analogy to what happens in 3D TIs [105–109]. Considering a mean free or relaxation time of the order of $\tau \sim 10^{-14}$s and a usual experimental electric field of magnitude $E \sim 10^4$kgm/Cs^2, then we get that the induced spin polarization at the free edge turns out to be of the order of 10^{-7} (in units of μ_B). On the other hand, at the $y = 10$ interface where the BHZ model is in contact with the FMM, the modulus of $\chi^z(y)$ is quite large at small interface hopping $t_B = 0.2$ but diminishes at larger t_B. The spatial profile for the response function $\chi^z(y)$ penetrates into the FMM for both the pristine and the submerged cases, and varies with t_B in a quite complex form. Band structures presented in Fig. 3.3 (c) and (d) explain very clearly the enhancement of χ^z arising from interface hopping: In comparison to an isolated BHZ system, the BHZ/FMM junction contains a lot more states at the chemical potential comming from the FMM

sub-bands ($|n\rangle$ and $|m\rangle$ in Eq. (3-42)) who also participate in the particle-hole excitation process for the magnetoelectric response. Furthermore, the FMM wave functions and the edge state wave functions have an important overlap which comes from the percolation of the edge state, this yields nonzero matrix elements $\langle n|\hat{O}|m\rangle$ in Eq. (3-42) which contribute to the correlator. Since an isolated FMM does not exhibit Edelstein effect, the nonzero $\chi^z(y)$ inside the FMM region $y \in FM$ is entirely proximity induced and arises from the contact to the BHZ.

To understand the role of impurities in improving our calculation of the response function, an issue which is explained in Appendix B, we should keep in mind how impurities permit to lift degeneracies in the system and in that way improve the overlap of the 3 distributions that make up the function (also a distribution) $\tilde{F}(E_n, E_m)$, these are $\frac{\eta}{(\omega-E_n)^2+\eta^2}$, $\left(\frac{1}{\pi}\frac{\partial f(\omega)}{\partial \omega}\right)$ and $\frac{\eta}{(\omega-E_m)^2+\eta^2}$:

$$\tilde{F}(E_n, E_m) \approx \int d\omega \, \frac{\eta}{(\omega - E_n)^2 + \eta^2} \left(\frac{1}{\pi}\frac{\partial f(\omega)}{\partial \omega}\right) \frac{\eta}{(\omega - E_m)^2 + \eta^2} \quad \text{(3-46)}$$

The fact is that the BHZ model alone has a lot of degeneracies coming from spin (Kramers Theorem), left-right edge, and spatial symmetries. In the BHZ/FMM the spectrum is more full because of the metallic bands of FMM (TR-invariance is broken), but still there is a lot of degeneracies. Only when we add impurities the spectrum becomes smooth and hence the numerics for susceptibility becomes more reliable. This feature is clearly seen in Fig. 3.11 where we plot the Energy-spectrum of the system for the 3 above mentioned situations.

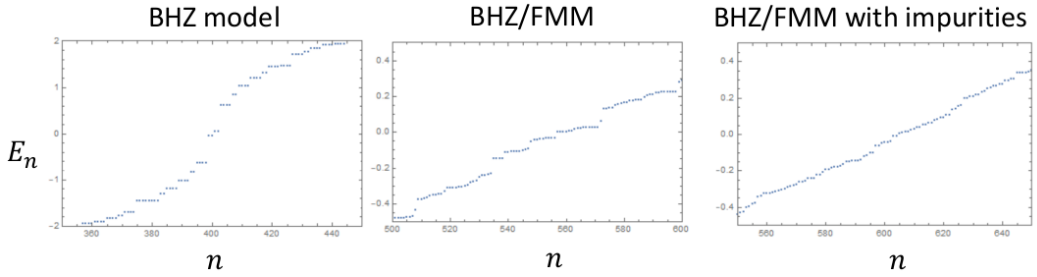

Figure 3.11: The above 3 figures show how the eigenenergies E_n have a lot of degeneracies, so the numerics is not be very accurate. Unless we put in impurities, in this case the spectrum becomes more smooth and numerical accuracy is improved.

The effect of removing degeneracies is shown schematically in Fig. 3.12, where the discrete eigenstates are broadened by a Lorentzian (blue triangles).

The susceptibility is basically the overlap of these Lorentzians times derivative of the Fermi function (green) as Eq. (3-46) tells us, times the current-spin correlator $\langle n|\sigma^b(i)|m\rangle\langle m|J^0(j)|n\rangle$ as Eq. (3-42) shows explicitly. So it is important to remove the degeneracies to have more overlap between states, especially near the chemical potential (red line), to increase the accuracy. The overlap of these Lorentzians basically gives the particle-hole excitation in the many-body language.

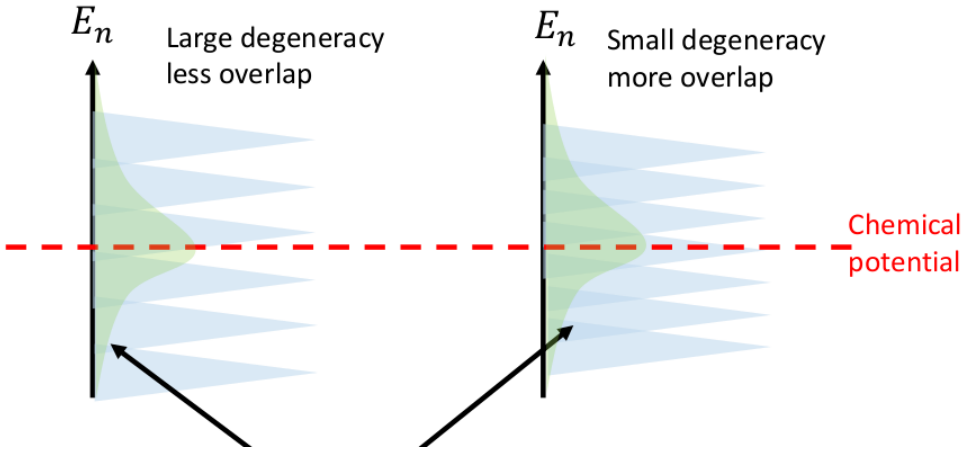

Figure 3.12: This schematic figure explains why we try to smoothen the Chemical Spectrum using impurities. The discrete eigenstates are broadened by a Lorentzian (blue triangles) as indicated by the arrows. The susceptibility is basically the overlap of these Lorentzians times derivative of the Fermi function (green) times the current-spin correlator. It is clear why states closer to the Fermi Level or chemical potential (red line) contribute more to the response, just because here the correlation is larger.

Inside the FMM region the average magnetoelectric susceptibility is calculated as

$$\chi_F^b \equiv \sum_{y\in FM} \chi^b(y)/N_{y,FM}, \tag{3-47}$$

and is this average inside the FMM region what produces the spin torque on the magnetization $\mathbf{S}$. For an isolated BHZ model we know that the current-induced spin polarization is polarized along $\hat{\mathbf{z}}$, from this result it is customary to define the field-like torque in the FMM to point along $\hat{\mathbf{S}} \times \hat{\mathbf{z}}$ and the damping-like torque to point along $\hat{\mathbf{S}} \times (\hat{\mathbf{S}} \times \hat{\mathbf{z}})$, because this is what occurs in the usual metallic thin film spin-transfer torque (STT) devices. We encounter that if the magnetization lies in the xy-plane or entirely points along $\hat{\mathbf{z}}$, then only χ_F^z is nonzero out of the three components $\chi_F^b = \{\chi_F^x, \chi_F^y, \chi_F^z\}$. This result implies that the spin torque is entirely field-like if the magnetization belongs to the xy-plane, and of course there is no any torque when the

magnetization points out-of-plane $\mathbf{S} \parallel \hat{\mathbf{z}}$. If we consider other directions for the magnetization, then a small damping-like component develops (note that our treatment neglects other more complex phenomena such as spin-orbit torque [18, 19] and spin relaxation). This situation is a lot different from the STT in usual metallic heterostructures [16, 17] or that induced by means of the spin Hall effect [110, 111], since there the plane wave states produce both field-like and damping-like torque at any orientation set for the magnetization.

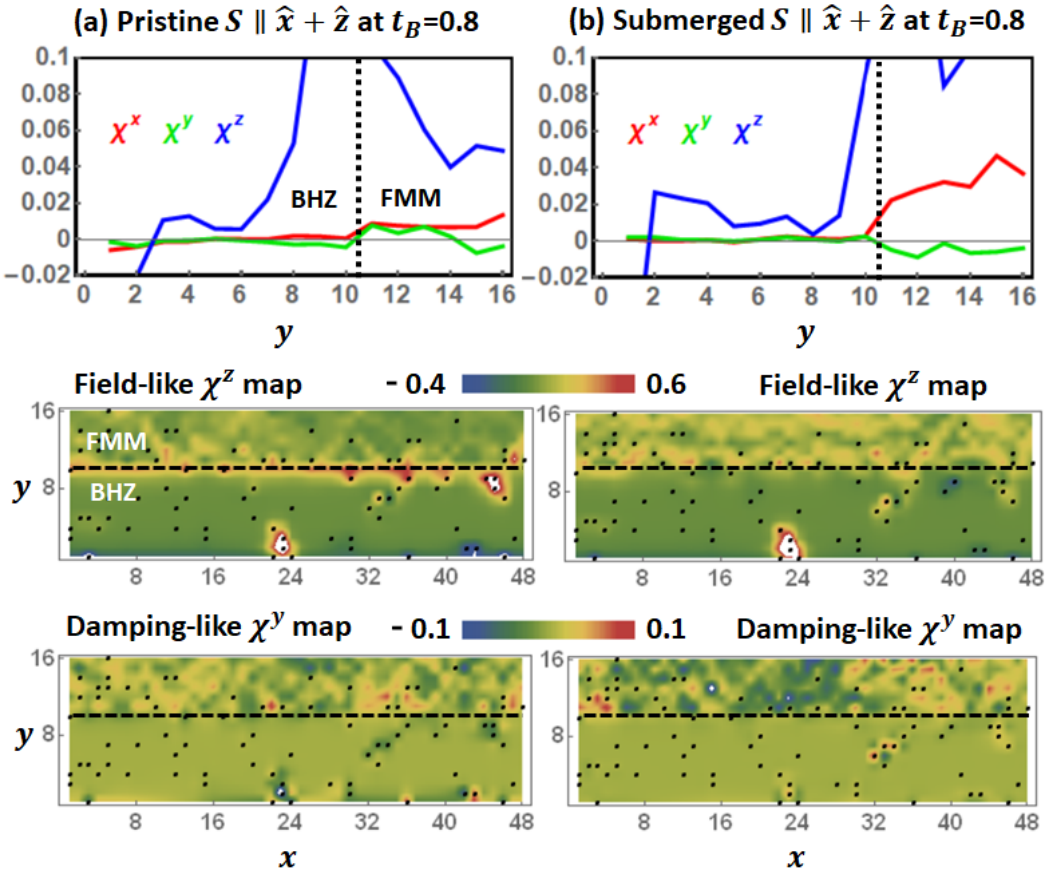

Figure 3.13: Magnetoelectric susceptibility χ^b for a magnetization oriented along $\mathbf{S} \parallel \hat{\mathbf{x}} + \hat{\mathbf{z}}$ averaged over longitudinal position x for a specific random impurity configuration, for both the (a) pristine and (b) submerged situations. The spatial surfaces for both the field-like χ^z and damping-like χ^y components are presented in lower panels, there the black dots represent the fixed positions for the impurities. This Figure has been taken from Ref. [74].

In Figure 3.13 we can see the simulation results for the magnetization oriented along $\mathbf{S} \parallel \hat{\mathbf{x}} + \hat{\mathbf{z}}$, this result exhibits both the field-like χ^z and the damping-like χ^y components. It turns out that the field-like component is dominant and usualy one order of magnitude larger than the damping-like component. If we look more closely, we could notice that near the two edges of

the BHZ region only, both χ^z and χ^y are locally enhanced at the positions of the impurities, this is clear from the local $\{\chi^y, \chi^z\}$ map shown in Fig. 3.13. This phenomena does not take place inside the FMM region, there the magnitude of both components does not exhibit any correlation with the locations of the impurities. This kind of correlation holds for both the pristine and the submerged kinds of band structures. If we apply a typical external electric charge current $j_c \sim 10^{11}\mathrm{A/m}^2$, the spin polarization induced as Eq. (3-41) tells us produces a spin torque, and the dynamics for the magnetization is subjected to the Landau-Lifshitz equation

$$\frac{d\mathbf{S}}{dt} = \frac{J_{ex}}{\hbar}\left[\frac{1}{N_{y,FM}}\sum_{i\in FM}\boldsymbol{\sigma}(i)\right]\times\mathbf{S}\,, \tag{3-48}$$

this is just the the numerical values of χ_F^b multiplied by GHz, as detailed in Appendix B. Despite the fact that our BHZ/FMM side junction differs from the actual experimental setup where the TMD is frequently deposited on the top of the FMM thin film, the absolute modulus we have found for the spin torque is fairly consistent with that obtained from actual experiments [78–83].

3.4 Outlook on the p-orbitals for the BHZ model and Exchange term in the FMM

In the model studied in this Chapter, we have considered that for both spinful s and p orbitals we have spin $\sigma =\uparrow,\downarrow$ corresponding to spin $1/2$ and $-1/2$ respectively, so transition and mixing terms between these states are possible. However, this is actually incorrect because p orbitals have orbital angular momentum $l = 1$ which must be added to the spin angular mometum $s = 1/2$ so we should consider 4 states for these p orbitals which correspond to $|3/2, 3/2\rangle, |3/2, 1/2\rangle, |3/2, -1/2\rangle, |3/2, -3/2\rangle$, in this way the model has a total of 6 bands instead of just 4 as we considered. Notwithstanding that, only 4 bands will actually be important at low energies, and for p orbitals these correspond to states $|3/2, 3/2\rangle$ and $|3/2, -3/2\rangle$, so for p orbitals spin $\sigma =\uparrow,\downarrow$ correspond to spin $3/2$ and $-3/2$ respectively. Here enters a selection rule that forbids any transition or mixing term between states with total angular momentum projection of $3/2$ and $-3/2$ or viceversa, this implies that we need to modify our 4×4 Pauli matrices so there cannot be mixing terms between these 2 states. This will modify the Pauli exchange term in the ferromagnet, because it will be equivalent to consider there only the term $\sigma_z S_z$ so in order to correct our model we should wipe out terms $\sigma_x S_x + \sigma_y S_y$ in that exchange

term which is the same as using the following spin-orbit 4×4 matrices

$$\sigma_x = \begin{pmatrix} 0 & 0 & 1 & 0 \\ 0 & 0 & 0 & 0 \\ 1 & 0 & 0 & 0 \\ 0 & 0 & 0 & 0 \end{pmatrix}, \quad \sigma_y = \begin{pmatrix} 0 & 0 & -i & 0 \\ 0 & 0 & 0 & 0 \\ i & 0 & 0 & 0 \\ 0 & 0 & 0 & 0 \end{pmatrix}, \quad \sigma_z = \begin{pmatrix} 1 & 0 & 0 & 0 \\ 0 & 1 & 0 & 0 \\ 0 & 0 & -1 & 0 \\ 0 & 0 & 0 & -1 \end{pmatrix},$$

This modification has been considered by MSc student Julian Zanon together with his advisor Prof Carlos Egues at IFSC-USP to study a more realistic BHZ model and calculate its band structure, edge state and spin texture.

4
Conclusions

If we would like to summarize our first project in one phrase, we could say that we have developed a tool which, taking into account Green's function formalism together with T-matrix approximation, allows us to corroborate the bulk-edge correspondence and the quantum criticality in weakly interacting 1D TIs. Considering specifically the SSH model and introducing there nearest-neighbor interactions, we found out that a spectral function indicating gap-closing is still a definite signature for a topological phase transition even under the influence of interactions, so we verified that interactions can also drive topological phase transitions. With the aid of T-matrix formalism, we can identify the edge state from the LDOS in a vicinity of the impurity (edge) site, this edge state is found to be localized at the same sublattice as the noninteracting situation. The Hartree term of the self-energy is responsible for shifting the whole energy spectrum if the interaction destroys particle-hole symmetry, and since the edge state is always localized in the middle of the gap, then we show that interactions are able to shift away this edge state from zero energy (so interactions induced an effective chemical potential). If we extract the critical exponent from the decay length of the edge state then we find out that the system remains in the same universality class despite the presence of interactions, this is valid at least within our treatment that limits calculations to just one-loop approximation and the T-matrix approximation which avoids considering interference diagrams.

We hope that the formalism we have followed could be extended to investigate similar characteristics for TIs and TSCs in other dimensions and symmetry classes, and in addition to consider many other different types of interactions. In higher dimensions we could simulate the edge state by a line or a surface of impurities within the T-matrix approximation approach. We focused just on a specific type of interaction whose self-energy is frequency independent, so it will be interesting to study other kinds of self-energies which are frequency-dependent, such as those that arise from electron-phonon interactions, since for this situation the quasiparticle lifetime is altered and so the spectral function exhibits a broadening. For those more

general situations, an interesting research project could be the investigation of the way in which the broadened spectral functions impact the feature of gap-closing. Furthermore, by selecting the proper minimal Dirac models we could simulate systems which belong to different symmetry classes. Another interesting proposal is the investigation of the robustness of the topological and non-topological edges states which appear in the quantum dots of Ref. [54] if they become subjected to the influence of the electron-electron scattering considered here. Certainly a lot of research is still required to establish if the results we obtained here would still be valid in such systems with confined geometry as is the case for quantum dots.

In a similar fashion a phrase to summarize our second project would be to state that we investigated the percolation of QSHE into an adjacent FMM with the aid of a lattice model and unveiled some important physical consequences from this percolation like the generation of local charge and spin currents as well as a current induced spin-torque. Due to the difference in work functions of the two materials (BHZ and FMM) in contact, the band structure of the whole system (BHZ/FMM junction) exhibits a pristine/submerged dichotomy, this has a strong influence in the percolation or infiltration of the edge state from the BHZ into the FMM. The spin momentum-locking in a vicinity of the TI/FMM interface as well as the spin polarization inside the FMM region are altered due to the amalgamation or merging between the edge states of the BHZ and the quantum well states of the FMM. From the asymmetry of the band structure obtained when the magnetization of the FMM has a component along the quantization axis ($\hat{\mathbf{z}}$ axis), which is the direction of the spin polarization for the BHZ alone, we uncover a laminar flow of local persistent charge current. We also unveil a laminar flow of local persistent spin current at any direction of the magnetization but, as well as the for the charge current, it is proximity induced which means that it only appears if the materials are joined by a finite value of interface hopping t_B.

It turns out that at the positions of the impurites (or in a vicinity) there is a dramatical enhancement of the current-induced spin polarization as is confirmed by visualizing the spatial surface of the respective response function. However, we see that this phenomena only occurs at the edges of the BHZ and there is not any correlation with the impurity positions inside the FMM. The current induced spin torque results entirely field-like if the magnetization lies in the xy-plane or is oriented along the $\hat{\mathbf{z}}$ axis (in this last case there is no net torque). However, at other orientations for the magnetization there appears a

damping-like component, but this is usually one order of magnitude smaller than the field-like component. Since these results enable us to understand better the role of edge states in 2D TI-based spintronic systems, it would be relevant to apply the same kind of lattice model approach to more realistic cases similar to the experimental setups, for instance, when the TI is put on the top of the FMM (3D case).

Bibliography

[1] V. KLITZING; G. DORDA; M. PEPPER, K.. **New method for high-accuracy determination of the fine-structure constant based on quantized hall resistance**. Phys. Rev. Lett., 45:224438, Aug 1980.

[2] HALDANE, F. D. M.. **Model for a quantum hall effect without landau levels: Condensed-matter realization of the "parity anomaly"**. Phys. Rev. Lett., 61:2015–2018, Oct. 1988.

[3] KANE, C. L.; MELE, E. J.. **Quantum spin hall effect in graphene**. Phys. Rev. Lett., 95:226801, Nov. 2005.

[4] BERNEVIG, B. A.; ZHANG, S.-C.. **Quantum spin hall effect**. Phys. Rev. Lett., 96:106802, Mar 2006.

[5] KÖNIG, M.; WIEDMANN, S.; BRÜNE, C.; ROTH, A.; BUHMANN, H.; MOLENKAMP, L. W.; QI, X.-L. ; ZHANG, S.-C.. **Quantum spin hall insulator state in hgte quantum wells**. Science, 318(5851):766–770, 2007.

[6] BERNEVIG, B. A.; HUGHES, T. L. ; ZHANG, S.-C.. **Quantum spin hall effect and topological phase transition in hgte quantum wells**. Science, 314(5806):1757–1761, 2006.

[7] SU, W. P.; SCHRIEFFER, J. R. ; HEEGER, A. J.. **Solitons in polyacetylene**. Phys. Rev. Lett., 42:1698–1701, June 1979.

[8] KÖNIG, M.; BUHMANN, H.; MOLENKAMP, L. W.; HUGHES, T.; LIU, C.-X.; QI, X.-L. ; ZHANG, S.-C.. **The quantum spin hall effect: Theory and experiment**. J. Phys. Soc. Jpn., 77(3):031007, 2008.

[9] ZHOU, B.; LU, H.-Z.; CHU, R.-L.; SHEN, S.-Q. ; NIU, Q.. **Finite size effects on helical edge states in a quantum spin-hall system**. Phys. Rev. Lett., 101:246807, Dec. 2008.

[10] QI, X.-L.; ZHANG, S.-C.. **Topological insulators and superconductors**. Rev. Mod. Phys., 83:1057–1110, Oct. 2011.

[11] RYU, S.; SCHNYDER, A. P.; FURUSAKI, A. ; LUDWIG, A. W. W.. **Topological insulators and superconductors: tenfold way and dimensional hierarchy**. New J. Phys., 12(6):065010, 2010.

[12] CHIU, C.-K.; TEO, J. C. Y.; SCHNYDER, A. P. ; RYU, S.. **Classification of topological quantum matter with symmetries**. Rev. Mod. Phys., 88:035005, Aug 2016.

[13] SCHNYDER, A. P.; RYU, S.; FURUSAKI, A. ; LUDWIG, A. W. W.. **Classification of topological insulators and superconductors in three spatial dimensions**. Phys. Rev. B, 78:195125, Nov. 2008.

[14] KITAEV, A.. **Periodic table for topological insulators and superconductors**. AIP Conf. Proc., 1134:22, May 2009.

[15] MELLNIK, A. R.; LEE, J. S.; RICHARDELLA, A.; GRAB, J. L.; MINTUN, P. J.; FISCHER, M. H.; VAEZI, A.; MANCHON, A.; KIM, E.-A.; SAMARTH, N. ; RALPH, D. C.. **Spin-transfer torque generated by a topological insulator**. Nature, 511:449, Jul 2014.

[16] BERGER, L.. **Emission of spin waves by a magnetic multilayer traversed by a current**. Phys. Rev. B, 54:9353–9358, Oct 1996.

[17] SLONCZEWSKI, J.. **Current-driven excitation of magnetic multilayers**. J. Magn. Magn. Mater., 159(1):L1 – L7, 1996.

[18] MANCHON, A.; ZHANG, S.. **Theory of nonequilibrium intrinsic spin torque in a single nanomagnet**. Phys. Rev. B, 78:212405, Dec 2008.

[19] MANCHON, A.; ZHANG, S.. **Theory of spin torque due to spin-orbit coupling**. Phys. Rev. B, 79:094422, Mar 2009.

[20] MAHENDRA, D. C.; GRASSI, R.; CHEN, J.-Y.; JAMALI, M.; REIFSNYDER HICKEY, D.; ZHANG, D.; ZHAO, Z.; LI, H.; QUARTERMAN, P.; LV, Y.; LI, M.; MANCHON, A.; MKHOYAN, K. A.; LOW, T. ; WANG, J.-P.. **Room-temperature high spin-orbit torque due to quantum confinement in sputtered bixse(1-x) films**. Nat. Mater., 17:800, 2018.

[21] YOKOYAMA, T.; ZANG, J. ; NAGAOSA, N.. **Theoretical study of the dynamics of magnetization on the topological surface**. Phys. Rev. B, 81:241410, Jun 2010.

[22] SAKAI, A.; KOHNO, H.. **Spin torques and charge transport on the surface of topological insulator**. Phys. Rev. B, 89:165307, Apr 2014.

[23] FISCHER, M. H.; VAEZI, A.; MANCHON, A. ; KIM, E.-A.. **Spin-torque generation in topological insulator based heterostructures**. Phys. Rev. B, 93:125303, Mar 2016.

[24] NDIAYE, P. B.; AKOSA, C. A.; FISCHER, M. H.; VAEZI, A.; KIM, E.-A. ; MANCHON, A.. **Dirac spin-orbit torques and charge pumping at the surface of topological insulators**. Phys. Rev. B, 96:014408, Jul 2017.

[25] OKUMA, N.; NOMURA, K.. **Microscopic derivation of magnon spin current in a topological insulator/ferromagnet heterostructure**. Phys. Rev. B, 95:115403, Mar 2017.

[26] GHOSH, S.; MANCHON, A.. **Spin-orbit torque in a three-dimensional topological insulator–ferromagnet heterostructure: Crossover between bulk and surface transport**. Phys. Rev. B, 97:134402, Apr 2018.

[27] ZEGARRA, A.; CANDIDO, D. R.; EGUES, J. C. ; CHEN, W.. **Corroborating the bulk-edge correspondence in weakly interacting one-dimensional topological insulators**. Phys. Rev. B, 100:224438, Aug 2019.

[28] ZAK, J.. **Berry's phase for energy bands in solids**. Phys. Rev. Lett., 62:2747–2750, June 1989.

[29] ESSIN, A. M.; GURARIE, V.. **Bulk-boundary correspondence of topological insulators from their respective green's functions**. Phys. Rev. B, 84:125132, Sep 2011.

[30] NAYAK, C.; SIMON, S. H.; STERN, A.; FREEDMAN, M. ; DAS SARMA, S.. **Non-abelian anyons and topological quantum computation**. Rev. Mod. Phys., 80:1083–1159, Sep 2008.

[31] PESIN, D.; MACDONALD, A. H.. **Spintronics and pseudospintronics in graphene and topological insulators**. Nat. Mater., 11:409, 2012.

[32] CHEN, W.. **Weakly interacting topological insulators: Quantum criticality and the renormalization group approach**. Phys. Rev. B, 97:115130, Mar 2018.

[33] LINDER, J.; YOKOYAMA, T. ; SUDBØ, A.. **Anomalous finite size effects on surface states in the topological insulator bi_2se_3**. Phys. Rev. B, 80:205401, Nov 2009.

[34] LU, H.-Z.; SHAN, W.-Y.; YAO, W.; NIU, Q. ; SHEN, S.-Q.. **Massive dirac fermions and spin physics in an ultrathin film of topological insulator**. Phys. Rev. B, 81:115407, Mar. 2010.

[35] SHEN, S.-Q.. **Topological Insulators: Dirac Equation in Condensed Matters (Springer Series in Solid-State Sciences)**. Springer, 2013 edition, Jan. 2013.

[36] SO, H.. **Induced topological invariants by lattice fermions in odd dimensions**. Progress of Theoretical Physics, 74(3):585–593, 1985.

[37] NIU, Q.; THOULESS, D. J. ; WU, Y.-S.. **Quantized hall conductance as a topological invariant**. Phys. Rev. B, 31:3372–3377, Mar 1985.

[38] ISHIKAWA, K.; MATSUYAMA, T.. **Magnetic field induced multicomponent qed3 and quantum hall effect**. Zeitschrift für Physik C Particles and Fields, 33(1):41–45, Mar 1986.

[39] VOLOVIK, G. E.. **An analog of the quantum hall effect in a superfluid 3he film**. JETP, 67:1804, 1988.

[40] VOLOVIK, G. E.. **The Universe in a Helium Droplet**. Oxford University Press, Mar. 2003.

[41] QI, X.-L.; HUGHES, T. L. ; ZHANG, S.-C.. **Topological field theory of time-reversal invariant insulators**. Phys. Rev. B, 78:195424, Nov 2008.

[42] WANG, Z.; QI, X.-L. ; ZHANG, S.-C.. **Topological order parameters for interacting topological insulators**. Phys. Rev. Lett., 105:256803, Dec 2010.

[43] GURARIE, V.. **Single-particle green's functions and interacting topological insulators**. Phys. Rev. B, 83:085426, Feb 2011.

[44] WANG, Z.; ZHANG, S.-C.. **Simplified topological invariants for interacting insulators**. Phys. Rev. X, 2:031008, Aug 2012.

[45] WANG, Z.; QI, X.-L. ; ZHANG, S.-C.. **Topological invariants for interacting topological insulators with inversion symmetry**. Phys. Rev. B, 85:165126, Apr 2012.

[46] WANG, Z.; YAN, B.. **Topological hamiltonian as an exact tool for topological invariants**. J. Phys. Condens. Matter, 25(15):155601, 2013.

[47] GRANDI, F.; MANGHI, F.; CORRADINI, O.; BERTONI, C. M. ; BONINI, A.. **Topological invariants in interacting quantum spin hall: a cluster perturbation theory approach**. New J. Phys., 17(2):023004, 2015.

[48] CHEN, W.. **Scaling theory of topological phase transitions**. J. Phys. Condens. Matter, 28(5):055601, 2016.

[49] CHEN, W.; SIGRIST, M. ; SCHNYDER, A. P.. **Scaling theory of z_2 topological invariants**. J. Phys. Condens. Matter, 28(36):365501, 2016.

[50] CHEN, W.; LEGNER, M.; RÜEGG, A. ; SIGRIST, M.. **Correlation length, universality classes, and scaling laws associated with topological phase transitions**. Phys. Rev. B, 95:075116, Feb 2017.

[51] CHEN, W.; SCHNYDER, A. P.. **Universality classes of topological phase transitions with higher-order band crossing**. arXiv:1901.11468.

[52] KHARITONOV, M.; MAYER, J.-B. ; HANKIEWICZ, E. M.. **Universality and stability of the edge states of chiral-symmetric topological semimetals and surface states of the luttinger semimetal**. Physical review letters, 119(26):266402, 2017.

[53] CANDIDO, D. R.; KHARITONOV, M.; EGUES, J. C. ; HANKIEWICZ, E. M.. **Paradoxical extension of the edge states across the topological phase transition due to emergent approximate chiral symmetry in a quantum anomalous hall system**. Phys. Rev. B, 98:161111, Oct 2018.

[54] CANDIDO, D. R.; FLATTÉ, M. E. ; EGUES, J. C.. **Blurring the boundaries between topological and nontopological phenomena in dots**. Phys. Rev. Lett., 121:256804, Dec 2018.

[55] YAO, W.; YANG, S. A. ; NIU, Q.. **Edge states in graphene: From gapped flat-band to gapless chiral modes**. Physical review letters, 102(9):096801, 2009.

[56] WEN, J.; RÜEGG, A.; WANG, C.-C. J. ; FIETE, G. A.. **Interaction-driven topological insulators on the kagome and the decorated honeycomb lattices**. Phys. Rev. B, 82:075125, Aug 2010.

[57] GRUSHIN, A. G.; CASTRO, E. V.; CORTIJO, A.; DE JUAN, F.; VOZMEDIANO, M. A. H. ; VALENZUELA, B.. **Charge instabilities and topological phases in the extended hubbard model on the honeycomb lattice with enlarged unit cell**. Phys. Rev. B, 87:085136, Feb 2013.

[58] JIA, Y.; GUO, H.; CHEN, Z.; SHEN, S.-Q. ; FENG, S.. **Effect of interactions on two-dimensional dirac fermions**. Phys. Rev. B, 88:075101, Aug 2013.

[59] DAGHOFER, M.; HOHENADLER, M.. **Phases of correlated spinless fermions on the honeycomb lattice**. Phys. Rev. B, 89:035103, Jan 2014.

[60] GUO, H.; JIA, Y.. **Interaction-driven phases in a dirac semimetal: exact diagonalization results**. J. Phys. Condens. Matter, 26(47):475601, 2014.

[61] LUO, X.; YU, Y. ; LIANG, L.. **Collective modes in a dirac insulator with short range interactions**. Phys. Rev. B, 91:125126, Mar 2015.

[62] AMARICCI, A.; VALLI, A.; SANGIOVANNI, G.; TRAUZETTEL, B. ; CAPONE, M.. **Coexistence of metallic edge states and antiferromagnetic ordering in correlated topological insulators**. Phys. Rev. B, 98:045133, Jul 2018.

[63] SLAGER, R.-J.; RADEMAKER, L.; ZAANEN, J. ; BALENTS, L.. **Impurity-bound states and green's function zeros as local signatures of topology**. Phys. Rev. B, 92:085126, Aug 2015.

[64] BALATSKY, A. V.; VEKHTER, I. ; ZHU, J.-X.. **Impurity-induced states in conventional and unconventional superconductors**. Rev. Mod. Phys., 78:373–433, May 2006.

[65] MARQUES, A. M.; DIAS, R. G.. **Multihole edge states in su-schrieffer-heeger chains with interactions**. Phys. Rev. B, 95:115443, Mar 2017.

[66] MARQUES, A. M.; DIAS, R. G.. **Topological bound states in interacting su–schrieffer–heeger rings**. J. Phys. Condens. Matter, 30(30):305601, jul 2018.

[67] YAHYAVI, M.; SALEEM, L. ; HETÉNYI, B.. **Variational study of the interacting, spinless su–schrieffer–heeger model**. J. Phys. Condens. Matter, 30(44):445602, oct 2018.

[68] SBIERSKI, B.; KARRASCH, C.. **Topological invariants for the haldane phase of interacting su-schrieffer-heeger chains: Functional renormalization-group approach**. Phys. Rev. B, 98:165101, Oct 2018.

[69] KUNO, Y.. **Phase structure of the interacting su-schrieffer-heeger model and the relationship with the gross-neveu model on lattice**. Phys. Rev. B, 99:064105, Feb 2019.

[70] ATALA, M.; AIDELSBURGER, M.; BARREIRO, J. T.; ABANIN, D.; KITAGAWA, T.; DEMLER, E. ; BLOCH, I.. **Direct measurement of the Zak phase in topological Bloch bands**. Nat. Phys., 9:795–800, Dec. 2013.

[71] MEIER, E. J.; AN, F. A. ; GADWAY, B.. **Observation of the topological soliton state in the su–schrieffer–heeger model**. Nat. Commun., 7:13986, 2016.

[72] YOSHIDA, T.; PETERS, R.; FUJIMOTO, S. ; KAWAKAMI, N.. **Characterization of a topological mott insulator in one dimension**. Phys. Rev. Lett., 112:196404, May 2014.

[73] KOURTIS, S.; NEUPERT, T.; MUDRY, C.; SIGRIST, M. ; CHEN, W.. **Weyl-type topological phase transitions in fractional quantum hall like systems**. Phys. Rev. B, 96:205117, Nov 2017.

[74] ZEGARRA, A.; EGUES, J. C. ; CHEN, W.. **Persistent currents and spin torque caused by percolated quantum spin hall state**. Phys. Rev. B, 101:224438, Jun 2020.

[75] SHIOMI, Y.; NOMURA, K.; KAJIWARA, Y.; ETO, K.; NOVAK, M.; SEGAWA, K.; ANDO, Y. ; SAITOH, E.. **Spin-electricity conversion induced by spin injection into topological insulators**. Phys. Rev. Lett., 113:196601, Nov 2014.

[76] ROJAS-SÁNCHEZ, J.-C.; OYARZÚN, S.; FU, Y.; MARTY, A.; VERGNAUD, C.; GAMBARELLI, S.; VILA, L.; JAMET, M.; OHTSUBO, Y.; TALEB-IBRAHIMI, A.; LE FÈVRE, P.; BERTRAN, F.; REYREN, N.; GEORGE, J.-M. ; FERT, A.. **Spin to charge conversion at room temperature by spin pumping into a new type of topological insulator: α-sn films**. Phys. Rev. Lett., 116:096602, Mar 2016.

[77] MENDES, J. B. S.; ALVES SANTOS, O.; HOLANDA, J.; LORETO, R. P.; DE ARAUJO, C. I. L.; CHANG, C.-Z.; MOODERA, J. S.; AZEVEDO, A.

; REZENDE, S. M.. **Dirac-surface-state-dominated spin to charge current conversion in the topological insulator $(\mathrm{bi}_{0.22}\mathrm{sb}_{0.78})_2\mathrm{te}_3$ films at room temperature**. Phys. Rev. B, 96:180415, Nov 2017.

[78] SHAO, Q.; YU, G.; LAN, Y.-W.; SHI, Y.; LI, M.-Y.; ZHENG, C.; ZHU, X.; LI, L.-J.; AMIRI, P. K. ; WANG, K. L.. **Strong rashba-edelstein effect-induced spin-orbit torques in monolayer transition metal dichalcogenide/ferromagnet bilayers**. Nano Lett., 16:7514, Dec 2016.

[79] ZHANG, W.; SKLENAR, J.; HSU, B.; JIANG, W.; JUNGFLEISCH, M. B.; XIAO, J.; FRADIN, F. Y.; LIU, Y.; PEARSON, J. E.; KETTERSON, J. B.; YANG, Z. ; HOFFMANN, A.. **Research update: Spin transfer torques in permalloy on monolayer mos2**. APL Mater., 4(3):032302, 2016.

[80] MENDES, J. B. S.; APARECIDO-FERREIRA, A.; HOLANDA, J.; AZEVEDO, A. ; REZENDE, S. M.. **Efficient spin to charge current conversion in the 2d semiconductor mos2 by spin pumping from yttrium iron garnet**. Appl. Phys. Lett., 112(24):242407, 2018.

[81] BANSAL, R.; KUMAR, A.; CHOWDHURY, N.; SISODIA, N.; BARVAT, A.; DOGRA, A.; PAL, P. ; MUDULI, P.. **Extrinsic spin-orbit coupling induced enhanced spin pumping in few-layer mos2/py**. J. Magn. Magn. Mater., 476:337 – 341, 2019.

[82] WU, G.; REN, Y.; HE, X.; ZHANG, Y.; XUE, H.; JI, Z.; JIN, Q. Y. ; ZHANG, Z.. **Tuning magnetization dynamics with strong spin-orbit coupling in transition-metal dichalcogenide/Co-Fe-B heterostructures**. Phys. Rev. Applied, 13:024027, Feb 2020.

[83] FAN, Y.; LI, H.; DC, M.; PETERSON, T.; HELD, J.; SAHU, P.; CHEN, J.; ZHANG, D.; MKHOYAN, A. ; WANG, J.-P.. **Spin pumping and large field-like torque at room temperature in sputtered amorphous wte2x films**. APL Materials, 8(4):041102, 2020.

[84] QIAN, X.; LIU, J.; FU, L. ; LI, J.. **Quantum spin hall effect in two-dimensional transition metal dichalcogenides**. Science, 346(6215):1344–1347, 2014.

[85] MA, Y.; KOU, L.; LI, X.; DAI, Y.; SMITH, S. C. ; HEINE, T.. **Quantum spin hall effect and topological phase transition in two-dimensional square transition-metal dichalcogenides**. Phys. Rev. B, 92:085427, Aug 2015.

[86] WU, S.; FATEMI, V.; GIBSON, Q. D.; WATANABE, K.; TANIGUCHI, T.; CAVA, R. J. ; JARILLO-HERRERO, P.. **Observation of the quantum spin hall effect up to 100 kelvin in a monolayer crystal**. Science, 359(6371):76–79, 2018.

[87] BERNEVIG, B. A.; HUGHES, T. L.. **Topological Insulators and Topological Superconductors**. Princeton University Press, Apr. 2013.

[88] COWLEY, A. M.; SZE, S. M.. **Surface states and barrier height of metal-semiconductor systems**. J. Appl. Phys., 36(10):3212–3220, 1965.

[89] TUNG, R. T.. **The physics and chemistry of the schottky barrier height**. Appl. Phys. Rev., 1(1):011304, 2014.

[90] GAMBARDELLA, P.; MIRON, I. M.. **Current-induced spin–orbit torques**. Phil. Trans. R. Soc. A, 369(1948):3175–3197, 2011.

[91] CHEN, W.; SCHNYDER, A. P.. **Majorana edge states in superconductor-noncollinear magnet interfaces**. Phys. Rev. B, 92:214502, Dec. 2015.

[92] NAGAOSA, N.. **Spin currents in semiconductors, metals, and insulators**. J. Phys. Soc. Jpn., 77(3):031010, 2008.

[93] BRYDON, P. M. R.; TIMM, C. ; SCHNYDER, A. P.. **Interface currents in topological superconductor–ferromagnet heterostructures**. New J. Phys., 15(4):045019, apr 2013.

[94] SCHNYDER, A. P.; TIMM, C. ; BRYDON, P. M. R.. **Edge currents as a signature of flatbands in topological superconductors**. Phys. Rev. Lett., 111:077001, Aug 2013.

[95] CHEN, W.. **Absence of equilibrium edge currents in theoretical models of topological insulators**. Phys. Rev. B, 101:195120, May 2020.

[96] CHEN, W.; ANDERSEN, B. M. ; HIRSCHFELD, P. J.. **Theory of resistivity upturns in metallic cuprates**. Phys. Rev. B, 80:134518, Oct 2009.

[97] TAKIGAWA, M.; ICHIOKA, M. ; MACHIDA, K.. **Relation between vortex excitation and thermal conductivity in superconductors**. Eur. Phys. J. B, 27:303.

[98] GHOSH, S.; MANCHON, A.. **Spin-orbit torque in two-dimensional antiferromagnetic topological insulators**. Phys. Rev. B, 95:035422, Jan 2017.

[99] ZHANG, S.; LEVY, P. M. ; FERT, A.. **Mechanisms of spin-polarized current-driven magnetization switching**. Phys. Rev. Lett., 88:236601, May 2002.

[100] ZHANG, S.; LI, Z.. **Roles of nonequilibrium conduction electrons on the magnetization dynamics of ferromagnets**. Phys. Rev. Lett., 93:127204, Sep 2004.

[101] LIU, D.; GUO, Y.; FANG, L. ; ROBERTSON, J.. **Sulfur vacancies in monolayer mos2 and its electrical contacts**. Applied Physics Letters, 103(18):183113, 2013.

[102] HONG, J.; HU, Z.; PROBERT, M.; LI, K.; LV, D.; YANG, X.; GU, L.; MAO, N.; FENG, Q.; XIE, L.; ZHANG, J.; WU, D.; ZHANG, Z.; JIN, C.; JI, W.; ZHANG, X.; YUAN, J. ; ZHANG, Z.. **Spin pumping and large field-like torque at room temperature in sputtered amorphous wte2x films**. Nat. Commun., 6:6293, 2015.

[103] LIN, Z.; CARVALHO, B. R.; KAHN, E.; LV, R.; RAO, R.; TERRONES, H.; PIMENTA, M. A. ; TERRONES, M.. **Defect engineering of two-dimensional transition metal dichalcogenides**. 2D Mater., 3(2):022002, apr 2016.

[104] VANCSÓ, P.; MAGDA, G. Z.; PETŐ, J.; NOH, J.-Y.; KIM, Y.-S.; HWANG, C.; BIRÓ, L. P. ; TAPASZTÓ, L.. **Spin pumping and large field-like torque at room temperature in sputtered amorphous wte2x films**. Sci. Rep., 6:29726, 2016.

[105] TIAN, J.; MIOTKOWSKI, I.; HONG, S. ; CHEN, Y. P.. **Electrical injection and detection of spin-polarized currents in topological insulator bi2te2se**. Sci. Rep., 5:14293, 2015.

[106] KONDOU, K.; YOSHIMI, R.; TSUKAZAKI, A.; FUKUMA, Y.; MATSUNO, J.; TAKAHASHI, K. S.; KAWASAKI, M.; TOKURA, Y. ; OTANI, Y.. **Fermi-level-dependent charge-to-spin current conversion by dirac surface states of topological insulators**. Nat. Phys., 12:1027, 2016.

[107] LIU, Y.; BESBAS, J.; WANG, Y.; HE, P.; CHEN, M.; ZHU, D.; WU, Y.; LEE, J. M.; WANG, L.; MOON, J.; KOIRALA, N.; OH, S. ; YANG, H..

Direct visualization of current-induced spin accumulation in topological insulators. Nat. Commun., 9:2491, 2018.

[108] DANKERT, A.; BHASKAR, P.; KHOKHRIAKOV, D.; RODRIGUES, I. H.; KARPIAK, B.; KAMALAKAR, M. V.; CHARPENTIER, S.; GARATE, I. ; DASH, S. P.. **Origin and evolution of surface spin current in topological insulators**. Phys. Rev. B, 97:125414, Mar 2018.

[109] CHEN, W.. **Edelstein and inverse edelstein effects caused by the pristine surface states of topological insulators**. J. Phys. Condens. Matter, 32:035809, 2020.

[110] CHEN, W.; SIGRIST, M.; SINOVA, J. ; MANSKE, D.. **Minimal model of spin-transfer torque and spin pumping caused by the spin hall effect**. Phys. Rev. Lett., 115:217203, Nov 2015.

[111] SAKANASHI, K.; SIGRIST, M. ; CHEN, W.. **Theory of in-plane current induced spin torque in metal/ferromagnet bilayers**. J. Phys. Condens. Matter, 30(20):205803, 2018.

A
The Current Operators

Here we delineate the way to construct the charge and spin current operators for this lattice model. Considering the translational invariance of the system along $\hat{\mathbf{x}}$, then we only need to calculate the currents which flow along $\hat{\mathbf{x}}$. We obtain the corresponding current operator from the respective polarization operator by using the Heisenberg equation of motion $J^a = \dot{P}^a = \frac{i}{\hbar}[H, P^a]$, where the tedious commutator $[H, P^a]$ may be simplified as explained next. We focus only on hopping terms present in Eq. (3-30) since only them contribute to the current operator, these terms take the general form

$$H^{\delta}_{L\alpha M\beta} = \sum_j T^{\delta}_{L\alpha M\beta} c^{\dagger}_{jL\alpha} c_{j+\delta M\beta} + T^{\delta *}_{L\alpha M\beta} c^{\dagger}_{j+\delta M\beta} c_{jL\alpha} \ , \tag{A-1}$$

this factor outlines the hopping of electrons between site/orbital/spin $jL\alpha$ and $j+\delta M\beta$ along the planar orientations $\delta = \{a, b\}$, where $T^{\delta}_{L\alpha M\beta}$ stands for the hopping amplitude. If we take into account the fact that the hopping part of the full Hamiltonian is made up from the summation $H_t = \sum_{\delta} \sum_{L\alpha M\beta} H^{\delta}_{L\alpha M\beta}$, we find out that the contribution to the the charge current ($a = 0$) and the spin current ($a = z$) comming from a specific orbital/spin species $I\eta\lambda$ is given by, considering the definition set in Eq. (3-36),

$$\begin{aligned}
J^a_{I\eta\lambda} &= \frac{i}{\hbar} \sum_{\delta} \sum_{L\alpha M\beta} \left[H^{\delta}_{L\alpha M\beta}, P^a_{I\eta\lambda} \right] \\
&= \frac{i}{\hbar} \sum_i \Bigg\{ \sum_{M\beta} \left[-x_i T^a_{I\lambda M\beta} \right] c^{\dagger}_{iI\eta} \sigma^a_{\eta\lambda} c_{i+aM\beta} \\
&+ \sum_{L\alpha} \left[(x_i + a) T^a_{L\alpha I\eta} \right] c^{\dagger}_{iL\alpha} \sigma^a_{\eta\lambda} c_{i+aI\lambda} \\
&\quad + \sum_{L\alpha} \left[(-x_i - a) T^{a*}_{L\alpha I\lambda} \right] c^{\dagger}_{i+aI\eta} \sigma^a_{\eta\lambda} c_{iL\alpha} \\
&\quad + \sum_{M\beta} \left[x_i T^{a*}_{I\eta M\beta} \right] c^{\dagger}_{i+aM\beta} \sigma^a_{\eta\lambda} c_{iI\lambda} \Bigg\} \ .
\end{aligned} \tag{A-2}$$

We then introduce there all the nonvanishing hopping amplitudes $T^{\delta}_{L\alpha M\beta}$ and $T^{\delta *}_{L\alpha M\beta}$ as delineated in Eq. (3-30), and perform a summation over all of the

$I\eta\lambda$ species. The final form for the charge current operator can then be written as

$$\begin{aligned} J^0 &= \frac{1}{\hbar}\sum_{i\in TI}\sum_{\sigma}\Big\{\eta_\sigma t\, c^\dagger_{is\sigma}c_{i+ap\sigma} + \eta_\sigma t\, c^\dagger_{i+ap\sigma}c_{is\sigma} \\ &\quad +\eta_\sigma t\, c^\dagger_{ip\sigma}c_{i+as\sigma} + \eta_\sigma t\, c^\dagger_{i+as\sigma}c_{ip\sigma}\Big\} \\ &+ \frac{1}{\hbar}\sum_{i\in TI}\sum_{\sigma}\Big\{-it'\, c^\dagger_{is\sigma}c_{i+as\sigma} + it'\, c^\dagger_{i+as\sigma}c_{is\sigma} \\ &\quad +it'\, c^\dagger_{ip\sigma}c_{i+ap\sigma} - it'\, c^\dagger_{i+ap\sigma}c_{ip\sigma}\Big\} \\ &+ \frac{1}{\hbar}\sum_{i\in FM}\sum_{\sigma}\Big\{-it_F\, c^\dagger_{is\sigma}c_{i+as\sigma} + it_F\, c^\dagger_{i+as\sigma}c_{is\sigma} \\ &\quad -it_F\, c^\dagger_{ip\sigma}c_{i+ap\sigma} + it_F\, c^\dagger_{i+ap\sigma}c_{ip\sigma}\Big\}\ , \end{aligned} \tag{A-3}$$

where here $\eta_\uparrow = 1$, $\eta_\downarrow = -1$, and $i \in TI$, $i \in FM$ and $i \in BD$ tell us that the positions i and $i + a$ belong to the BHZ model region, the FMM region, and the interface bonds. By following a very similar approach, we find out that the operator for the spin current polarized along z can be written as

$$\begin{aligned} J^z &= \frac{1}{\hbar}\sum_{i\in TI}\sum_{\sigma}\Big\{t\, c^\dagger_{is\sigma}c_{i+ap\sigma} + t\, c^\dagger_{i+ap\sigma}c_{is\sigma} \\ &\quad +t\, c^\dagger_{ip\sigma}c_{i+as\sigma} + t\, c^\dagger_{i+as\sigma}c_{ip\sigma}\Big\} \\ &+ \frac{1}{\hbar}\sum_{i\in TI}\sum_{\sigma}\Big\{-it'\eta_\sigma\, c^\dagger_{is\sigma}c_{i+as\sigma} + it'\eta_\sigma\, c^\dagger_{i+as\sigma}c_{is\sigma} \\ &\quad +it'\eta_\sigma\, c^\dagger_{ip\sigma}c_{i+ap\sigma} - it'\eta_\sigma\, c^\dagger_{i+ap\sigma}c_{ip\sigma}\Big\} \\ &+ \frac{1}{\hbar}\sum_{i\in FM}\sum_{\sigma}\Big\{-it_F\eta_\sigma\, c^\dagger_{is\sigma}c_{i+as\sigma} + it_F\eta_\sigma\, c^\dagger_{i+as\sigma}c_{is\sigma} \\ &\quad -it_F\eta_\sigma\, c^\dagger_{ip\sigma}c_{i+ap\sigma} + it_F\eta_\sigma\, c^\dagger_{i+ap\sigma}c_{ip\sigma}\Big\}\ , \end{aligned} \tag{A-4}$$

which is actually of the very same form as J^0, but for this spin case the spin up and down channels have an additional minus sign difference, which is expected since we know that spins having opposite orientations have a sign difference in their respective group velocities (a feaure which is very clear by looking at the Dirac cone).

B
Linear Response Theory for the Magnetoelectric Susceptibility

In order to compute the spin accumulation induced by a charge current, we make use of linear response theory which provides a value for the local spin accumulation $\sigma^b(i,t)$, this is an effect which arises from a perturbation $H'(t')$ present in the Hamiltonian

$$\sigma^b(i,t) = -i\int_{-\infty}^{t} dt' \langle \left[\sigma^b(i,t), H'(t')\right]\rangle \ , \tag{B-1}$$

where $\sigma^b(i,t) = \sum_{I\beta\gamma} c^{\dagger}_{iI\beta}(t)\sigma^b_{\beta\gamma}c_{iI\gamma}(t)$ stands for the component $b = \{x,y,z\}$ of the spin operator at site i, and the fermionic operators $c_{iI\gamma}(t)$ are represented in the Heisenberg picture. The origin of the perturbation is in the longitudinal component of the vector field $A(j,t')$ which provides the electric field and so the electric current, in this way the perturbation Hamiltonian is written as

$$H'(t') = -\sum_j J^0(j,t')A(j,t') \ , \tag{B-2}$$

where the electric field arises from the time-variation of the vector field $A(i,t) = A(i)e^{-i\omega t}$

$$E = -\partial_\beta V - \frac{\partial A}{\partial t} = -\frac{\partial A}{\partial t} = i\omega A \ . \tag{B-3}$$

Consequently, we could write the commutator in Eq. (B-1) as

$$\left[\sigma^b(i,t), H'(t')\right] = \frac{i}{\omega}\sum_j e^{i\omega(t-t')}E(j,t)\left[\sigma^b(i,t), J^0(j,t')\right], \tag{B-4}$$

because the electric field has a fixed unique value of wave length and frequency $E(i,t) = E^0 e^{i\mathbf{q}\cdot\mathbf{r}_i - i\omega t}$. From these considerations, the local spin accumulation

from Eq. (B-1) is simplified as

$$\begin{aligned}\sigma^b(\mathbf{r},t) &= \sum_j \int_{-\infty}^{\infty} dt' e^{i\omega(t-t')} \frac{1}{\omega}\theta(t-t') \\ &\quad \times \langle \Big[\sigma^b(i,t), J^0(j,t')\Big] \rangle E(j,t) \\ &= \sum_j \int_{-\infty}^{\infty} dt' e^{i\omega(t-t')} \frac{i\pi^b(i,j,t-t')}{\omega} E(j,t) \\ &= \sum_j \frac{i\pi^b(i,j,\omega)}{\omega} E(j,t) \equiv \sum_j \chi^b(i,j,\omega) E(j,t). \end{aligned} \tag{B-5}$$

The function $\chi^b(i,j,\omega)$ represents the response coefficient for the contribution to the $\sigma^b(i,t)$ at lattice site i arising from the longitudinal electric field $E(j,t)$ which is applied at lattice site j. Furthermore, we assume that the electric field remains constant everywhere, i.e., $\mathbf{q} \to 0$ in such a way that $E(i,t) = E(j,t) = E^0 e^{-i\omega t}$. For this situation we can write

$$\sigma^b(i,t) = \left\{ \sum_j \chi^b(i,j,\omega) \right\} E(i,t) = \chi^b(i,\omega) E(i,t) \ , \tag{B-6}$$

and our goal is to solve for the real part of the DC (zero frequency limit) magnetoelectric susceptibility

$$\lim_{\omega\to 0} \mathrm{Re}\chi^b(i,\omega) = \lim_{\omega\to 0} \mathrm{Re} \left\{ \frac{i}{\omega} \sum_j \pi^b(i,j,\omega) \right\} \ . \tag{B-7}$$

Denoting by $|n\rangle$ the eigenstate with corresponding eigenenergy E_n which is obtained after proper diagonalization of the BHZ/FMM junction described by the Hamiltonian of Eq. (3-30), the retarded factor $\pi^b(i,j,\omega)$ has the explicit form

$$\pi^b(i,j,\omega) = \sum_{m,n} \langle n|\sigma^b(i)|m\rangle\langle m|J^0(j)|n\rangle \frac{f(E_n) - f(E_m)}{\omega + E_n - E_m + i\eta} \ , \tag{B-8}$$

where η is introduced to create a small artificial broadening. Considering the approximation $\eta/(x^2+\eta^2) = \pi\delta_\eta(x)$, the DC limit in Eq. (B-7) then reads

$$
\begin{aligned}
&-\lim_{\omega\to 0}\mathrm{Re}\left\{\frac{i}{\omega}\sum_j \pi^b(i,j,\omega)\right\} \\
&= \lim_{\omega\to 0}\left\{\sum_{m,n}\langle n|\sigma^b(i)|m\rangle\langle m|\sum_j J^0(j)|n\rangle\frac{f(E_n)-f(E_m)}{\omega}\frac{-\eta}{(\omega+E_n-E_m)^2+\eta^2}\right\} \\
&= \lim_{\omega\to 0}\left\{\sum_{m,n}\langle n|\sigma^b(i)|m\rangle\langle m|\sum_j J^0(j)|n\rangle\frac{f(E_n)-f(E_n+\omega)}{\omega}(-\pi)\delta_\eta(\omega+E_n-E_m)\right\} \\
&= \sum_{m,n}\langle n|\sigma^b(i)|m\rangle\langle m|\sum_j J^0(j)|n\rangle\left(\pi\frac{\partial f(E_n)}{\partial E_n}\right)\delta_\eta(E_n-E_m) \\
&= \sum_{m,n}\langle n|\sigma^b(i)|m\rangle\langle m|\sum_j J^0(j)|n\rangle\tilde{F}(E_n,E_m)\ , \qquad \text{(B-9)}
\end{aligned}
$$

where we took into account the facts that $\mathrm{Re}\left[\langle m|\sum_j J^0(j)|n\rangle\right]$ is even but $\mathrm{Im}\left[\langle m|\sum_j J^0(j)|n\rangle\right]$ is odd in (n,m), $\mathrm{Re}\left[\langle n|\sigma^b(i)|m\rangle\right]$ is even but $\mathrm{Im}\left[\langle n|\sigma^b(i)|m\rangle\right]$ is odd in (n,m), and the real part of $(1/\omega)(f(E_n)-f(E_m))/(\omega+E_n-E_m+i\eta)$ in the $\eta\to 0$ and $\omega\to 0$ limit is even in (n,m) to wipe out many terms in the $\sum_{nm}$ summation. The distribution function $\tilde{F}(E_n,E_m)$ can be further approximated as

$$
\begin{aligned}
\tilde{F}(E_n,E_m) &= \left(\pi\frac{\partial f(E_n)}{\partial E_n}\right)\delta_\eta(E_n-E_m) = \int d\omega\,\delta(\omega-E_n)\left(\pi\frac{\partial f(\omega)}{\partial\omega}\right)\delta_\eta(\omega-E_m) \\
&\approx \int d\omega\,\frac{\eta}{(\omega-E_n)^2+\eta^2}\left(\frac{1}{\pi}\frac{\partial f(\omega)}{\partial\omega}\right)\frac{\eta}{(\omega-E_m)^2+\eta^2}\ , \qquad \text{(B-10)}
\end{aligned}
$$

which provides Eq. (3-42). Additionally, we impose the vanishing of diagonal elements $\tilde{F}(E_n,E_n)=0$ as is dictated by Eq. (B-8).

Despite the success of linear response theory to investigate metallic systems, for this BHZ model we found out that some numerical subtleties must be implemented. First of all, for the homogeneous isolated BHZ system, there is a double degeneracy in all of its states which arises from Kramers' theorem (look at the block-diagonal form of Eq. (3-15)). Additionally, both the edge state located at the $y=1$ edge and the one localized at the $y=N_{y,TI}$ edge are degenerate at the same energy, as a consequence of this the wave function that is calculate numerically could be an arbitrary superposition of them, this issue makes difficult the computation of the $\langle n|\sigma^b(i)|m\rangle$ and $\langle m|\sum_j J^0(j)|n\rangle$ matrix elements which permit to construct the correlator in

Eq. (3-42). Furthermore, we find out that the matrix elements $\langle m|\sum_j J^0(j)|n\rangle$ between the edge states are zero for the homogeneous BHZ model. The reason is that this matrix element is the one corresponding to the velocity operator, and the edge states are eigenstates of this specific operator, therefore $\langle m|\sum_j J^0(j)|n\rangle \propto \langle m|\hat{v}_x|n\rangle = v_F\langle m|n\rangle = 0$ if $|n\rangle \neq |m\rangle$.

To wipe out these numerical contradictions, we concentrate on the BHZ/FMM junction system under the presence of disorder (impurities) and a very small magnetic field applied at the free edge for the following reasons. First of all, when we put in contact the two sub-systems the degeneracy between the two edges of the BHZ region is removed because of the nonzero interface coupling $t_B \neq 0$ to the FMM at the interface $y = N_{y,TI}$, therefore this junction solves the problem of the superposition of the wave functions from the two edges. Notice that despite the contact at the interface, the $y = 1$ free edge still exhibits very accurately the Edelstein effect of an isolated BHZ system, therefore we could use this effect at the free edge to compare with the $t_B \neq 0$ cases at the interface $y = N_{y,TI}$. Secondly, the vanishing $\langle m|\sum_j J^0(j)|n\rangle$ is resolved because the edge state under the presence of disorder is not anymore an eigenstate of the velocity operator. The presence of disorder also increases the accuracy of the numerical calculation because it permits to smear out the sparce edge state energy spectrum. Since Kramers degeneracy is still present at the free edge $y = 1$, to remove that degeneracy between spins up and down we apply a small magnetic field there $\mathbf{B}(y = 1) = B_{y=1}\hat{\mathbf{z}}$ and impose the condition $|n - m| > 1$ to avoid neighboring energy levels such that there is not any ambiguity in the calculation of the matrix elements corresponding to the spin operator $\langle n|\sigma^b(i)|m\rangle$.

Regarding the numerics, we performed the simulation on a lattice of finite size $N_x \times (N_{y,TI} + N_{y,FM}) = 48 \times (10 + 6)$ with 10% impurities having a potential of strength $U_{imp} = 4$, we also considered an artificial broadening of $\eta = 0.1$ (equivalent to a mean free time of $\tau \sim 10^{-14}$s) and set the temperature to $k_BT = 0.03$ (room temperature). Since the distribution function $\tilde{F}(E_n, E_m)$ is highly peaked in a vicinity of the Fermi level $E_n \approx E_m \approx 0$, then it is possible to truncate the summation $\sum_{n,m}$ in Eq. (3-42) and consider just the 100 states closer to the chemical potential. The accuracy could be improved at larger system sizes, but our approximation could achieve about $70\% \sim 80\%$ accuracy, which is more than enough to obtain meaningful conclusions.

The numerical value obtained for the response function χ^b results to be of the order of $\mathcal{O}(1) \times ae/t \sim 10^{-9}$mC/J. Considering a typical external charge

current of $j_c \sim 10^{11}\mathrm{A/m}^2$ and an electrical conductivity of $\sim 10^7\mathrm{S/m}$ for the FMM, then the corresponding electric field is of the order of $E \sim 10^4\mathrm{kgm/C}s^2$, this provides a spin polarization of $\sigma^b(i) \sim 10^{-5}$. Fixing $J_{ex} = 0.1\mathrm{eV}$, the current induced spin torque at this typical current density is given by the numerical values of $\chi^b(i)$ averaged only over the FMM sites and multiplied by GHz.